**Title**
Advancements in Prostate-Specific Membrane Antigen Targeted Radionuclide Therapy Through Dosimetry



**Author**
Meyer, Catherine Anne Louise

**Publication Date**
2022

Peer reviewed|Thesis/dissertation

UNIVERSITY OF CALIFORNIA

Los Angeles

# Advancements in Prostate-Specific Membrane Antigen Targeted Radionuclide Therapy Through Dosimetry

A dissertation submitted in partial satisfaction of the

requirements for the degree Doctor of Philosophy in

Physics and Biology in Medicine

by

Catherine Anne Louise Meyer

2022

ABSTRACT OF THE DISSERTATION

Advancements in Prostate-Specific Membrane Antigen Targeted Radionuclide Therapy Through Dosimetry

by

Catherine Anne Louise Meyer

Doctor of Philosophy in Physics and Biology in Medicine

University of California, Los Angeles, 2022

Professor Magnus Dahlbom, Chair

One promising treatment option for metastatic castration-resistant prostate cancer is systemic radionuclide therapy targeting prostate-specific membrane antigen (PSMA). PSMA is a highly overexpressed protein on prostate cancer cells, but has low expression in normal organ tissues. Small molecule inhibitors of PSMA specifically bind to PSMA and can therefore be labeled with imaging or therapeutic isotopes to deliver the radiation directly to the site of cancer cells. When labeled with a therapeutic isotope, such as a beta- or alpha-emitter, PSMA ligands acts as a delivery vector for a lethal payload of radiation to cancer cells. This therapy is known as radionuclide therapy (RNT).

The most commonly used therapeutic isotope in PSMA-targeted RNT is lutetium-177 ($^{177}$Lu). Treatment response rates to $^{177}$Lu-PSMA RNT vary widely across treatment

studies and patient cohorts from 30 to 70%. However, actinium-225 ($^{225}$Ac), an alpha particle emitter, has emerged as a promising alternative isotope with favorable therapeutic decay properties. Alpha particles are of interest in RNT due to higher energy deposition over a shorter tissue penetration range, ostensibly causing more dense ionizations and inducing more DNA damage as compared with beta particles. While fewer clinical studies have been conducted with $^{225}$Ac-PSMA RNT, the studies so far report impressive response rates, particularly in chemotherapy-naïve patients. Despite improved biochemical response in $^{225}$Ac-treated patients, this comes at the cost of higher-grade toxicities. Overall, PSMA RNT using either therapeutic isotope is not curative and even in those patients who do respond, the disease almost inevitably relapses. One possible explanation for treatment failure and disease relapse is that the tumor targets are not receiving a sufficiently high radiation dose necessary to kill the cancer cells.

The current treatment paradigm is to treat with fixed activities for the same number of cycles at fixed intervals. However, treatment with a fixed activity neglects the fact that the mechanism of action of RNT is by radiation, and as such warrants radiation dose evaluation. To move away from a “one size fits all” approach to more individualized treatment, dosimetry can be used to devise safe therapeutic activities to deliver maximal tumor doses while delivering as low as achievable doses to non-target volumes.

This dissertation addresses two overarching goals: i) to identify clinically relevant differences between $^{177}$Lu and $^{225}$Ac by incorporating dosimetry in translational RNT research, and ii) to evaluate the clinical dosimetry of imaging and therapy theranostic agents. The first specific aim uses various in vivo murine models of prostate cancer for the optimization of preclinical PSMA RNT exploring the effect of different therapeutic

isotopes and targeting ligands relative to intervention time and lesion size. The second specific aim evaluates the clinical radiation dosimetry profile of two new imaging theranostic tracers. Finally, the third specific aim seeks to quantify the patient-specific absorbed doses in tumors and normal organs for therapeutic $^{177}$Lu and $^{225}$Ac PSMA RNT agents.

The dissertation of Catherine Anne Louise Meyer is approved.

Johannes Czernin

Jeremie Calais

Keisuke Steven Iwamoto

Nicholas G Nickols

Roger Slavik

Magnus Dahlbom, Committee Chair

University of California, Los Angeles

2022

Dedicated to my parents, Beatrice Simonis and Rudi Meyer.

TABLE OF CONTENTS

LIST OF FIGURES

LIST OF TABLES

# LIST OF ABBREVIATIONS

| | |
|---|---|
| Androgen deprivation therapy | ADT |
| Bioluminescence imaging | BLI |
| Cancer-associated fibroblast | CAF |
| Computed tomography | CT |
| External beam radiation therapy | EBRT |
| Fibroblast activation protein | FAP |
| Fibroblast activation protein inhibitor | FAPI |
| Hematoxylin and eosin | H&E |
| Maximum intensity projection | MIP |
| Metastatic castration-resistant prostate cancer | mCRPC |
| Medical internal radiation dosimetry | MIRD |
| NOD scid gamma | NSG |
| Patient derived xenograft | PDX |
| Peptide receptor radionuclide therapy | PRRT |
| Positron emission tomography | PET |
| Prostate specific antigen | PSA |

| | |
|---|---|
| Prostate specific membrane antigen | PSMA |
| Radioguided surgery | RGS |
| Radionuclide therapy | RNT |
| Region of interest | ROI |
| Relative biologic effectiveness | RBE |
| Single photon emission computed tomography | SPECT |
| Standardized uptake value | SUV |
| Targeted alpha therapy | TAT |
| Time-integrated activity coefficient | TIAC |
| Tumor-to-background ratio | TBR |
| Volume of interest | VOI |

# ACKNOWLEDGMENTS

I would first like to thank my doctoral committee: Dr. Johannes Czernin, Dr. Roger Slavik, Dr. Jeremie Calais, Dr. Kei Iwamoto, Dr. Nicholas Nickols, and finally, the Chair of my committee Dr. Magnus Dahlbom. I am so grateful to all Committee members for their willingness to share their expertise, and generosity with their time to mentor me and help guide my research.

There is no doubt that I would not be here without the support and mentorship of Dr. Roger Slavik and Dr. Andreea Stuparu. I thank Roger for taking me on as a graduate student, for his patience in training me, and his leadership to pursue the projects we believed in. I thank Andreea for teaching me everything I know about conducting preclinical research. Not only did she teach me what it means to be a good scientist, she also serves as a shining example of how to be a good person along the way.

I would like to acknowledge the entire community of scientists, physicians, and colleagues on the A-level. First, I thank Dr. Christine Mona and Dr. Katharina Lückerath for their constant support since my first day in the lab. Also, I thank Dr. Caius Radu and his entire group for many successful joint collaborations. I thank Dr. Marco Taddio and Joel Almajano for their friendship and of course countless lunches. I thank Wes Armstrong for his contagious optimism. I thank Dr. Giuseppe Carlucci, Dr. Roger Slavik, and Dr. Lea Nyiranshuti for their tireless work at the cyclotron, and without whom none of our work in radionuclide therapy would be possible.

Thank you to Kiara Booker, Rejah Alano, Jeannine Gartmann, Lindy Gardner, and Stephanie Lira – the clinic would not be the same without these inspirational women

whose dedication to patient care is unmatched. I thank David Sennung for his ability to spread cheer throughout the clinic and for sharing his passion for medical physics. I also thank Dr. Ida Sonni, whose professional mentorship has helped me so much and has evolved into lasting friendship.

I could not ask for a better PI and mentor than Magnus Dahlbom. I thank Magnus for his thoughtful guidance and advice over the last 5 years and for always believing in me. I will forever be grateful to have trained with him. I would also like to acknowledge the incredible support I have received from Dr. Jeremie Calais as a consistent source of encouragement in my ear. I thank Dr. Johannes Czernin for helping me grow as a scientist and for fostering a sense of community in our work family. To Magnus, Jeremie, and Johannes: it has been the privilege of my career to train under your leadership and mentorship. Thank you.

I would also like to extend my gratitude to the entire PBM community. I thank Dr. Michael McNitt-Gray for his unwavering dedication to his students and for championing a spirit of achievement, respect, and joy in the program. Countless PBM graduate students have made an immense impact on my journey at UCLA. In particular, I thank Mike Lauria, Brad Stiehl, and Nyasha Maforo for their constant support and friendship.

Lastly, I thank Avery Rux for his support that started long before I even began my graduate school journey. Finally, I am grateful to my family: my sister and best friend Brigitte Meyer, my mother Beatrice Simonis, and my father and role model Rudi Meyer.

I acknowledge that versions of the following manuscripts, either published, submitted, or in preparation, were the basis of certain chapters of the dissertation.

**Chapter 2** is a version of: Meyer C*, Stuparu A*, Evans-Axelsson S, Lückerath K, Wei L, Kim W, Poddar S, Mona C, Dahlbom M, Girgis M, Radu CG, Czernin J, Slavik R. Targeted alpha therapy in a systemic mouse model of prostate cancer - a feasibility study. Theranostics. 2020; 10:2612-2620. *Contributed equally.

**Chapter 3** is a version of: Meyer C, Stuparu A, Wei L, Lückerath K, Czernin J, Slavik R, Dahlbom M. Tandem isotope therapy with $^{225}$Ac- and $^{177}$Lu-PSMA-617 in a murine model of prostate cancer. [Manuscript in preparation].

**Chapter 3** also includes excerpts of: Stuparu A, Capri J, Meyer C, Le TM, Evans-Axelsson S, Current K, Lennox M, Mona C, Fendler WP, Calais J, Eiber M, Dahlbom M, Czernin J, Radu CG, Lückerath K, Slavik R. Mechanisms of resistance to PSMA-targeted radioligand therapy in a mouse model of prostate cancer. J Nucl Med. 2021; 62:989-995.

**Chapter 4** is a version of: Meyer C, Prasad V, Stuparu A, Kletting P, Glatting G, Miksch J, Solbach C, Lückerath K, Nyiranshitu L, Zhu S, Czernin J, Beer J, Slavik R, Calais J, Dahlbom M. Comparison of PSMA-TO-1 and PSMA-617 labelled with $^{68}$Ga, $^{177}$Lu and $^{225}$Ac. [Manuscript submitted].

**Chapter 5** is a version of: Meyer C, Dahlbom M, Lindner T, Vauclin S, Mona C, Slavik R, Czernin J, Haberkorn U, Calais J. Radiation dosimetry and biodistribution of $^{68}$Ga-FAPI-46 PET imaging in cancer patients. J Nucl Med. 2020; 26:2946-2955.

**Chapter 6** is a version of: Urbán S, Meyer C, Dahlbom M, Farkas I, Sipka G, Besenyi Z, Czernin J, Calais J, Pávics L. Radiation dosimetry of $^{99m}$Tc-PSMA-I&S: a single-center prospective study. J Nucl Med. 2021; 62:1075-1081.

**Chapter 7** is a version of: Meyer C, Mirando D, Adams T, Ranganathan D, Esfandiari R, Delpassand E, Czernin J, Calais J, Dahlbom M. Dosimetry of mCRPC patients treated with 177Lu-PSMA-617: a post-hoc analysis of a prospective phase 2 study. [Manuscript in preparation].

**Chapter 8** is a version of: Meyer C, Allmann A, Allmann J, Eiber M, Czernin J, Dahlbom M, Calais J. Extrapolating organ and tumor doses for $^{225}$Ac-PSMA-I&T radionuclide therapy in patients with mCRPC. [Manuscript in preparation].

VITA

## EDUCATION

**UCLA** (University of California, Los Angeles)

2017 – 2019 M.S. in Physics & Biology in Medicine

**Carleton College** (Northfield, MN)

2011 – 2015 B.A. in Physics

## PEER-REVIEWED PUBLICATIONS

1. **Meyer C**, Prasad V, Stuparu A, Kletting P, Glatting G, Miksch J, Solbach C, Lückerath K, Nyiranshitu L, Zhu S, Czernin J, Beer J, Slavik R, Calais J, Dahlbom M. Comparison of PSMA-TO-1 and PSMA-617 labelled with $^{68}$Ga, $^{177}$Lu and $^{225}$Ac. [Submitted].

2. Urbán S, **Meyer C**, Dahlbom M, Farkas I, Sipka G, Besenyi Z, Czernin J, Calais J, Pávics L. Radiation dosimetry of $^{99m}$Tc-PSMA-I&S: a single-center prospective study. J Nucl Med. 2021; 62:1075-1081.

3. Stuparu A, Capri J, **Meyer C**, Le TM, Evans-Axelsson S, Current K, Lennox M, Mona C, Fendler WP, Calais J, Eiber M, Dahlbom M, Czernin J, Radu CG, Lückerath K, Slavik R. Mechanisms of resistance to PSMA-targeted radioligand therapy in a mouse model of prostate cancer. J Nucl Med. 2021; 62:989-995. (Cover article).

4. **Meyer C**, Dahlbom M, Lindner T, Vauclin S, Mona C, Slavik R, Czernin J, Haberkorn U, Calais J. Radiation dosimetry and biodistribution of $^{68}$Ga-FAPI-46 PET imaging in cancer patients. J Nucl Med. 2020; 26:2946-2955.

5. **Meyer C***, Stuparu A*, Evans-Axelsson S, Lückerath K, Wei L, Kim W, Poddar S, Mona C, Dahlbom M, Girgis M, Radu CG, Czernin J, Slavik R. Targeted alpha therapy in a systemic mouse model of prostate cancer - a feasibility study. Theranostics. 2020; 10:2612-2620.

6. Current K, **Meyer C**, Magyar C, Mona C, Almajano J, Slavik R, Stuparu A, Cheng C, Dawson D, Radu CG, Czernin J, Lückerath K. Investigating PSMA-targeted radioligand therapy efficacy as a function of cellular PSMA levels and intra-tumoral PSMA heterogeneity. Clin Can Res. 2020; 61:1171-1177.

## SELECTED CONFERENCE PRESENTATIONS

1. Extrapolating organ and tumor doses for $^{225}$Ac-PSMA-IT radionuclide therapy in patients with mCRPC. Society of Nuclear Medicine & Molecular Imaging Annual Meeting 2022 - upcoming June 2022.

2. Comparison of PSMA-TO-1 and PSMA-617 labelled with $^{68}$Ga, $^{177}$Lu and $^{225}$Ac: a first in-human translational study. Top Rated Oral Session, European Association of Nuclear Medicine Annual Meeting 2021 -Virtual.

3. Patient-specific tumor dosimetry in mCRPC patients treated with $^{177}$Lu-PSMA-617. Society of Nuclear Medicine & Molecular Imaging Annual Meeting 2021 -Virtual.

4. A combination isotope approach towards improved PSMA RLT in a murine model of prostate cancer. Society of Nuclear Medicine & Molecular Imaging Annual Meeting 2020 -Virtual.

5. Biodistribution and radiation dosimetry study of $^{68}$Ga-FAPi-46 PET imaging in patients with various cancers. European Association of Nuclear Medicine Annual Meeting 2019, Barcelona, Spain.

6. Murine models of prostate cancer to study resistance mechanisms to alpha-therapy using PSMA-617. Society of Nuclear Medicine & Molecular Imaging Annual Meeting 2019, Anaheim, CA.

7. Therapeutic efficacy and dosimetry of targeted alpha therapy using $^{225}$Ac-PSMA-617 in a murine model of prostate cancer. International Symposium on Targeted Alpha Therapy 2019, Ottawa, Canada.

## SELECTED AWARDS

2022 ACR Medical Physics Graduate Student Scholarship

2021 UCLA Physics & Biology in Medicine Moses A. Greenfield Award

2021 SNMMI Alavi-Mandell Publication Award

2021 UCLA Graduate Division Dissertation Year Fellowship

2020 SNMMI Student Research Grant

2019 Best poster at UCLA Physics & Biology in Medicine Research Symposium

# Chapter 1: Introduction

## 1.1 PSMA-Targeted Theranostics

Nuclear medicine theranostics is a term used to describe the combination of diagnostic molecular imaging and targeted therapeutics towards more patient-specific cancer diagnosis and treatment. Broadly speaking, theranostics refers to the coupling of diagnostic and therapeutic modalities targeting the same biological target. The goals of a theranostic approach include enabling sensitive disease detection, improving patient treatment selection, with an integrated imaging platform to evaluate responses to therapy, and ultimately improve treatment outcomes (*1*). The field of nuclear medicine is currently experiencing a “renaissance” of sorts because of rapidly increasing interest and investment in theranostics, leveraging this more individualized approach for precision medicine (*2*).

A theranostic agent comprises a targeting molecule, such as a small molecule inhibitor or an antibody, chemically bound with a radionuclide (*3*). These targeting molecules are designed to specifically seek out cancer cell markers and labeled with radionuclides to deliver radiation directly to the site of cancer cells. These agents are labeled either with diagnostic radionuclides (gamma- or positron-emitting isotopes) for disease localization, or therapeutic radionuclides (beta- or alpha-emitting isotopes) that are intended to deliver lethal doses of radiation. First, the targeting molecule is labeled with a gamma- or positron-emitting isotope and a diagnostic nuclear medicine scan is acquired to determine target expression, disease localization, and therapeutic eligibility. Then, only the patients who are positive for the target by imaging will be treated with the

corresponding therapeutic companion radiopharmaceutical (labeled with a therapeutic isotope that decays by alpha or beta particles). This treatment paradigm of first imaging then treating works based on the notion that the therapeutic radiopharmaceutical accumulates with the same biodistribution as identified on the diagnostic scan.

One of the most promising cancer cell surface receptors for application in theranostics is prostate specific membrane antigen (PSMA). PSMA, also known as glutamate carboxypeptidase II, is a transmembrane protein with a large extracellular domain for substrate binding and an intracellular domain containing an internalization motif. PSMA is encoded by the FOLH1 (folate hydrolase 1) gene and is observed to be upregulated in prostate adenocarcinoma (*4,5*). Despite its name suggesting exclusive expression in prostate tissue, PSMA is known to be expressed in non-prostatic tissue including salivary glands, kidneys, liver, and gastrointestinal tissue (*6,7*). However, the level of overexpression of PSMA in prostate cancer tissue is on the order of 100-1000 times greater than observed in benign tissue (*6,8,9*). This overexpression makes PSMA an ideal target for both imaging and precision therapeutics. In addition, high PSMA expression is associated with increased cancer aggression and is an indicator of poor prognosis (*8,10,11*).

In response to the significant specificity of PSMA for prostate cancer, researchers have developed targeting molecules designed to bind specifically to PSMA. Multiple antibody and small molecule inhibitor ligands were subsequently designed (*12-14*). The low molecular weight of the small molecule ligands compared to antibodies leads to different pharmacokinetic properties, including more rapid biological clearance and more efficient tissue penetration (*12,15*). The focus of this work is on the theranostic

applications of small molecule inhibitors, namely PSMA-11 and PSMA-617, two of the most prevalent PSMA ligands for imaging and therapy, respectively (*16*).

### 1.2 Therapeutic Isotopes

The two major therapeutic isotopes in the clinical landscape right now are lutetium-177 ($^{177}$Lu) and actinium-225 ($^{225}$Ac). PSMA-targeted radionuclide therapy (RNT) is most often delivered using $^{177}$Lu, owing to its medium energy beta-emission (0.5 MeV) with long half-life of 6.7 days (*17*). One alternative is $^{225}$Ac, an alpha-emitting isotope whose decay chain yields a net 4 alpha particles and 3 beta disintegrations. Isotope decay schemes are shown in Figure 1.1 and other relevant physical properties are outlined in Table 1.1.

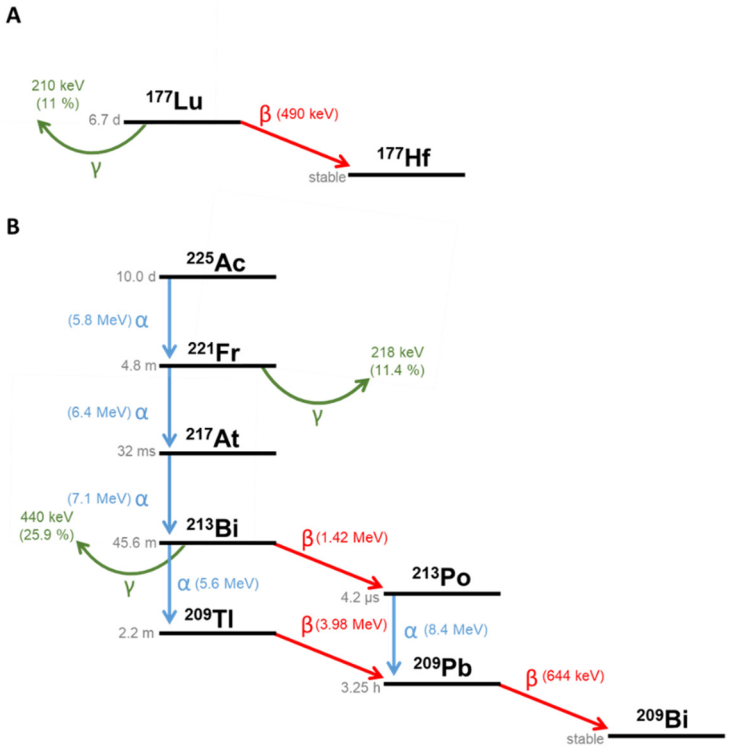


Figure 1.1 Isotope decay schemes for $^{177}$Lu and $^{225}$Ac.

Alpha particles are of interest for targeted alpha therapy (TAT) due to higher energy deposition over a shorter tissue penetration range, causing more dense ionizations as compared with beta particles (*18,19*). As shown in Figure 1B, $^{225}$Ac decays via multiple alpha particles – each capable of inducing irreparable DNA double-strand breaks in cell nuclei.

Table 1.1 Physical properties of $^{177}$Lu and $^{225}$Ac (*20*)

| | **$^{177}$Lu** | **$^{225}$Ac** |
|---|---|---|
| Physical half-life (days) | 6.7 | 9.9 |
| Maximum Energy (MeV) | 0.49 (β-) | 5.6 – 8.4 (α) in decay chain |
| Range in tissue (mm) | 0.7 – 2.0 | 0.05 – 0.1 |
| Linear energy transfer (keV/μm) | 0.2 – 0.7 | 60 - 100 |
| Gamma emissions (% abundance) | 208 keV (11%) | 218 keV (11% Fr-221 daughter)<br>440 keV (26% Bi-213 daughter) |

As seen in Table 1.1, $^{225}$Ac decays with ten times greater energy than $^{177}$Lu in a much shorter path length (<0.1 mm). This leads to about 100 times greater linear energy transfer (energy deposited per unit distance) on the order of 100 keV/μm for the alpha particles (*3,21-23*). The short range of alpha particles of only a few cell diameters is attractive because it creates more localized dose deposition, therefore minimizing toxicities to surrounding healthy tissue. For this reason, it is postulated that alpha particles

will be most clinically beneficial in the settings where the need to spare surrounding tissue is of greater concern. While the higher density of ionizations is desirable in tumor targets, this inevitably leads to higher dose in non-target organs, leading to increased toxicity. Selection of a radionuclide for therapeutic purposes involves consideration of multiple factors beyond the physical decay parameters of the isotope, including patient-specific factors such as tumor burden, spread, and location.

### 1.3 Clinical Landscape

RNT using PSMA-targeting ligands is an emerging therapeutic option in men with metastatic castration-resistant prostate cancer (mCRPC). Given that the therapeutic radiopharmaceuticals are administered intravenously and circulated systemically, this is a suitable treatment option for treating metastatic disease. These patients would otherwise be ineligible for external beam radiation therapy (EBRT) or surgery due to the extent of metastatic disease. Treatment with systemic radiopharmaceuticals also brings about the theoretical advantage of treating disease that is below the detection limits of diagnostic imaging.

Response rates to $^{177}$Lu labeled with PSMA-617, as measured by >50% decline in serum biomarker prostate-specific antigen (PSA), vary across treatment studies and patient cohorts from 30 to 70% (*24-29*). Several clinical studies have shown therapeutic efficacy of PSMA RNT in delaying disease progression (*29-31*). With a tissue penetration range of <2mm, $^{177}$Lu beta particles are effective in de-bulking tumor masses (*3,32,33*). While treatment with $^{177}$Lu-PSMA-617 is largely well-tolerated with a favorable dosimetry

profile (*34-36*), in the setting of severe bone marrow infiltration, treatment with beta-emitters may be contraindicated due to the potential for hematologic toxicities (*33*). $^{225}$Ac, an alpha-emitter with 9.9 days half-life (see Table 1.1), has emerged as an alternative isotope with favorable therapeutic decay properties.

While fewer clinical studies have been conducted with $^{225}$Ac-PSMA-617, studies so far report biochemical response rates (>50% decline in PSA) ranging from 25% to over 90%, though patient cohorts, prior treatments, and treatment settings vary widely (*37-39*). Additionally, alpha particle therapy may be favoured in the treatment of microscopic metastatic disease and bone marrow infiltration due to the shorter range of alpha radiation (*40-43*). However, the same radiobiological features that make $^{225}$Ac attractive against tumors also present a tradeoff at the expense of higher-grade toxicities (*39*). The most significant adverse effect of alpha particle PSMA-targeted RNT is dry mouth (xerostomia), making the salivary glands a key dose-limiting organ (*44*). While the accumulation of PSMA ligands in salivary glands is still not well understood, it is believed to be the result of both non-specific and specific uptake mechanisms of PSMA ligands (*45-47*). While xerostomia from $^{177}$Lu therapy is often temporary and reversible, with $^{225}$Ac, there is a greater incidence of xerostomia, which can significantly diminish patient quality of life and lead to treatment discontinuation (*39,48,49*). The higher tolerability of $^{177}$Lu-PSMA-617 in contrast to the high tumor dose potential of $^{225}$Ac is a motivation for combined or “tandem” isotope approaches that could reduce toxicity while maintaining high tumor dose (*50*).

Despite the fact that ~90% of patients present with PSMA-positive lesions (*8*), around half of RNT mCRPC patients do not achieve a biochemical response (*27,51*). Reasons

for disease progression or patient relapse may include insufficient radiation dose delivery (due to low PSMA expression, insufficient administered activity, insufficient tumor retention time of the agent) or radio-resistance (tumor biology, mutations, DNA damage repair mechanisms) (*36,52-56*).

## 1.4 Dosimetry in Nuclear Medicine

The previous section describes the clinical reality that even though most patients do present with PSMA-positive lesions, PSMA RNT is not curative, and only around half of patients may achieve a significant biochemical response. Even in those patients who do respond, the disease almost inevitably relapses. One possible explanation is that the tumor targets are not receiving a sufficiently high radiation dose necessary to kill the cancer cells. This is where dosimetry may come into play to help move away from a one-size-fits-all approach to a more personalized treatment and hopefully improve response rates and response duration.

### 1.4.1 Dosimetry Calculation Fundamentals

Fundamentally, the absorbed dose is an established parameter used for quantifying the radiation safety and risk for both diagnostic and therapeutic applications of radiation. The absorbed dose is also intimately related to the radiobiological effects of radiation (*57*). Simply put, the dose is a measure of the energy absorbed by ionizing radiation per unit mass of the tissue or organ:

$$D = \frac{E_{total}}{m} \qquad \textit{(Eq. 1-1)}$$

where $D$ is the dose in units of Gray, $E_{total}$ is the energy in Joules, and $m$ is the tissue mass in kg (1 Gray = 1 Joule/kg).

Individualized dosimetry calculations for tumor targets and affected healthy tissues are a standard practice for every patient in external beam radiation therapy. One key difference between EBRT and RNT is the mechanism of radiation delivery. In EBRT, you need to know the precise location of a target lesion to accurately irradiate the tumor. In contrast to this, in RNT, the systemic delivery of radiation is based on a molecular phenotype that requires knowledge of the tumor biology to accurately target the cancerous tissue. These fundamental differences in dose delivery implore that the dose deposition and calculations are also different. For dosimetry of unsealed radiation sources, as is the case in RNT, it is useful to define a target and source framework as outlined by MIRD (Medical Internal Radiation Dose) formalism. A source organ (or any defined volume) is any region that accumulates activity, and a target organ is the recipient of radiation from any other source. The target also self-irradiates. The sources and targets can be any size – whole organs or as small as individual voxels depending on the application.

In Equation 1-1, the numerator is the total absorbed energy in a region of interest. To calculate this energy term, we first need to know the total number of decays of the isotope in each organ (also known as the cumulated activity, $\tilde{A}$) as well as the energy per decay for a given isotope, $E$. Lastly, we need to know the penetration of the radiation, or, how much of the energy released gets absorbed within the region. For example, if the

absorbed fraction ($\varphi$) is 1, all the energy emitted in a region is absorbed in that region (there is no crossfire-irradiation of other organs).

$$D = \frac{\tilde{A} \times E \times \varphi}{m} \qquad \textit{(Eq. 1-2)}$$

The energy emitted per disintegration is a physical property of the nuclide and therefore independent of the patient. However, the number of decays accumulated in a tumor, and the fraction of radiation absorbed by a target organ are patient-specific due to differences in biological washout. Further, the absorbed fraction, which can be defined as relating between a source and a target, depends on the type and energy of the radiation, the relative geometry, and the material that separates them. The total dose is therefore a sum of all contributions of energy deposited in nearby source organs to a target organ or tumor.

$$D = \frac{\tilde{A}_s \times E \times \varphi_{t \leftarrow s}}{m} \qquad \textit{(Eq. 1-3)}$$

where $\tilde{A}_s$ is the cumulated activity in a source and $\varphi_{t \leftarrow s}$ is the absorbed fraction from a source to a given target. A source organ can also itself be the defined target.

The calculation of the cumulated activity for an unsealed source is fundamentally a kinetic problem. The injected radioactivity distributes in the patient over time, and the uptake is not instantaneous. Furthermore, the radiopharmaceutical both decays with a physical half-life of the radionuclide and is removed by biological processes. Therefore, the radiation dose is governed by the decay properties of the radionuclide and the pharmacokinetic properties of the ligand. However, patient-specific biokinetics and target expression (including intensity and heterogeneity) will also affect

the cumulated activity (and therefore dose) in a patient-specific manner (*58*). Therefore, to calculate the cumulated activities of interest, quantitative imaging is required to identify the injected radiopharmaceutical activity biodistribution over time.

One imaging modality for follow-up imaging and activity quantification is planar scintigraphy. From the 2D patient projections, counts are quantified using the geometric mean (using the patient thickness known from computed tomography (CT) scans) and activity standards are used to quantify the camera sensitivity and quantify the detected counts. The main disadvantage of this approach is a susceptibility to overlapping activity structures along the same projection line. This could lead to dose over-estimations from including activity in a region in which the activity was not actually accumulated. Alternatively, single photon emission computed tomography (SPECT) imaging captures a 3D image of the patient, thus eliminating issues with overlapping structures. However, time constraints may not allow for whole body SPECT imaging (which can be more quickly acquired by planar imaging). If multiple time points of SPECT imaging are acquired, in theory, individual voxels can be followed for activity kinetics which allows voxel-level source and target framework. There is also a “hybrid” imaging approach for dosimetry which combines both planar and SPECT imaging. In this approach, serial planar images are used to define the biokinetics of the tracer in a given region; then, a quantitative SPECT scan is used to calibrate or scale the activity measurements. This method is somewhat of a compromise between the improved quantitative accuracy of SPECT and logistical time and equipment constraints.

Once the images are acquired and quantified, regions of interest (ROIs) for dosimetry purposes are segmented. This could include tumors and critical organs most

at risk of irradiation. From these images, we can then generate time-activity curves that describe the time-course distribution of the radiopharmaceutical. These curves are fit with models to interpolate and extrapolate beyond our measurements. The area under the curve, or integral, therefore represents the time-integrated cumulated activity (TIAC), or the total number of disintegrations occurring in a given region over time:

$$\tilde{A} = \int_0^\infty A(t)dt \qquad \textit{(Eq. 1-4)}$$

The last step in the dose calculation involves multiplying the cumulated activity by a term called the S-factor. The S-factor is the radiation transport factor which is unique to each isotope and source-target geometry:

$$S = \frac{E \times \varphi_{t \leftarrow s}}{m} \qquad \textit{(Eq. 1-5)}$$

At the organ level, S-factors are derived from computational phantoms assuming homogeneous activity distributions. These are typically used for population risk estimates since they use phantoms of an average male or female and are not usually used for patient specific dosimetry. For more personalized approaches, the gold standard, albeit most computationally intensive option, would be to perform Monte Carlo radiation transport simulations for each patient's individual geometry. There are also more simplified dose point kernels, which are spatially computed dose profiles from point sources that can be convolved with activity distributions to yield total absorbed dose estimates.

### 1.4.2 Dosimetry for PSMA-Targeted RNT

The current treatment paradigm in RNT is to treat with fixed activities for the same number of cycles at fixed intervals, occasionally empirically adjusting the activity based on body weight, number of lesions, or in subsequent cycles to comply with normal organ toxicity limits (*59*). To move away from a “one size fits all” approach to more individualized treatment, dosimetry can be used to devise safe therapeutic activities to deliver maximal tumor doses while delivering as low as achievable doses to non-target volumes. Furthermore, a directive from the European Atomic Energy Community Basic Safety Standards now mandates that “target volumes shall be individually planned” for all radiotherapeutic medical exposures (*60*). Several clinical studies have started to investigate potential dose-response relationships in RNT across multiple cancer types and targets. One study found that mean tumor absorbed doses after $^{177}$Lu-PSMA-617 were significantly higher in patients with >50% decline in PSA at 12 weeks after treatment (*36*). This study and others have also demonstrated that patient variation in tumor volume/burden had an impact on normal organ absorbed doses (*61,62*). Thereby, tumor sink effects provide another rationale for more personalized dosimetry. Despite the growing body of evidence that absorbed doses in RNT correlate with efficacy and toxicity (*58*), dosimetry is still rarely performed (*59*). The research presented in this dissertation is driven by a motivation to incorporate dosimetry in translational RNT research and understand how dosimetry can be utilized towards improving patient outcomes.

## 1.5 Specific Aims

The overall goal of this dissertation is to integrate dosimetry into translational PSMA-targeted theranostics research. Dosimetric evaluation of PSMA RNT in preclinical studies, for new imaging tracers, and finally for therapeutic agents are the foundations of the specific aims of this work.

Specific Aim 1: To optimize preclinical PSMA RNT efficacy. The first aim uses various in vivo murine models of prostate cancer to investigate the therapeutic efficacy of single agent $^{177}$Lu and $^{225}$Ac PSMA RNT, as well as combination isotope approaches. Treatment efficacy is assessed against different lesion sizes and at various progressive stages of disease. Finally, a novel PSMA targeting ligand is evaluated by biodistribution, dosimetry, and treatment efficacy studies. This aim is addressed in Chapters 2 - 4.

Specific Aim 2: To evaluate the radiation dosimetry profile of new imaging theranostic tracers. The second aim addresses the dosimetry and radiation safety of two novel imaging tracers with application in metastatic prostate cancer evaluated in clinical cohorts. This specific aim is discussed in Chapters 5 and 6 of the dissertation.

Specific Aim 3: To determine tumor and organ absorbed doses for therapeutic PSMA RNT agents. The final aim determines the personalized radiation doses from therapeutic $^{177}$Lu-PSMA-617 treatments in a clinical cohort. Additionally, existing $^{177}$Lu PSMA dosimetry for a different PSMA targeting ligand is extrapolated to $^{225}$Ac for TAT dose estimates. Chapters 7 and 8 address the third specific aim.

This dissertation addresses two overarching goals: i) to identify preclinically and clinically relevant differences between $^{177}$Lu and $^{225}$Ac by incorporating dosimetry in

translational RNT research, and ii) to evaluate the clinical dosimetry of imaging and therapy theranostic agents.

### 1.6 Thesis at a Glance

Chapter 2: Development of a mouse model of disseminated prostate cancer

**Purpose:** To characterize a translatable mouse model of disseminated prostate cancer and evaluate TAT using this model.

**Methods:** Bioluminescence and immunohistochemistry were used to characterize the model prior to in vivo treatment studies. Treatment efficacy was evaluated by tumor growth kinetics and overall survival after treatment with $^{225}$Ac-PSMA-617 at two intervention times.

**Conclusion:** We developed a reproducible model of aggressive widespread prostate cancer achieved by intracardiac inoculation of cells. When this model is treated with $^{225}$Ac-PSMA-617, earlier intervention times lead to superior efficacy, corroborating the effectiveness of TAT against micrometastatic lesions.

Chapter 3: Testing isotope combination therapeutic approaches

**Purpose:** To compare RNT efficacy using alpha ($^{225}$Ac) versus beta ($^{177}$Lu) particle radiation, as well as a combination of both isotopes.

**Methods:** Biodistribution and tumor dosimetry studies were carried out in a subcutaneous model. Treatment efficacy of single agent versus a combination regime in a disseminated

model of disease with varying lesion sizes was evaluated using tumor growth kinetics and survival.

**Conclusion:** Treatment with $^{177}$Lu alone was ineffective against micrometastatic disease, while the most significant tumor growth retardation and survival benefits were observed with the single agent $^{225}$Ac and tandem approaches.

Chapter 4: Evaluation of a novel PSMA ligand with extended circulation time

**Purpose:** To evaluate PSMA-TO-1, a new PSMA-targeting ligand with longer circulation time

**Methods:** Comparison of tracer uptake by positron emission tomography (PET) imaging, long-term biodistribution using $^{177}$Lu, and a treatment study using $^{225}$Ac in our metastatic prostate cancer model.

**Conclusion:** Higher tumor uptake was achieved with PSMA-TO-1 compared with PSMA-617; however, this was accompanied by higher uptake in kidneys. Mice treated with $^{225}$Ac-PSMA-TO-1 conferred a significant survival benefit over those treated with $^{225}$Ac-PSMA-617.

Chapter 5: Radiation dosimetry of a new pan-cancer imaging agent

**Purpose:** To assess the dosimetry profile and biodistribution of $^{68}$Ga-FAPI-46, a new theranostic agent targeting cancer-associated fibroblasts.

**Methods:** Retrospective dosimetry analysis of 6 patients with various cancers based on 3 serial PET/CT scans following tracer administration.

**Conclusion:** $^{68}$Ga-FAPI-46 was shown to have a safe dosimetry profile for imaging, with increasing tumor-to-background ratios over time.

Chapter 6: Assessing feasibility of a $^{99m}$Tc-labelled PSMA tracer

**Purpose:** To calculate the dosimetry profile of $^{99m}$Tc-PSMA-I&S, a PSMA-targeting ligand for application in gamma imaging and radioguided surgery.

**Methods:** Retrospective dosimetry analysis of 4 healthy volunteers using a hybrid imaging method (5 sequential gamma planar imaging scans and one SPECT/CT).

**Conclusion:** Effective doses were deemed safe and comparable to other $^{99m}$Tc-labeled PSMA inhibitors. Early results from a clinical trial at UCLA using $^{99m}$Tc-PSMA-I&S for radioguided surgery of pelvic lymph node metastases are shown.

Chapter 7: Patient-specific radiation dosimetry of $^{177}$Lu-PSMA-617

**Purpose:** To quantify the patient-specific kidney and metastatic tumor absorbed doses in patients treated with $^{177}$Lu-PSMA-617.

**Methods:** Retrospective dosimetry evaluation of 49 patients (totaling 289 lesions) who were included in a phase 2 trial of $^{177}$Lu-PSMA-617 for mCRPC. Dose estimates are based on 4-5 serial gamma planar imaging scans and one quantitative SPECT/CT.

**Conclusion:** Kidney doses were regarded to be safe. We observed significant inter- and intra-patient variability in tumor doses, with a mean 10-fold increase in tumor doses compared to kidneys. This work is ongoing as more patients are included in the analysis.

Chapter 8 discusses opportunities for further research in RNT, including early and ongoing work from our group to extrapolate dose estimates for TAT. Chapter summaries and the dissertation conclusions are presented in Chapter 9.

# Chapter 2: Development of a mouse model of disseminated prostate cancer

A version of this chapter has been published: Meyer C*, Stuparu A*, Evans-Axelsson S, Lückerath K, Wei L, Kim W, Poddar S, Mona C, Dahlbom M, Girgis M, Radu CG, Czernin J, Slavik R. Targeted alpha therapy in a systemic mouse model of prostate cancer - a feasibility study. Theranostics. 2020; 10:2612-2620.

*Contributed equally

## 2.1 Introduction

The use of mouse models has aided in the discovery, mechanistic interrogation, and therapeutic developments for a wide range of cancers. Importantly, the choice of model is intricately related to the translatability of measurements and observations. Subcutaneously implanted xenograft tumor models allow for easy tumor and treatment response monitoring. Previous work in our group established PSMA RNT in a subcutaneous mouse model of prostate cancer (*63*). However, subcutaneous tumor models fail to provide information about metastatic disease. Orthotopic tumor models more closely replicate the tissue-specific microenvironment and may model metastatic progression, but are more difficult to establish and monitor (*64-69*).

Systemic cancer mouse models, achieved via intracardiac inoculation to introduce cells into circulation, are better suited to create lesions varying both in size and location, thus more accurately recapitulating the disease state of mCRPC (*65,69,70*). One particularly useful application for metastatic tumor models is in response evaluation to

alpha particle treatments. These models more faithfully represent the setting in which treatment with alpha particles would actually be clinically warranted. Yet, these systemic models are rarely used for therapeutic efficacy studies with only few reports for RNT (*71-73*). The objective of the following experiments was to establish a disseminated model of prostate cancer for studying the efficacy of $^{225}$Ac-PSMA-617 against different metastatic patterns and stages of the disease.

Several human cell lines are commonly used for murine prostate cancer models. The most commonly used cell lines are the PC3 (derived from bone metastasis) and DU145 (derived from a brain metastasis) cells, and the LNCaP (derived from a lymph node metastasis) cell line, as well as derivatives of these cells (*74,75*).

We selected 3 cell lines that endogenously express PSMA to test their suitability for intracardiac inoculations and development of widespread disease patterns. The first is C4-2, a LNCaP subline known to develop metastases in vivo (*69,77,78*). The C4-2 cell line has been shown to respond well to PSMA-targeted RNT in a subcutaneous model, but disease relapses in a dose-dependent manner within weeks of treatment (*79*). We also tested C4-2B cells, which are C4-2 cells collected from bone metastases, potentially providing a different metastatic pattern than the parental C4-2 cells (*80-82*). Lastly, we selected 22Rv1, another human prostate carcinoma cell line (*83,84*). To our knowledge, this is the first report characterizing intracardiac inoculations of these cell lines and evaluation of the treatment efficacy of $^{225}$Ac-PSMA-617 at different stages of disease progression.

## 2.2 Materials and Methods

### 2.2.1 Cell Culture

C4-2 and C4-2B cells were provided by Dr. George Thalmann (Department of Urology, Inselspital Bern). 22Rv1 cells were purchased from American Type Culture Collection. Cells were thawed one week prior to inoculation and were maintained in Roswell Park Memorial Institute 1640 medium supplemented with 10% fetal bovine serum (Omega Scientific) at 37°C and 5% CO2. Cells were monitored on a regular basis for mycoplasma contamination using the Venor GeM mycoplasma detection kit (Sigma Aldrich). The parental cells were engineered to express firefly luciferase by transduction with an amphotropic retrovirus encoding enhanced firefly luciferase followed by fluorescence activated cell sorting of transduced cells.

### 2.2.2 Animal Studies

All animal studies were approved by the UCLA Animal Research Committee (#2005-090). Male, 6-8 weeks old NOD scid gamma (NSG) mice were obtained from the UCLA Radiation Oncology Animal Core. Mice were housed under pathogen-free conditions with food and water ad libitum, and a 12-12 hour light-dark cycle. Veterinarian staff and investigators observed the mice daily to ensure animal welfare and determine if humane endpoints (e.g., hunched and ruffled appearance, apathy, ulceration, severe weight loss, tumor burden) were reached. The mice were inoculated with either firefly luciferase expressing C4-2 (500k cells/mouse), C4-2B (500k cells/mouse), or 22Rv1

(100k cells/mouse) cells into the left ventricle of the heart under anesthesia (2% isoflurane).

The cells were trypsinized, filtered through a 40 μm cell strainer, spun down, and resuspended in media and 50 mg/mL D-luciferin in a ratio of 1:1 to enable post-inoculation bioluminescence imaging (BLI). A successful injection was judged by both bright red blood pumping into the syringe at the end of the inoculation, as well as whole-body BLI signal 10-15 min post-inoculation. Mice with focal thoracic bioluminescence signal, indicative of a failed injection, were not included in the treatment study. Disease burden and spread were monitored weekly using BLI. Mice were randomized into treatment groups based on whole-body BLI radiance.

Mice weighed (mean ± SD) 26.3 ± 1.4 g (control), 26.4 ± 1.4 g (early treatment), and 27.9 ± 1.6 g (late treatment) at study start, and 23.1 ± 1.7 g (control), 23.2 ± 1.9 g (early treatment), and 24.7 ± 3.3 g (late treatment) at the last time point all mice were alive. Mice were sacrificed when they exhibited weight loss (>20%) and showed signs of deteriorating health due to the metastatic burden, such as hunching, dehydration, and labored breathing. The overall condition of the animals was assessed using the body conditioning score (*85*). A drop in score from 3 (well-conditioned mouse) to 2 (underconditioned; segmentation of vertebral column evident, dorsal pelvic bones palpable) warranted euthanasia. At sacrifice, organs were inspected for visible metastases and imaged *ex vivo* by BLI for metastatic burden quantification. The organs that showed BLI signal above background were stored in formalin and then paraffin-embedded for hematoxylin and eosin (H&E) staining.

In a separate experiment, five mice were sacrificed at either 1, 3, 4, 5, or 6 weeks after inoculation with C4-2 cells for *ex vivo* metastatic characterization. Again, all organs that showed BLI signal greater than background were retained for H&E staining.

### 2.2.3 Intracardiac Injections

To guide the syringe for intracardiac inoculations, we marked the sternal notch, the top of the xyphoid process, and the midpoint. Prior to injection, we drew a small bubble of air into the syringe to allow visualization of the cardiac pulse followed by drawing 100 µL of cell suspension (*86*). The needle insertion was performed slightly to the left of the midway mark on the sternum, directed to the left ventricle of the heart. Success of left ventricular needle insertion was judged by pulsating bright red blood in the syringe. The cells were then injected slowly over a period of about 30 seconds. At the end of the injection, the syringe plunger was slightly pulled back to draw a minimal amount of blood into the syringe. This prevents cells spilling into the chest cavity during the needle removal and provides proof that the needle was still positioned correctly in the left ventricle. After needle removal, gentle pressure was applied to the chest of the mouse for about a minute to reduce bleeding. Mice were monitored closely for any signs of distress post-injection.

### 2.2.4 Bioluminescence and $^{68}$Ga-PSMA-11 PET/CT imaging

Metastatic disease burden and spread were quantified with weekly BLI using a Xenogen IVIS 100 imaging system (Perkin Elmer). The mice were subcutaneously injected with 150 mg/kg D-luciferin (50 mg/mL) and after 15 minutes, imaged in the supine

position. Living Image software was used to quantify whole body radiance as a measure of disease burden. GraphPad Prism 8 was used to analyze radiance data and generate survival plots. The Log-rank (Mantel-Cox) test was used for survival analysis.

$^{68}$Ga-PSMA-11 was synthesized by eluting gallium-68 from a $^{68}$Ge/$^{68}$Ga generator (Eckert & Ziegler) with 0.1 M hydrochloric acid, trapping $^{68}$Ga on a cationic exchange cartridge and eluting with 5 M sodium chloride solution. 5 µg PSMA-11 in HEPES buffer were reacted with 68GaCl3 for 5 min at 95°C. Radiochemical identity and purity were confirmed before application by radiographic thin-layer chromatography. For PET/CT, ~1.1 MBq $^{68}$Ga-PSMA-11 in 100 µL volume was injected into the tail vein and images were acquired 1 hour later using the preclinical Genisys 8 PET/CT scanner (Sofie Biosciences). Attenuation-corrected images were reconstructed using maximum-likelihood expectation maximization with 60 iterations. The following parameters were applied for CT imaging: 40 kVp, 190 mA, 720 projections, and 55 ms exposure time per projection. The resulting PET/CT images were analyzed using VivoQuant Imaging Software (Invicro).

### 2.2.5 Targeted Alpha Therapy with $^{225}$Ac-PSMA-617

$^{225}$Ac was supplied by the Isotope Program within the Office of Nuclear Physics in the Department of Energy's Office of Science. $^{225}Ac(NO_3)_3$ was dissolved in 0.1 M HCl and mixed with PSMA-617 in 1 M NaOAc containing 10 mg/mL gentisic acid, resulting in a final reaction pH ~5.5. Labeling for 30 min at 90 °C provided $^{225}$Ac-PSMA-617 in a purity of at least 92% by radio-thin layer chromatography at a molar activity of 130 MBq/µmol.

After dilution with normal saline, mice (n=10 mice/group) were injected intravenously with 40 kBq $^{225}$Ac-PSMA-617 at either 1 or 3 weeks after cancer cell inoculation. Control mice (n=10 mice) were left untreated.

### 2.2.6 Tissue Analysis

All tissue analysis was performed by the UCLA translational pathology core laboratory. Tissue samples were fixed overnight in 10% PBS-buffered formalin and transferred to 70% ethanol for storage before paraffin embedding. Paraffin-embedded tissues were sectioned into 4 μm slices and stained with H&E. For anti-PSMA antibody staining, tissue sections were de-paraffinized and re-hydrated. Endogenous peroxidase was blocked (3% hydrogen peroxide/methanol, 10 min.). Antigens were retrieved in heated 0.01 M citrate buffer, pH 6.0 (95ºC, 25 min.). Specimens were incubated overnight at 4°C with an anti-PSMA antibody (clone 3E6; 1:50, DAKO, M362029-2) in bovine serum albumin. For detection, the Dakocytomation Envision System labeled polymer horseradish peroxidase (DakoCytomation, Carpinteria) and the diaminobenzidine reaction (#BDB2004 L; Biocare Medical) were used according to the manufacturers' instructions. The sections were counterstained with hematoxylin.

## 2.3 Results

### 2.3.1 Model Characterization for Different Cell Lines

C4-2 cells: Intracardiac inoculation of C4-2-luc cells led to liver micrometastases after one week. Smaller extra-hepatic metastatic sites were difficult to detect in vivo by BLI given the high intensity signal from the liver (Figure 2.1).

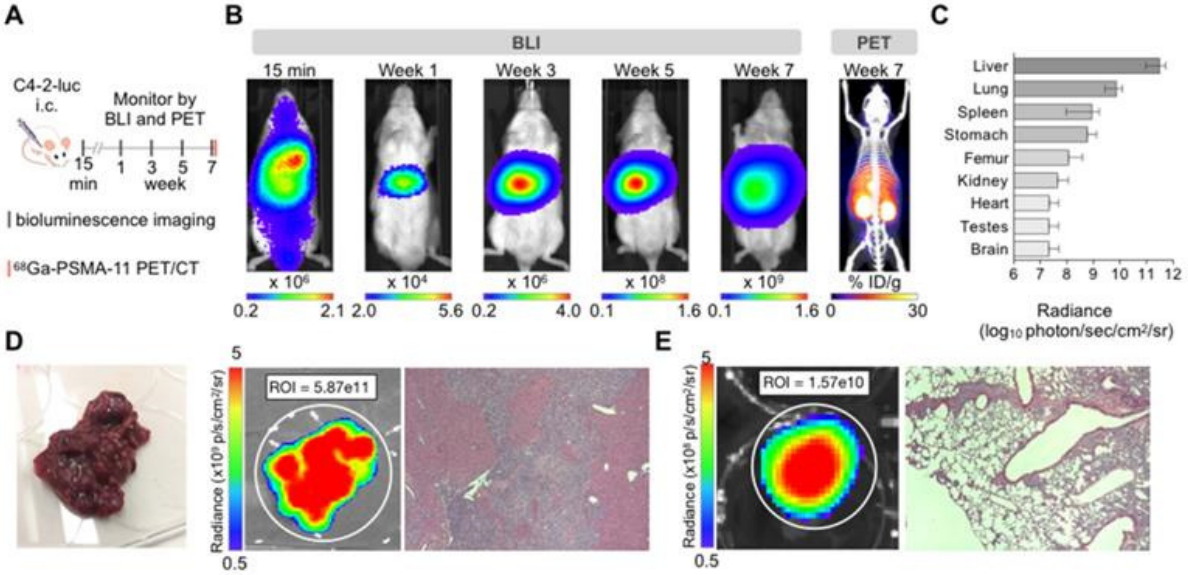


Figure 2.1 Characterization of the C4-2 intracardiac systemic tumor model. (A) Experimental design. (B) In vivo BLI over time of an untreated mouse inoculated by intracardiac injection and $^{68}$Ga-PSMA-11 PET/CT at 7 weeks. (C) Tumor burden as measured by ex vivo bioluminescence radiance (photons/second/cm2/sr) for individual organs 7-9 weeks post-inoculation (mean ± SD, n=10 mice). (D) Liver disease burden was visible by eye, BLI, and H&E staining in all mice. (E) Lung metastases were only visible by BLI and H&E staining.

Serial ex vivo analysis revealed visible macroscopic liver lesions as early as four weeks post-inoculation with the BLI signal, number, and size of lesions increasing over time. In addition, H&E staining revealed liver lesions otherwise non-visible by eye in 4/5 mice sacrificed at 1 week or 3 weeks post inoculation. The number of lesions and size may be underestimated due to the small number of slices. Seven weeks after inoculation, at the time of body score deterioration and subsequent sacrifice, multiple liver metastases

were visible by eye (Figure 2.1D). The presence of the C4-2 metastases was verified by $^{68}$Ga-PSMA-11 PET/CT before sacrifice, ex vivo BLI following sacrifice, and H&E staining. Ex vivo analysis revealed other metastatic sites such as the lungs, spleen, stomach, bone, and brain 7 weeks post-inoculation (Figure 2.1E and Figure 2.2).

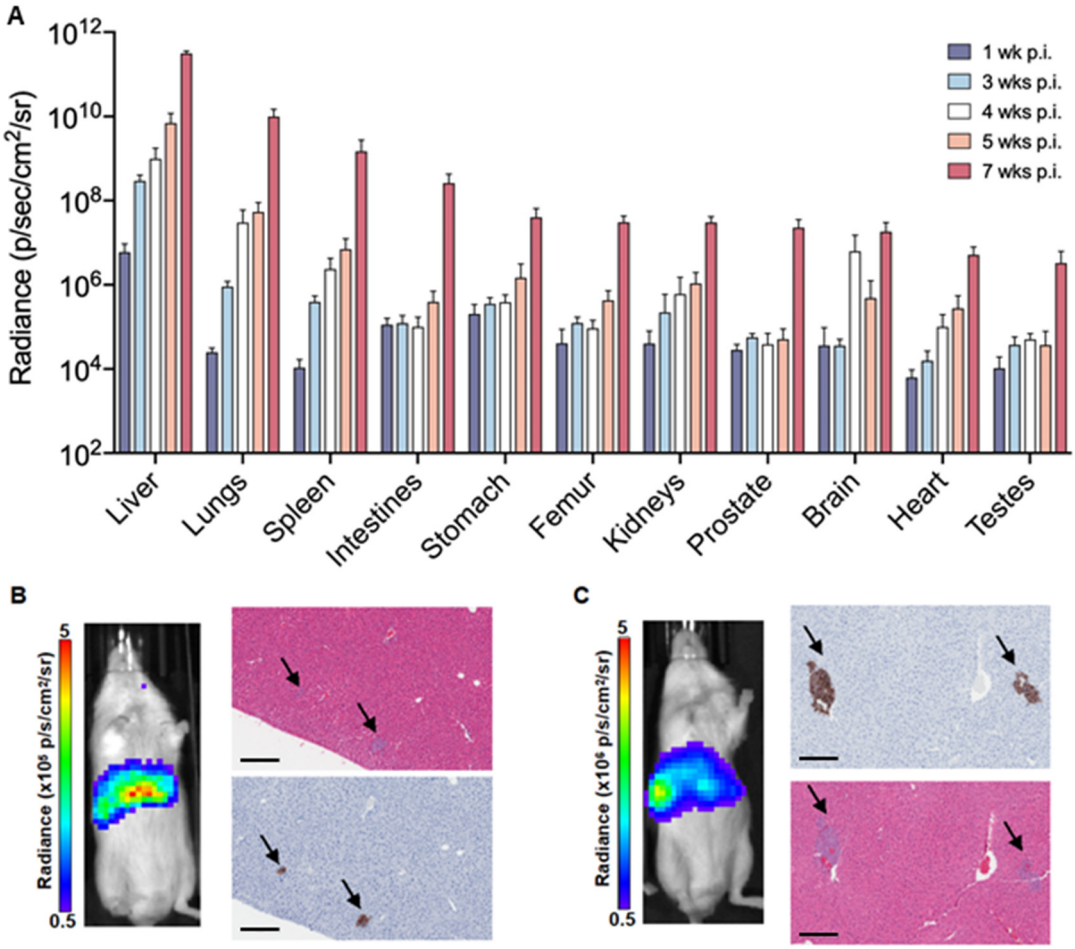


Figure 2.2 C4-2 lesion distribution over time**.** (A) Ex vivo bioluminescence imaging shows increasing disease burden over time. Liver tumor burden is detectable by whole body BLI, anti-PSMA IHC, and H&E staining at 1 week (B), and 3 weeks (C), respectively. The depicted H&E and anti-PSMA sections have 10x magnification and a scale bar of 200 µm. Black arrows indicate lesions.

22Rv1 cells: 22Rv1 intracardiac inoculation led to the formation of visible macroscopic metastases in liver, adrenal glands, and kidney in all mice 5 weeks post-inoculation. Additional lesions were detected in lung and bones by ex vivo BLI. Thus, intracardiac 22Rv1 cell administration provided a robust metastatic model. However, we chose the C4-2 model for further therapy studies due to low, if any, kidney disease burden. The 22Rv1 model yielded 100-fold greater radiance in the kidneys as compared to the C4-2 model. The high metastatic burden in kidney and adrenal glands seen in the 22Rv1 model may interfere with assessment of off-target organ toxicity, and the model did not yield any additional sites or patterns of disease not already produced by the C4-2 cells.

C4-2B cells: The success rate of inoculations for the C4-2B model was too low to robustly assess metastatic spread and tumor burden.

### 2.3.2 Treatment Efficacy of $^{225}$Ac-PSMA-617 RNT

To investigate treatment response as a function of disease burden, mice were treated with 40 kBq of $^{225}$Ac-PSMA-617 at either one week (early treatment cohort) or three weeks (late treatment cohort) after intracardiac injection with C4-2 cells. This treatment activity was chosen as it is well-tolerated and efficacious in a subcutaneous mouse model (*56*). Both early and late treatment resulted in a significant survival benefit (27 vs. 13 weeks median survival; $p<0.001$) compared to untreated mice (7 weeks). Disease remained stable in the early and late treatment groups for 8 and 3 weeks, respectively (Figure 2.3).

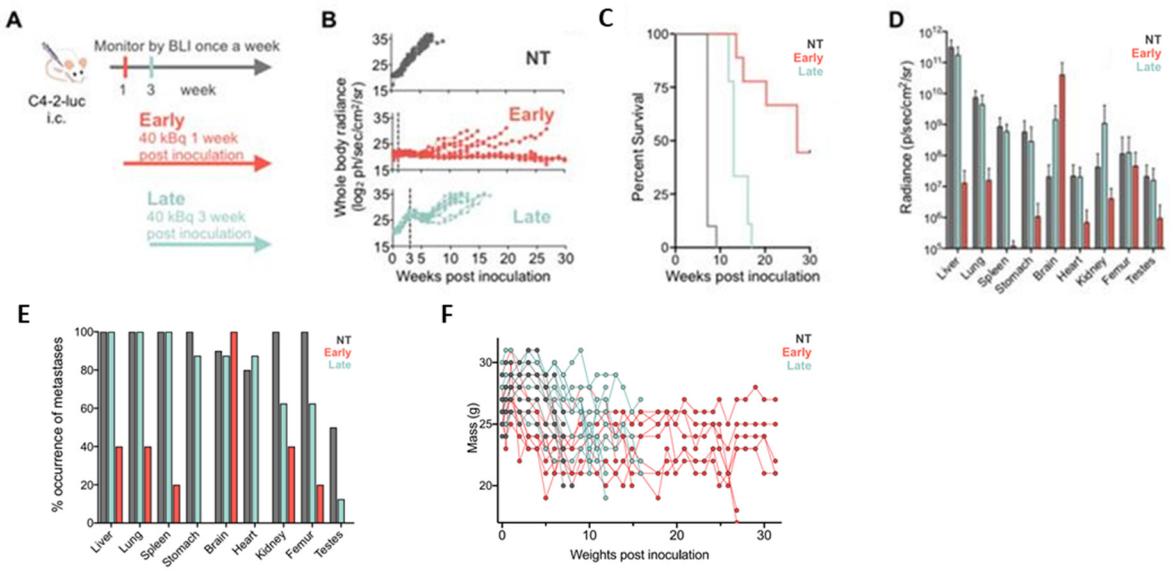


Figure 2.3 $^{225}$Ac-PSMA-617 RNT in a systemic mouse model. (A) Experimental design. (B) Individual whole-body radiance growth curves following one cycle of 40 kBq $^{225}$Ac-PSMA-617 either 1 week (early) or 3 weeks (late) post-inoculation (n=10 mice per group). (C) Survival plot. Median survival was 7 weeks (NT), 27 weeks (early treatment), and 13 weeks (late treatment), (NT vs. early treatment, $p<0.0001$; NT vs. late treatment, $p<0.0001$; early vs. late treatment, $p<0.001$). (D) Mean whole organ radiance measured ex vivo at time of sacrifice (mean ± SD for 10 mice for NT, 8 mice for late treatment and 5 mice for early treatment). (E) Percent occurrence of lesions in various tissues using a 600 counts BLI threshold (above background). (F) Individual mouse weights during the treatment study. NT = untreated.

Disease recurred uniformly after 3 weeks in all mice of the late treatment group. In contrast, disease recurred later (week 8) and only in 4/9 mice of the early treatment cohort. At termination of the study 30 weeks post-inoculation, 4/9 mice in the early treatment cohort showed stable whole body tumor burden. One mouse was sacrificed at 27 weeks post-inoculation due to rapid 20% weight loss despite non-detectable whole-body disease burden by in vivo imaging. Ex vivo, disease was detected in the femur, brain, and liver. All untreated and late treatment mice had extensive liver involvement at

the time of sacrifice (Figure 2.3E and Figure 2.4). However, the late treatment cohort had more extensive brain involvement than the untreated controls (Figure 2.3D). The early treatment cohort had significantly more brain involvement as compared to both late treatment cohort and the untreated controls, possibly due to the fact that mice survived longer, allowing further progression. Liver lesions occurred less frequently in mice treated at the earlier time point (Figure 2.3E). All mice exhibited sudden and rapid weight loss around their time of sacrifice.

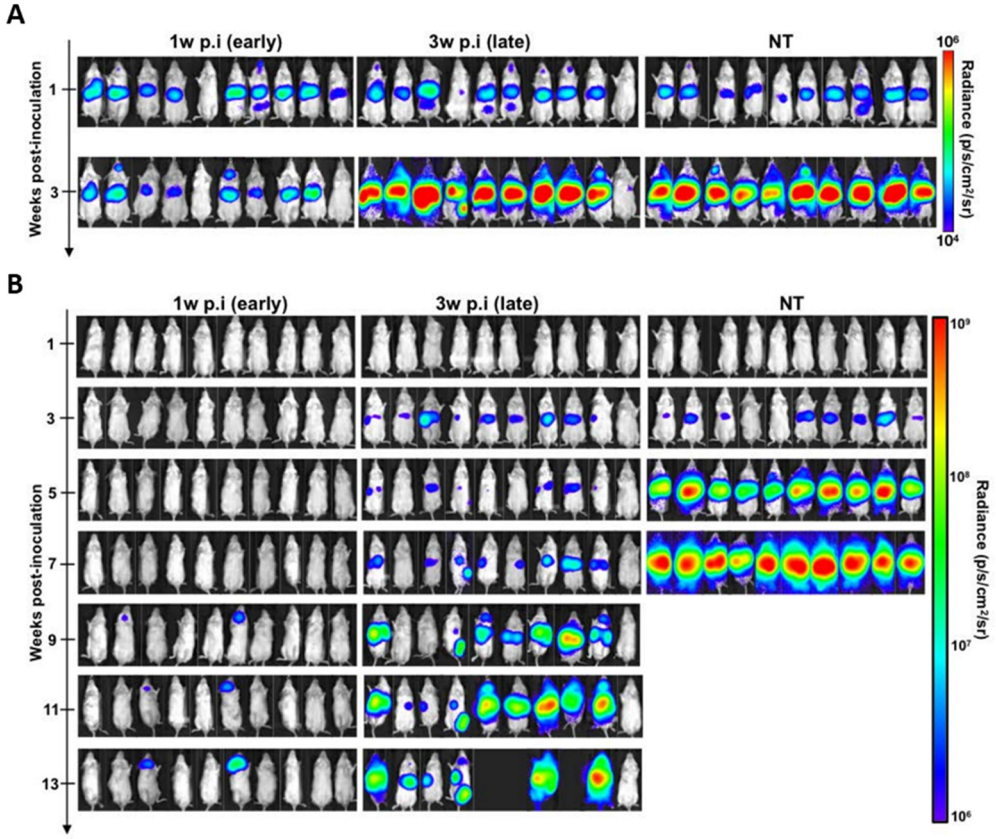


Figure 2.4 Bioluminescence images of NSG mice treated with $^{225}$Ac-PSMA-617 RNT. (A) Bioluminescence images at the time of treatment. All but one mouse in each treatment group showed significant tumor burden at the time of treatment. These mice were excluded from analysis. (B) Treatment, either at 1 week or 3 weeks after inoculation, reduces tumor burden and increases survival as compared to untreated (NT) control mice.

While not as sensitive as BLI for metastatic disease burden detection, PET/CT imaging confirmed the differential tumor burden in the control versus treated mice (Figure 2.5). $^{68}$Ga-PSMA-11 PET/CT imaging was used to confirm PSMA expression over time, as BLI cannot be used for this purpose. PET/CT images acquired 7 weeks post-inoculation showed high hepatic disease burden in control mice, with no detectable metastases in the early and late treatment cohorts. Brain lesions were detected in 3/6 late treatment as well as in 2/3 early treatment mice imaged by $^{68}$Ga-PSMA-11 PET/CT 12 weeks post-inoculation (Figure 2.6).

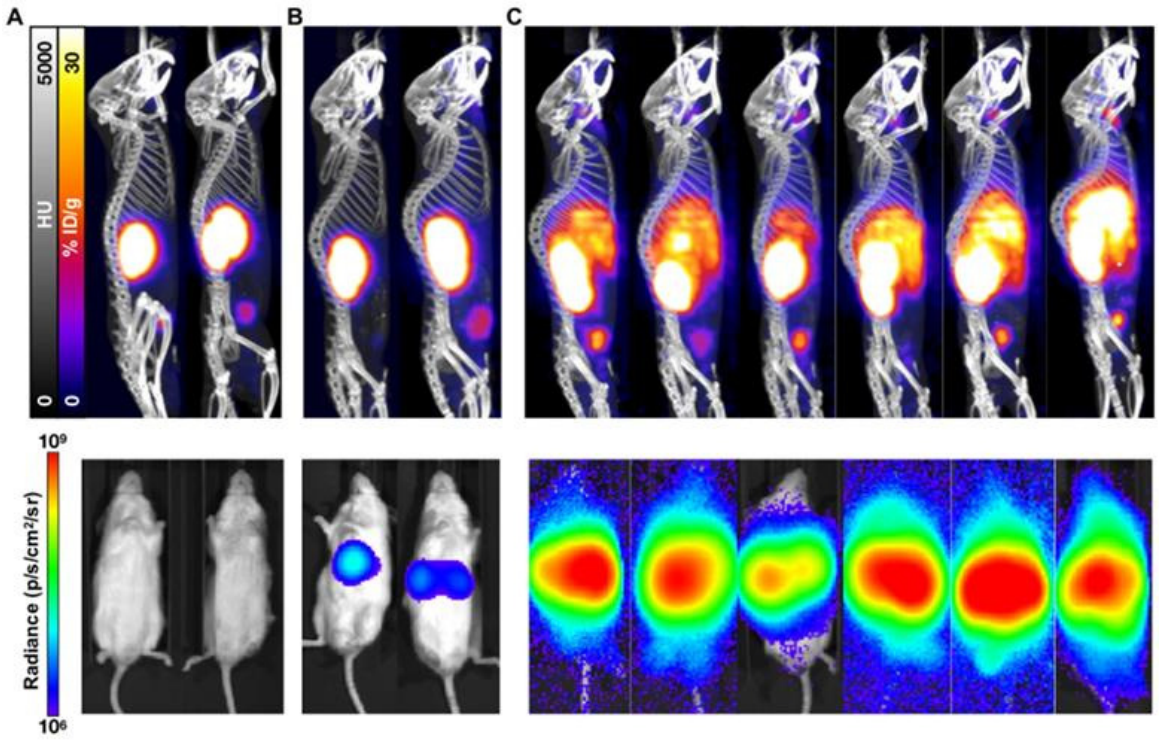


Figure 2.5 PET/CT and BLI characterization 7 weeks post-inoculation of C4-2 cells. Representative mice treated with 40 kBq of $^{225}$Ac-PSMA-617 at (A) 1 week (early treatment cohort), or (B) 3 weeks (late treatment cohort) post-inoculation, and (C) untreated control mice were imaged using $^{68}$Ga-PSMA-11 and BLI. Images show detectable liver disease in control mice by both PET/CT and BLI, but only by BLI for the late treatment cohort. No detectable disease was observed for the early treatment mice.

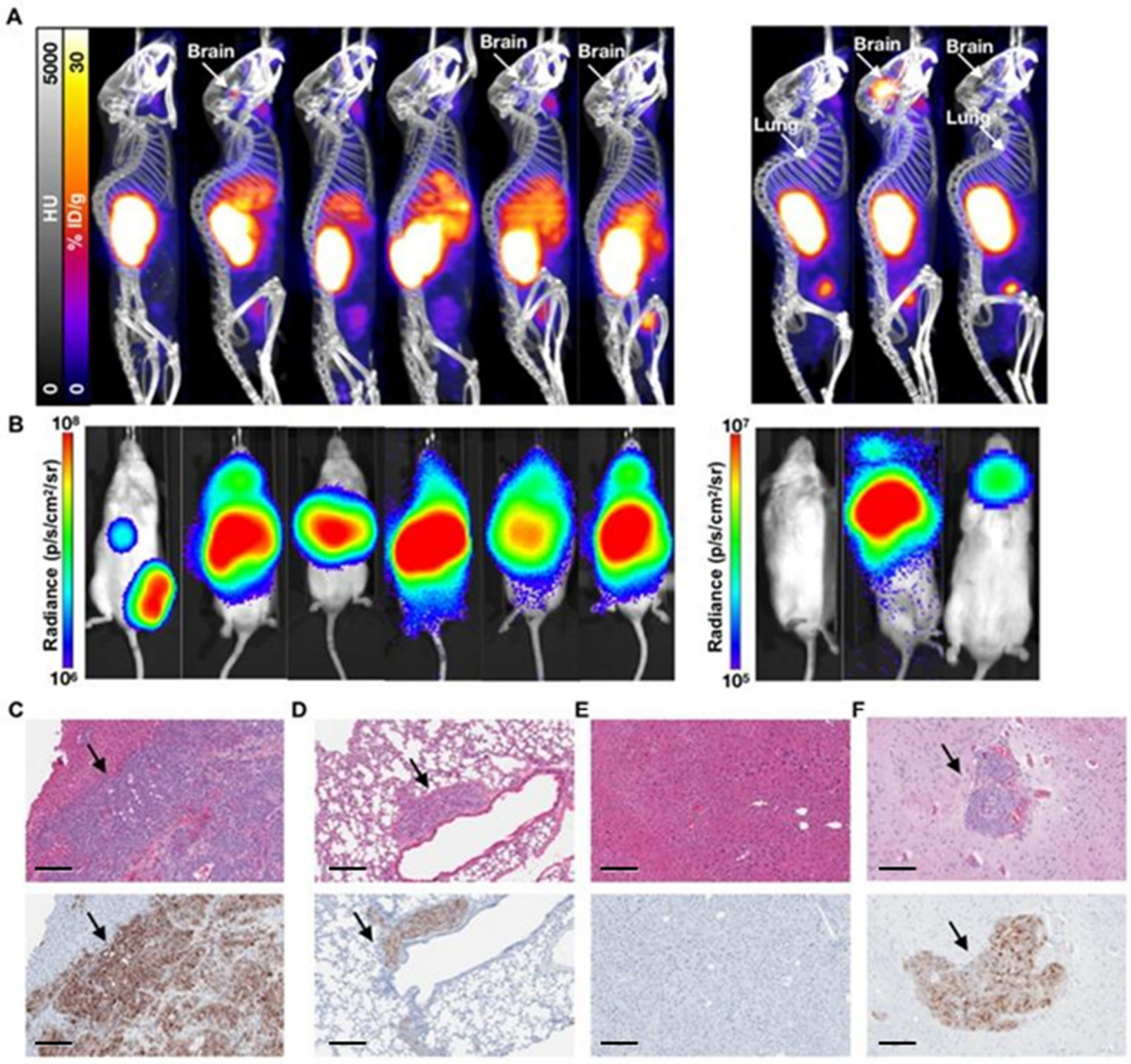


Figure 2.6 Characterization of the early and late treatment groups. (A) $^{68}$Ga-PSMA-11 PET/CT imaging of six mice from the 3 week (late) p.i. treatment group at 80 days post treatment and three mice from the 1 week (early) p.i. group at 144 days post treatment. (B) Corresponding in vivo bioluminescence images of the mice at 78 and 141 days post treatment, respectively. Most mice showed various degrees of liver involvement, with one mouse showing focal uptake in the left femur (not visible by PET/CT) and four mice showing significant brain disease. (C) H&E and anti-PSMA IHC staining of liver and (D) lung slices from a late treatment mouse. (E) H&E and anti-PSMA IHC staining of liver and (F) brain from a representative early treatment mouse. The depicted H&E and anti-PSMA sections have a 10x magnification and a scale bar of 200 μm. Black arrows indicate metastases.

## 2.4 Discussion

This chapter describes the development of a mCRPC mouse model suitable for monitoring PSMA-targeted RNT at various disease stages of disseminated disease. To achieve this, we performed intracardiac inoculations of C4-2, C4-2B, and 22Rv1 human prostate cancer cell lines. Disease burden and metastatic spread were monitored using BLI and $^{68}$Ga-PSMA-11 PET/CT. We found C4-2 to be the most suitable cell line as it led to the formation of consistent visceral tissue and bone metastases. Whereas 22Rv1 cells produce metastases similarly to C4-2, they also form adrenal and kidney metastases, making it harder to assess possible treatment-induced kidney toxicity. To date, our efforts to establish a reliable C4-2B metastatic model have not been successful. The C4-2B cells may be better suited for intratibial inoculations where the aim would be to assess RNT purely in bone metastases (*86,87*).

In a proof-of-concept treatment study, we show that treatment in the C4-2 metastatic model at an earlier intervention time with lower disease burden results in better outcomes. However, brain metastases impede even longer survival. This could be due to insufficient radiation dose delivered to the brain through poor blood brain barrier penetration, or the dose being mostly delivered to the liver, the organ with the highest disease burden due to sink effects. The significant survival benefit from early treatment supports the current efforts to treat patients with PSMA-targeted RNT earlier and before other treatment options such as chemotherapy and androgen deprivation therapy (ADT) (*37,88*). Our model suggests that treating at a micrometastatic stage, before disease could be detected by PET/CT imaging, could improve outcomes. Treatment at a higher

tumor burden is still efficacious with an overall median survival of 13 weeks, as compared to 7 weeks without treatment. Similar to controls, the late treatment cohort succumbed to high hepatic disease burden. The inability to sufficiently reduce the liver disease may be due to insufficient radiation dose delivered to the tumor, or metastatic lesions being too large for treatment with short-range alpha particles. It is possible that a combination of both alpha- and beta-targeted therapy will yield improved outcomes in patients with bulkier lesions.

The C4-2 metastatic model does differ in the pattern of metastases formation (primarily liver, but also in lungs, spleen, bone, and brain) from typical mCRPC patients who first develop lymph node and bone metastases, followed by visceral tissue metastases. However, patients with visceral metastases, especially lung and liver, have poor prognosis and do not respond well to $^{177}$Lu-PSMA-617 beta-targeted therapy (*27,89,90*). The high liver and lung metastatic tumor burden in our model makes it a useful representation of patients with visceral metastases. Our results suggest that $^{225}$Ac-PSMA-617 could delay progression even in settings with high visceral metastatic load. More data is required to show whether $^{225}$Ac-PSMA-617 can lead to better clinical responses than beta particle targeted therapy. To date, $^{225}$Ac-PSMA-617 is mostly used in patients with extensive bone disease since its shorter range in tissue will lead to lower bone marrow toxicity than seen with beta particle targeted therapy.

One limitation of our study is the lack of patient-derived xenograft (PDX) models, which are difficult to establish for prostate cancer. Further studies are warranted to test the viability of a systemic PDX model. Our model also does not recapitulate the impact of the immune system since human-derived cancer cell lines can only be used in immune-

deficient mice. Nevertheless, we believe this systemic model is more clinically relevant than subcutaneous xenograft models for treatment regimen efficacy and characterization studies.

## 2.5 Conclusion

In summary, we characterized the efficacy of PSMA-targeted alpha therapy in a disseminated prostate cancer mouse model. Our studies highlight that the treatment time has an impact on therapeutic effectiveness. Both 1- and 3-week treatment time points used in this study emphasize effectiveness of PSMA-targeted therapy even against visceral tissue metastases, which are more difficult to treat and are associated with a worse prognosis. In addition, the promising efficacy of $^{225}$Ac-PSMA-617 at a low disease burden, detectable by BLI, but not yet by PET/CT, suggests potential benefits for treating at a minimal residual disease stage. Further studies are warranted to compare differences between alpha- vs. beta-targeted therapy and to develop optimized combination therapies of radionuclides. For such studies, the use of a systemic model is preferred over used subcutaneous models.

# Chapter 3: Testing isotope combination therapeutic approaches

A version of this chapter has been presented at the 2020 SNMMI Annual Meeting and is the basis for a manuscript in preparation: Meyer C, Stuparu A, Wei L, Lückerath K, Czernin J, Slavik R, Dahlbom M. Tandem isotope therapy with $^{225}$Ac- and $^{177}$Lu-PSMA-617 in a murine model of prostate cancer. [Manuscript in preparation].

## 3.1 Introduction

Overall, clinical experiences using $^{177}$Lu or $^{225}$Ac have shown encouraging treatment responses; however, responses are not durable. Given that the dose-limiting tissue for the injected activity of $^{225}$Ac is the salivary glands, simply using higher $^{225}$Ac treatment activities to increase tumor dose delivery is not an option. Dual isotope combinations, or "tandem" approaches may provide the benefits of both $^{177}$Lu and $^{225}$Ac to improve treatment tolerability while retaining high tumor dose (*33,91*). Early clinical studies in both $^{177}$Lu-naïve patients and in those patients who progressed after $^{177}$Lu-PSMA have shown that augmentation of $^{177}$Lu-PSMA therapy with a boost of $^{225}$Ac is an effective treatment option with a more favourable side effects profile (*50,92*). No incidents of grade 3 or higher xerostomia were reported in these studies.

A similar approach has been tested in peptide receptor radionuclide therapy (PRRT) against neuroendocrine tumors using tandem $^{177}$Lu/$^{90}$Y-DOTATATE, combining two beta particle-emitting isotopes with different energies and tissue penetration ranges (*93,94*). In the preclinical setting, tandem $^{177}$Lu/$^{90}$Y-DOTATATE demonstrated a superior antitumor effect compared with either monotherapy alone (*95*). For PSMA-targeted

therapies, clinical data are still limited by small patient cohort sizes and to-date there are no systematic preclinical investigations into the efficacy of dual isotope combinations.

In the following study, we sought to directly compare alpha versus beta particle PSMA radionuclide therapy, as well as a combination thereof, in a mouse model of prostate cancer. First, we conducted activity escalation and dose-finding biodistribution studies to determine injected activities of $^{177}$Lu and $^{225}$Ac that yield equivalent tumor doses (*96,97*). We then treated mice bearing disseminated prostate cancer lesions at two different stages of disease with $^{177}$Lu- and $^{225}$Ac-PSMA-617 as single agents, or in combination, to compare therapeutic efficacy and survival.

## 3.2 Materials and Methods

### 3.2.1 Cell Culture and Animal Studies

In all studies, the C4-2 cell line was used. Details regarding cell culture and animal studies are as previously described in Section 2.2.1 and Section 2.2.2.

### 3.2.2 Radiopharmaceutical Synthesis

PSMA-617 precursor was obtained from ABX advanced biochemical compounds (Radeberg, Germany). $^{177}$Lu was obtained from Spectron MRC (South Bend, IN) and $^{225}$Ac was supplied by the U.S. Department of Energy's Isotope Program within the Office of Science. Radiolabeling was performed as previously described with molar activities of 84 GBq/μmol and 130 MBq/μmol for $^{177}$Lu- and $^{225}$Ac-PSMA-617, respectively (*63,98*).

### 3.2.3 $^{225}$Ac activity escalation study

This subsection has been published as part of the following publication: Stuparu A, Capri J, Meyer C, Le TM, Evans-Axelsson S, Current K, Lennox M, Mona C, Fendler WP, Calais J, Eiber M, Dahlbom M, Czernin J, Radu CG, Lückerath K, Slavik R. Mechanisms of resistance to PSMA-targeted radioligand therapy in a mouse model of prostate cancer. J Nucl Med. 2021; 62:989-995.

To optimize therapeutic activity of $^{225}$Ac- and $^{177}$Lu-PSMA RNT in mice, we used a subcutaneous C4-2 tumor model for a dose-finding activity escalation study. Immunodeficient, 6-8 weeks old NSG male mice were inoculated subcutaneously with 5x10$^6$ C4-2 cells in 100 µL matrigel into the shoulder region. The mice were randomized on the basis of tumor volume into 2 studies. Mice in study 1 were either untreated or received 30 or 120 MBq of $^{177}$Lu-PSMA-617 intravenously (6 mice per group), whereas mice in study 2 either were untreated or received 20,40, or 100 kBq of $^{225}$Ac-PSMA-617 intravenously (8 mice per group). Injected activities were based on previous publications (*56,98*). Therapeutic efficacy was assessed by tumor volume growth kinetics (study 1: caliper; study 2: CT), time to progression to half-maximal tumor volume (TTP), and survival.

### 3.2.4 Biodistribution and Tumor Dosimetry of $^{177}$Lu- and $^{225}$Ac-PSMA-617

Immunodeficient, 6-8 weeks old NSG male mice were inoculated subcutaneously with 5x10$^6$ C4-2 cells in 100 µL matrigel into the shoulder region (n=50 mice). After 3 weeks, when tumors reached ~300 mm$^3$ in volume, mice were treated with either 30 MBq

$^{177}$Lu-PSMA-617 (n=25 mice) or 40 kBq $^{225}$Ac-PSMA-617 (n=25 mice). The treatment activities were selected based on efficacious and well-tolerated activities in previous studies (*56*). Mice were sacrificed at 1, 4, 24, 48, and 168 hours following treatment (5 mice per time point for each nuclide). At the time of sacrifice, tumors and organs (including kidneys, liver, submandibular salivary glands, and intestines) were collected for *ex-vivo* gamma-counting for activity quantification ($^{177}$Lu energy window: 189-231 keV; $^{225}$Ac energy window: 170-260 keV for $^{221}$Fr daughter detection; Cobra II Auto-Gamma; Packard Instrument Co). Actinium samples were counted after 24 hours when secular equilibrium was reached. The multiple t-test method with Welch correction was used for biodistribution statistical comparisons (statistical significance set to ≤ 0.05).

We estimated tumor self-doses (ignoring cross-dose contributions from neighboring organs) by first curve-fitting and integrating the tumor time-activity curves (NUKFIT Software) (*99*). The total number of disintegrations was multiplied by dose constants to yield tumor doses for $^{177}$Lu and $^{225}$Ac ($2.838 \times 10^{-3}$ and $5.934 \times 10^{-1}$ Gy*g/[uCi*h], respectively). Dose constants are derived from nuclear data for energy released per disintegration of each radionuclide, ignoring contributions with a decay yield of <1% (*17,100*). In this case of self-dose calculation, it is assumed that all beta and alpha particle radiation has an absorption fraction of 1.0 and that all disintegrations measured in the tumor deposit all energy in the tumor. We can thereby estimate the injected activities of $^{177}$Lu- and $^{225}$Ac-PSMA-617 that yield approximately equivalent tumor doses for subsequent studies directly comparing single vs. dual isotope approaches.

### 3.2.5 Tandem $^{177}$Lu/$^{225}$Ac Therapy

All subsequent therapy studies were investigated in a mouse model of advanced metastatic prostate cancer, the development and characterization of which was described in Chapter 2. NSG mice were inoculated with C4-2-luc cells in the left biodistrib leading to disseminated visceral and bone lesions, as previously described (n=80 mice) (*98*). Mice were treated at two different stages of disease - either 3 or 5 weeks after inoculation with equivalent tumor dose-depositing activities of $^{177}$Lu- or $^{225}$Ac-PSMA-617 or in scaled combination (as determined by the tumor dose-finding study) using intravenous administration. The treatment groups were as follows: i) 35 MBq $^{177}$Lu-PSMA-617, ii) 40 kBq $^{225}$Ac-PSMA-617, iii) mixed 17 MBq $^{177}$Lu-PSMA-617 + 20 kBq $^{225}$Ac-PSMA-617, or, iv) untreated (n=10 mice per group per treatment time).

Disease burden was assessed by weekly luciferase-mediated BLI (Xenogen IVIS 100, Perkin Elmer) and mice were followed for overall survival. Mice were sacrificed when their overall condition showed signs of deteriorating health based on the body conditioning score (*85*). Therapeutic efficacy data, as measured by whole body radiance over time, were analyzed with one-way ANOVA with Bonferroni correction using GraphPad Prism 8. The Log-rank (Mantel-Cox) test was used for survival analysis.

## 3.3 Results

### 3.3.1 $^{225}$Ac Activity Escalation Study

To identify treatment activities resulting in the best antitumor effects without toxicity, mice were treated with varying activities of $^{225}$Ac- or $^{177}$Lu-PSMA-617. PSMA RNT

induced significant, dose-dependent tumor shrinkage and increased time to progression and survival (Figure 3.1). $^{225}$Ac-PSMA RNT with 100 kBq achieved the best tumor control, but the mice experienced toxicity as evidenced by a deteriorating condition leading to a humane endpoint, explaining their shorter survival. No severe weight loss was observed after $^{177}$Lu-PSMA RNT.

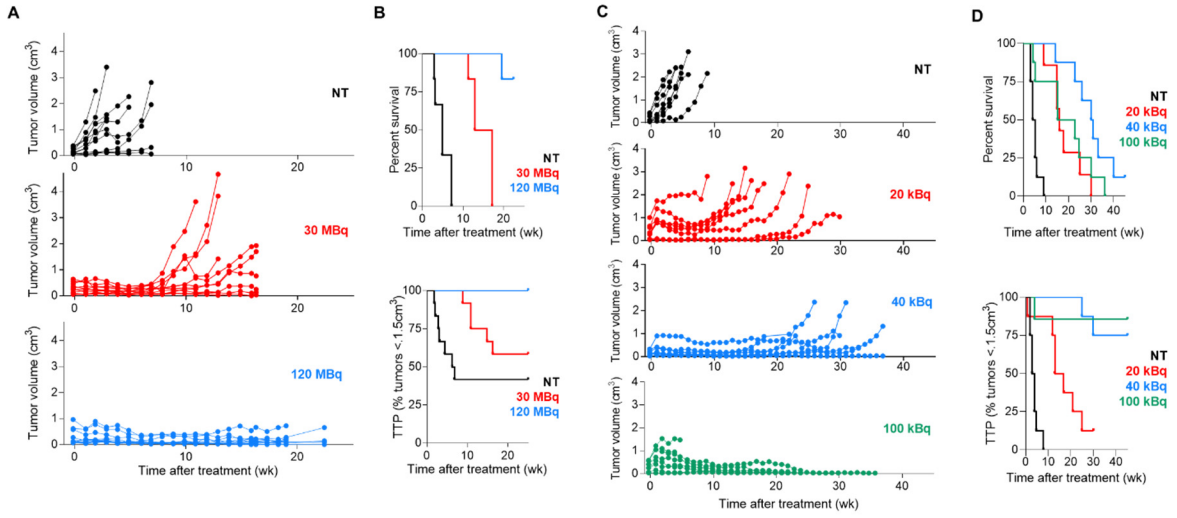


Figure 3.1 Optimizing treatment activities for $^{225}$Ac- and $^{177}$Lu-PSMA RNT. (A) Individual tumor growth curves after $^{177}$Lu-PSMA (12 tumors, 6 mice per group; NT vs. RNT, $p \leq 0.0018$ [7 wk]; 30 vs. 120 MBq, $p > 0.99$ [7 wk] and $p = 0.032$ [16 wk]). (B, top) Median survival: 4.8 wk (NT), 15 wk (30 MBq), not reached (120 MBq) (6 mice per group: all $p \leq 0.001$). (B, bottom) Time to progression: 6.6 wk (NT), not reached (30 and 120 MBq) (6 mice per group; NT vs. 30 MBq, $p = 0.153$; all other $p \leq 0.014$). (C) Individual tumor growth curves after $^{225}$Ac-PSMA RNT (8 mice per group; NT vs. RNT, $P \leq 0.027$ [6wk]; 20 vs. 40 or 100 kBq, $p < 0.023$ [15wk], 40 vs. 100 kBq, $p > 0.99$). (D, top) Median survival: 4.5wk (NT), 16 wk (20 kBq), 30 wk (40 kBq), 19 wk(100 kBq) (8 mice per group; $p < 0.0137$, except 40 vs. 100 kBq [p=0.078]; 20 vs. 100 kBq [p=0.620]). (D, bottom) Time to progression: 3.5 wk (NT), 15 wk (20 kBq), not reached (40 kBq, 100 kBq) (8 mice per group; $p \leq 0.0012$, except 40 vs. 100 kBq [p=0.679]).

Comparing the efficacy of 40 kBq of $^{225}$Ac-PSMA-617 versus 30 MBq of $^{177}$Lu-PSMA-617, we found that $^{225}$Ac-PSMA RNT resulted in significantly longer survival (p=0.0019) but not TTP (p=0.147). These treatment activities were well-tolerated and selected for use in subsequent biodistribution studies.

### 3.3.2 Biodistribution and Tumor Dosimetry of $^{177}$Lu- and $^{225}$Ac-PSMA-617

The *ex-vivo* biodistribution of $^{177}$Lu- and $^{225}$Ac-PSMA-617 in subcutaneous tumors and organs is shown in Figure 3.2. Tabulated biodistribution values for tumors and organs are available in Table 3.1 and Table 3.2. Kidney uptake at 1 h after injection was significantly greater for $^{225}$Ac vs. $^{177}$Lu (25.9 ± 3.5 and 13.3 ± 1.6 %IA/g, p<0.0005), but no statistical difference was observed at later time points. Both $^{177}$Lu- and $^{225}$Ac-PSMA-617 rapidly localize to the tumor with similar uptake of 14.4 ± 4.1 and 14.1 ± 4.9 %IA/g, respectively, at 4 hours after intravenous injection (n.s.; p=0.89). Peak tumor uptake occurs at 4 hours after injection, and by 168 h (7 days), tumor uptake is significantly greater in $^{225}$Ac-treated tumors compared to $^{177}$Lu-treated tumors (9.3 ± 1.3 vs. 6.3 ± 0.9 %IA/g, p<0.004, n=5 mice per radionuclide).

Tumor time-activity uptake curves in percent injected activity were used for curve-fitting in NUKFIT (Figure 3.2B and Figure 3.2D). NUKFIT software selected the best curve-fitting model in both cases to be in the form: $A_1 e^{-\lambda_1 t} + A_2 e^{-\lambda_{phys} t}$ , where $\lambda_1$ and $\lambda_{phys}$ represent the fitted and physical decay constant, respectively. Best fit curve parameters for $A_1$, $\lambda_1$, and $A_2$ are shown in Figure 3.2 and more details with model statistics are available in Table 3.3. The resultant cumulated activities were multiplied by

the respective dose constants, and normalized by injected activity and average tumor masses. The tumor-absorbed doses for $^{177}$Lu- and $^{225}$Ac-PSMA-617 in the subcutaneous C4-2 model were 0.00758 and 65.03 cGy/kBq, respectively, or roughly 850 times greater for $^{225}$Ac vs. $^{177}$Lu. Therefore, from this study we decided to use 35 MBq $^{177}$Lu and 40 kBq $^{225}$Ac to yield approximately equivalent tumor doses in the therapeutic efficacy studies. Previous work demonstrated that 40 kBq $^{225}$Ac-PSMA-617 is well-tolerated (*56*). For the tandem treatment arm, we chose to halve the activity of each isotope in combination (17 MBq $^{177}$Lu + 20 kBq $^{225}$Ac).

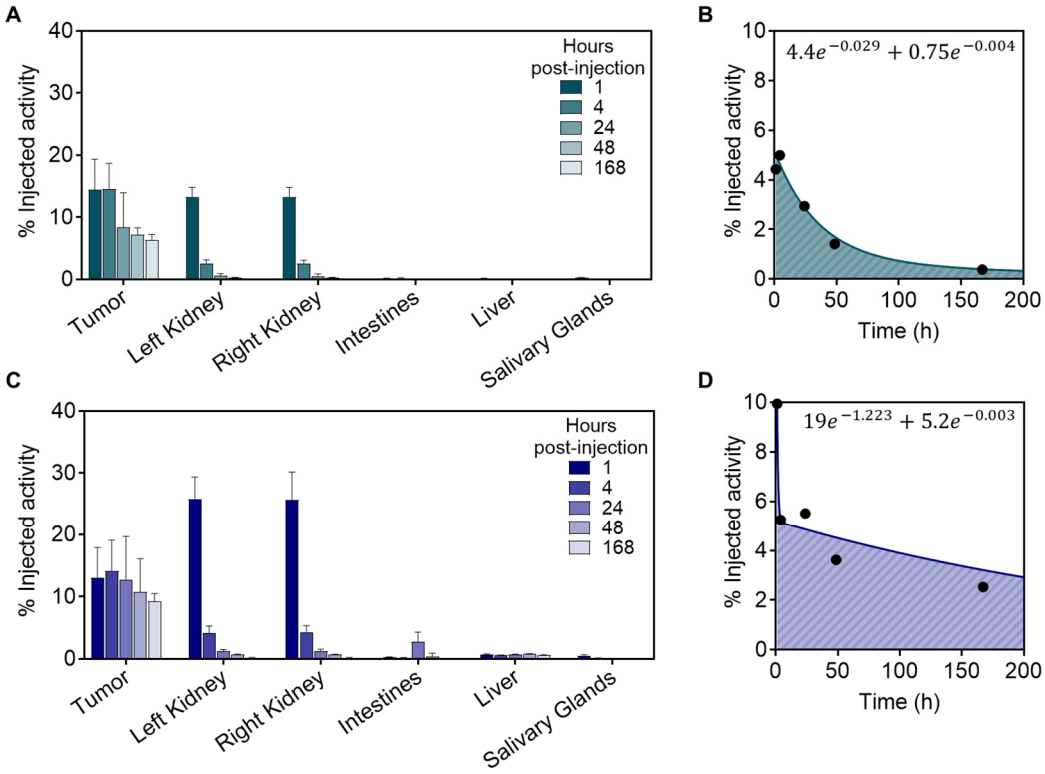


Figure 3.2. Biodistribution and tumor time-activity curves for $^{177}$Lu and $^{225}$Ac-PSMA-617. (A) Mean ± SD % injected activity per gram tissue for mice treated with 30 MBq $^{177}$Lu-PSMA-617 (n=5 mice per time point). Tabulated values and additional organs are available in Table 3.1. (B) Mean % injected activity of $^{177}$Lu-PSMA-617 uptake in tumors over time used for curve-fitting and dosimetry. Best-fit parameters are shown. (C) Mean ± SD % injected activity per gram tissue for mice treated with 40 kBq $^{225}$Ac-PSMA-617 (n=5 mice per time point). Tabulated values and additional organs are available in Table 3.2. (D) Mean % injected activity uptake of $^{225}$Ac-PSMA-617 in tumors over time used for curve-fitting and dosimetry. Best-fit parameters are shown.

Table 3.1. $^{177}$Lu-PSMA-617 biodistribution in organs and tumors (n=5 mice per time point)

| Organ | %Injected activity/gram (not decay-corrected) | | | | | | | | | |
|---|---|---|---|---|---|---|---|---|---|---|
| | 1 h | | 4 h | | 24 h | | 48 h | | 168 h | |
| | mean | SD | mean | SD | mean | SD | mean | SD | mean | SD |
| Brain | 0.025 | 0.005 | 0.016 | 0.002 | 0.013 | 0.004 | 0.008 | 0.002 | 0.002 | 0.001 |
| Tumor | 14.392 | 4.9601 | 14.536 | 4.1213 | 8.3500 | 5.6040 | 7.1320 | 1.1532 | 6.3440 | 0.8831 |
| Salivary glands (submandibular) | 0.244 | 0.039 | 0.068 | 0.019 | 0.028 | 0.008 | 0.018 | 0.005 | 0.002 | 0.005 |
| Heart | 0.260 | 0.046 | 0.026 | 0.009 | 0.008 | 0.001 | 0.005 | 0.001 | 0.001 | 0.001 |
| Lung | 0.566 | 0.068 | 0.087 | 0.022 | 0.022 | 0.002 | 0.012 | 0.001 | 0.002 | 0.001 |
| Liver | 0.156 | 0.022 | 0.074 | 0.017 | 0.040 | 0.012 | 0.030 | 0.007 | 0.010 | 0.000 |
| Left kidney | 13.25 | 1.552 | 2.566 | 0.564 | 0.550 | 0.386 | 0.230 | 0.068 | 0.048 | 0.016 |
| Right kidney | 13.20 | 1.599 | 2.544 | 0.522 | 0.538 | 0.335 | 0.232 | 0.075 | 0.050 | 0.016 |
| Spleen | 1.174 | 0.153 | 0.142 | 0.088 | 0.054 | 0.026 | 0.046 | 0.031 | 0.012 | 0.005 |
| Stomach (with contents) | 0.091 | 0.012 | 0.079 | 0.059 | 0.053 | 0.031 | 0.011 | 0.004 | 0.001 | 0.001 |
| Intestines (with contents) | 0.157 | 0.036 | 0.184 | 0.052 | 0.059 | 0.013 | 0.011 | 0.004 | 0.001 | 0.001 |
| Prostate | 1.273 | 1.783 | 0.590 | 0.840 | 0.018 | 0.026 | 0.007 | 0.007 | 0.001 | 0.001 |
| Muscle | 0.197 | 0.159 | 0.075 | 0.099 | 0.011 | 0.017 | 0.002 | 0.001 | 0.000 | 0.000 |
| Femur with BM | 0.272 | 0.175 | 0.246 | 0.193 | 0.015 | 0.004 | 0.011 | 0.002 | 0.003 | 0.001 |
| Femur no BM | 0.142 | 0.120 | 0.041 | 0.024 | 0.007 | 0.001 | 0.007 | 0.002 | 0.003 | 0.001 |
| Bone marrow | 0.086 | 0.098 | 0.176 | 0.360 | 0.008 | 0.008 | 0.014 | 0.022 | 0.000 | 0.000 |
| Blood | 0.412 | 0.065 | 0.020 | 0.007 | 0.002 | 0.005 | 0.000 | 0.000 | 0.000 | 0.000 |
| Testes | 0.372 | 0.308 | 0.057 | 0.020 | 0.027 | 0.009 | 0.011 | 0.005 | 0.003 | 0.002 |

BM: bone marrow

Table 3.2. $^{225}$Ac-PSMA-617 biodistribution in organs and tumors (n=5 mice per time point)

| Organ | %Injected activity/gram (not decay-corrected) | | | | | | | | | |
|---|---|---|---|---|---|---|---|---|---|---|
| | 1 h | | 4 h | | 24 h | | 48 h | | 168 h | |
| | mean | SD | mean | SD | mean | SD | mean | SD | mean | SD |
| Brain | 0.042 | 0.010 | 0.010 | 0.005 | 0.015 | 0.005 | 0.010 | 0.005 | 0.008 | 0.004 |
| Tumor | 12.99 | 4.901 | 14.13 | 4.939 | 12.76 | 6.924 | 10.74 | 5.326 | 9.250 | 1.270 |
| Salivary glands (submandibular) | 0.531 | 0.124 | 0.117 | 0.018 | 0.078 | 0.012 | 0.081 | 0.015 | 0.052 | 0.013 |
| Heart | 0.439 | 0.110 | 0.138 | 0.020 | 0.085 | 0.016 | 0.054 | 0.003 | 0.048 | 0.023 |
| Lung | 0.991 | 0.192 | 0.172 | 0.028 | 0.091 | 0.024 | 0.061 | 0.010 | 0.050 | 0.008 |
| Liver | 0.698 | 0.092 | 0.569 | 0.036 | 0.728 | 0.041 | 0.777 | 0.036 | 0.616 | 0.039 |
| Left kidney | 25.85 | 3.506 | 4.123 | 1.157 | 1.192 | 0.301 | 0.664 | 0.100 | 0.192 | 0.038 |
| Right kidney | 25.75 | 4.408 | 4.293 | 1.030 | 1.247 | 0.317 | 0.677 | 0.076 | 0.176 | 0.046 |
| Spleen | 1.286 | 0.386 | 0.180 | 0.055 | 0.147 | 0.050 | 0.113 | 0.076 | 0.090 | 0.061 |
| Stomach (with contents) | 0.164 | 0.013 | 0.078 | 0.061 | 3.962 | 2.254 | 0.181 | 0.104 | 0.012 | 0.002 |
| Intestines (with contents) | 0.241 | 0.063 | 0.165 | 0.034 | 2.713 | 1.572 | 0.384 | 0.511 | 0.009 | 0.001 |
| Prostate | 2.695 | 2.475 | 0.443 | 0.384 | 0.033 | 0.007 | 0.019 | 0.009 | 0.015 | 0.006 |
| Muscle | 0.268 | 0.194 | 0.035 | 0.026 | 0.020 | 0.015 | 0.016 | 0.010 | 0.016 | 0.012 |
| Femur with BM | 0.957 | 0.291 | 0.441 | 0.095 | 0.223 | 0.081 | 0.181 | 0.073 | 0.175 | 0.101 |
| Femur no BM | 0.581 | 0.299 | 0.287 | 0.121 | 0.189 | 0.072 | 0.162 | 0.032 | 0.178 | 0.096 |
| Bone marrow | 0.110 | 0.071 | 0.037 | 0.019 | 0.008 | 0.008 | 0.011 | 0.014 | 0.015 | 0.010 |
| Blood | 0.710 | 0.400 | 0.046 | 0.020 | 0.011 | 0.002 | 0.005 | 0.001 | 0.005 | 0.002 |
| Testes | 0.430 | 0.058 | 0.080 | 0.012 | 0.045 | 0.018 | 0.027 | 0.012 | 0.017 | 0.007 |

BM: bone marrow

Table 3.3. Curve-fit Parameters and Model Statistics from NUKFIT Software for Tumor % Injected Activity ($A_1 e^{-\lambda_1 t} + A_2 e^{-\lambda_{phys} t}$)

| Isotope | $A_1$ | | $\lambda_1$ | | $A_2$ | | AUC | $R^2$ | AIC |
|---|---|---|---|---|---|---|---|---|---|
| | Value | SD | Value | SD | Value | SD | | | |
| $^{177}$Lu | 4.4142 | 1.5805 | 0.0287 | 0.0292 | 0.7492 | 0.4645 | 3.061 | 0.9598 | 16.8621 |
| $^{225}$Ac | 19.0655 | 107.7149 | 1.2231 | 4.9518 | 5.2042 | 0.6690 | 18.1747 | 0.9682 | 20.4794 |

AUC: Area under curve; AIC: Aikaike information criterion

### 3.3.3 Tandem $^{177}$Lu/$^{225}$Ac Therapy

Whole body BLI radiance over time and mouse survival curves for treatment 3 weeks after inoculation are shown in Figure 3.3. Notably, disease burden of mice treated at this earlier stage of disease with $^{177}$Lu-PSMA-617 was not significantly different from untreated mice at any time point (p=0.932). However, both $^{225}$Ac-PSMA-617 as a single agent and in combination with $^{177}$Lu-PSMA-617 were associated with significant whole body tumor growth retardation (p=0.009 for tandem vs. $^{177}$Lu; p=0.0084 for $^{225}$Ac vs. $^{177}$Lu; p>0.999 for tandem vs. $^{225}$Ac measured 5 weeks after treatment). If left untreated, median survival was 8.3 weeks. When treated with 35 MBq $^{177}$Lu-PSMA-617, no significant survival benefit was observed (median survival 9.4 weeks; p=0.337). However, when treated with one of the $^{225}$Ac regimens, the median survival increased to 14.1 weeks for the tandem approach and 15.3 weeks for $^{225}$Ac-PSMA-617 alone (p<0.0001 for tandem vs. $^{177}$Lu; p<0.0001 for $^{225}$Ac vs. $^{177}$Lu; p=0.108 for $^{225}$Ac vs. tandem).

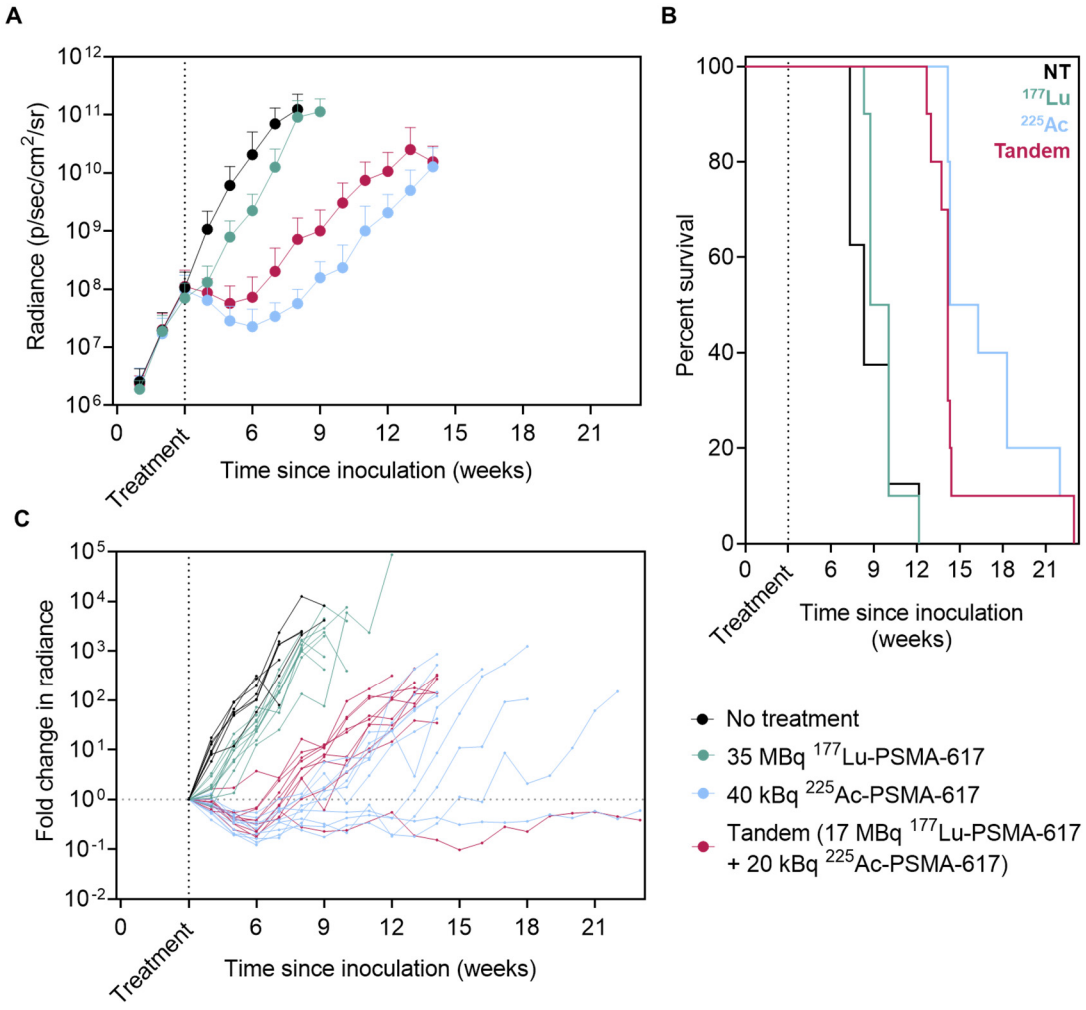


Figure 3.3 Therapeutic efficacy and survival curves for early treatment3 weeks after inoculation. (A) Mean ± SD whole body radiance over time (n=10 mice per group). Data are shown for time points with 5 or more remaining mice. (B) Median overall survival increased from 8.3 weeks to 9.4 weeks for $^{177}$Lu-PSMA-617, 14.1 weeks for tandem therapy, and 15.3 weeks for $^{225}$Ac-PSMA-617 alone (p=0.337 for NT vs. $^{177}$Lu, p<0.0001 for tandem vs. $^{177}$Lu; p<0.0001 for $^{225}$Ac vs. $^{177}$Lu; p=0.108 for $^{225}$Ac vs. tandem). (C) Individual mouse fold change in radiance over time relative to disease burden at the time of treatment. NT= no treatment.

When mice were treated at a later time point (5 weeks after inoculation), all treatment groups retarded tumor growth relative to untreated mice (Figure 3.4). However, the greatest benefits were observed with $^{225}$Ac-PSMA-617 monotherapy and tandem

approaches ($p<0.0001$ for $^{225}Ac$ vs. $^{177}Lu$; $p<0.0001$ for tandem vs. $^{177}Lu$ measured 5 weeks after treatment). Median overall survival increased from 7.9 weeks (untreated) to 10.3 weeks for $^{177}Lu$-PSMA-617, 13.2 weeks for tandem therapy, and 14.6 weeks for $^{225}Ac$-PSMA-617 alone ($p<0.0001$ for NT vs. $^{177}Lu$, $p<0.0001$ for tandem vs. $^{177}Lu$; $p<0.0001$ for $^{225}Ac$ vs. $^{177}Lu$). There were no significant differences in whole body disease burden or survival benefit conferred between $^{225}Ac$ alone vs. halving the $^{225}Ac$ activity in tandem with $^{177}Lu$ ($p=0.171$ for $^{225}Ac$ vs. tandem survival and $p>0.999$ for $^{225}Ac$ vs. tandem whole body radiance 5 weeks after treatment).

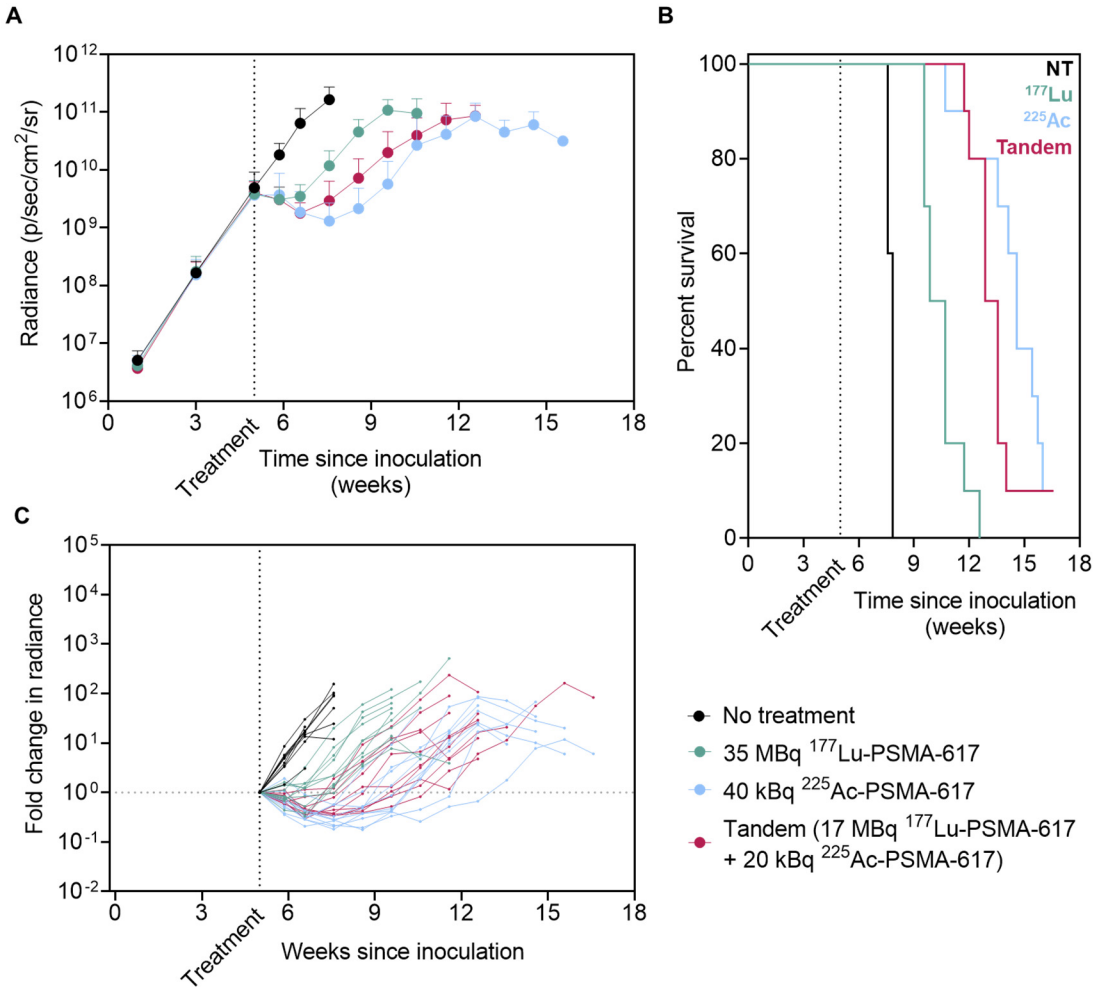


Figure 3.4 Therapeutic efficacy and survival curves for later treatment 5 weeks after inoculation. (A) Mean ± SD whole body radiance over time (n=10 mice per group). Data are shown for time points with 5 or more remaining mice. (B) Median overall survival increased from 7.9 weeks to 10.3 weeks for $^{177}$Lu-PSMA-617, 13.2 weeks for tandem therapy, and 14.6 weeks for $^{225}$Ac-PSMA-617 alone ($p<0.0001$ for NT vs. $^{177}$Lu, $p<0.0001$ for tandem vs. $^{177}$Lu; $p<0.0001$ for $^{225}$Ac vs. $^{177}$Lu; $p=0.171$ for $^{225}$Ac vs. tandem). (C) Individual mouse fold change in radiance over time relative to disease burden at the time of treatment. NT= no treatment.

## 3.4 Discussion

To our knowledge, this is the first study reporting on the efficacy of $^{177}$Lu/$^{225}$Ac-PSMA tandem isotope combinations in a mouse model of prostate cancer. In this work,

we sought to compare the treatment efficacy of the same tumor dose delivered by three different radiation mechanisms: beta particles ($^{177}$Lu), alpha particles ($^{225}$Ac), or both ($^{177}$Lu + $^{225}$Ac). To do so, we first determined efficacy and tolerability of increasing applied activities of $^{225}$Ac and $^{177}$Lu in a subcutaneous tumor model. We then found comparable injected activities to yield equivalent tumor doses by conducting a full *ex-vivo* biodistribution study using both $^{177}$Lu-PSMA-617 and $^{225}$Ac-PSMA-617. Interestingly, there was no significant difference in peak tumor uptake of $^{177}$Lu- or $^{225}$Ac -PSMA-617 4 hours after injection; however, increased tumor retention is observed at all subsequent time points for mice treated with $^{225}$Ac-PSMA-617. While normal organ biodistribution was not the primary objective of this report, all biodistribution data is available in Tables 3.1 and 3.2. In addition to the kidneys, liver, salivary glands and intestines included in this report, uptake data for the following additional organs are available: blood, heart, lungs, spleen, stomach (with contents), prostate, testes, muscle, femur (with and without bone marrow), bone marrow, and the brain.

One limitation of the mouse models used in these studies is the inability to recapitulate critical organ uptake as seen in patients (i.e. in salivary glands and kidneys). In the subcutaneous tumor model, kidney uptake was observed to be higher with $^{225}$Ac than $^{177}$Lu at 1 h after injection, however no significant difference was observed beyond the initial uptake phase. Clinically, kidney and salivary gland equivalent doses from $^{177}$Lu-PSMA-617 were reported in one study as 0.39 and 0.36-0.58 Sv/GBq, respectively (*36*). For $^{225}$Ac-PSMA-617, one dosimetry report calculated kidney and salivary gland doses to be 0.74 and 2.33 Sv/MBq, respectively (assuming a relative biologic effectiveness of 5 for $^{225}$Ac) (*96*). However, our biodistribution study revealed no significant differences in

submandibular gland uptake between $^{177}$Lu- and $^{225}$Ac-treated mice, and peak uptake was less than 0.5% at all measured time points (Figure 3.2). Given this inherent limitation in the translatability of salivary gland toxicity, it was not within the scope of this study to assess the preclinical feasibility of tandem isotope treatment to improve the toxicity profile.

Rather, we challenged a tandem isotope approach against an advanced model of widespread disease to compare dynamics of tumor control and overall survival. To more objectively compare the treatment arms against one another, we derived equivalent tumor dose-depositing injected activities for $^{177}$Lu and $^{225}$Ac and designed the tandem arm to be the combination of half each respective single agent activity. This tumor dosimetry was performed in the subcutaneous C4-2 model, the results of which were translated to the intracardiac inoculation model of C4-2 cells. While subcutaneous tumors allow for straightforward activity uptake quantification, and therefore interrogation into absorbed doses, they fail to recapitulate the metastatic state. Dosimetry was not feasible in the intracardiac inoculation model because the lesions are not easily isolated, especially in microscopic stages. Translating dosimetry findings from subcutaneous models is one approach towards standardizing the applied activity in this case where the tumor burden is distributed throughout the mouse and direct dosimetry was not possible. Furthermore, we sought to investigate the performance of tandem therapy in a model that more faithfully represents the setting in which treatment with alpha particles (alone or in combination) would actually be clinically warranted.

This is an aggressive prostate cancer model that when left untreated, the mice succumb to extensive disseminated disease warranting euthanasia by 8 weeks after

intracardiac inoculation (Figure 3C and Figure 4C). This model has previously been shown to be sensitive to treatment with $^{225}$Ac-PSMA-617 early in the disease model, but this work is the first effort at challenging at a very advanced stage (5 weeks after inoculation) (*98*). By treating at two different stages of disease, we can also seek to answer what size lesions most benefit from treatment with $^{177}$Lu or tandem approaches. At the onset of the earlier treatment time investigated (3 weeks after inoculation), the disseminated lesions are approximately ~200 μm in size, increasing to millimeter scale by 5 weeks, as previously characterized by H&E staining (*98*). When treated at 3 weeks, $^{177}$Lu-PSMA-617 as a single agent did not significantly improve tumor control or survival relative to untreated mice (Figure 3.3). However, when lesions are millimeters in size at the time of treatment, $^{177}$Lu-PSMA-617 retarded tumor growth and mice conferred a significant survival advantage (Figure 3.4). Failure of $^{177}$Lu-PSMA-617 against micron-scale lesions in the earlier treatment setting can be explained by a mismatch between the target lesion size and pathlength of the therapeutic radiation. With a mean tissue range of 600 μm (*3*), beta particles from $^{177}$Lu travel a distance that exceeds the lesion size at the time of early treatment (3 weeks). This results in a loss of specificity to the targeted lesions and attenuates tumor response, as confirmed in this study.

For treatment at both stages of disease, mice treated with $^{225}$Ac-PSMA-617 as a single agent survived the longest and yielded best tumor control (despite not reaching statistically significant differences at all time points). Given the tissue range of <0.1 mm, alpha particles from $^{225}$Ac yield dense ionizing paths with low cross-fire effect. Even when challenged with lesions on the millimeter scale, the single agent $^{225}$Ac-PSMA-617 outperformed $^{177}$Lu-PSMA-617. Interestingly, halving the $^{225}$Ac activity in tandem with

$^{177}$Lu did not significantly increase the whole body disease burden as measured 5 weeks after treatment (Figure 3.3A and Figure 3.4A). This superior therapeutic efficacy of $^{225}$Ac in the microscopic setting suggests a preference for alpha emitters alone, or possibly in combination, for treatment of microscopic or minimal residual disease. Further work is needed to understand the optimal conditions in which to scale the applied activities in tandem approaches to balance tradeoffs in efficacy and toxicity.

## 3.5 Conclusion

Treatment of a microscopic model of prostate cancer with 40 kBq $^{225}$Ac-PSMA-617 or 20 kBq $^{225}$Ac in tandem with 17 MBq $^{177}$Lu results in significantly decreased tumor growth compared with $^{177}$Lu which was ineffective as a single agent against microscopic lesions. Mice treated later (when lesions are millimeter scale in size) experience significant tumor growth retardation and survival benefit in both monotherapy and tandem regimes of $^{177}$Lu and $^{225}$Ac. However, the greatest benefits are observed with the single agent $^{225}$Ac and tandem approaches. Further work is needed to identify disease patterns and settings that most benefit from treatment with beta particles, alpha particles, or both.

# Chapter 4: Evaluation of a novel PSMA ligand with extended circulation time

A version of this chapter has been presented at the 2021 EANM Annual Meeting and is the basis for a submitted manuscript: Meyer C, Prasad V, Stuparu A, Kletting P, Glatting G, Miksch J, Solbach C, Lückerath K, Nyiranshitu L, Zhu S, Czernin J, Beer J, Slavik R, Calais J, Dahlbom M. Comparison of PSMA-TO-1 and PSMA-617 labelled with $^{68}$Ga, $^{177}$Lu and $^{225}$Ac. [Manuscript submitted].

## 4.1 Introduction

One potential strategy to increase tumor radiation doses is to extend the PSMA ligand circulation time. Reducing the blood clearance (by the kidneys and other off-target organs) can potentially lead to an increased tumor accumulation of the radiolabeled peptide. One approach is to use an Evans blue albumin-binding moiety that was shown to yield a 2-6 fold increase in the number of disintegrations in tumors using $^{177}$Lu-EB-PSMA-617 compared to $^{177}$Lu-PSMA-617 (*101*). This Evans blue modification approach has also been investigated for PRRT which was shown to increase tumor dose relative to $^{177}$Lu-DOTATATE; and, in a subsequent phase I clinical trial, improved response rates (NCT03478358) (*102,103*).

Similarly, in this study we investigate a novel PSMA-targeting ligand called PSMA-TO-1 (“Tumor-Optimized-1”) that was developed for prolonged circulation time and higher tumor uptake (Dr. H.-J. Wester, Technische Universität München, Germany). Compared with PSMA-617 and PSMA-11, PSMA-TO-1 contains an extended linker with additional napthyl groups to increase albumin and other protein binding in blood, thereby increasing

the lipophilicity. Chemical structures for these PSMA ligands are shown in Figure 4.1. Experimentally, PSMA-TO-1, also known as PSMA-71, was shown to improve internalization and exhibit greater albumin binding than both PSMA-617 and PSMA-I&T (98 vs. 74 and 78%, respectively) (*104*). Additionally, in mice bearing LNCaP tumors, biodistribution data of $^{177}$Lu-PSMA-TO-1 revealed 3 times greater tumor uptake 24 hours after injection compared with $^{177}$Lu-PSMA-I&T (14.3 ± 0.9 vs. 4. 1 ± 1.1 %IA/g) with an improved tumor-to-kidney uptake ratio (0.4 vs. 0.1, respectively) (*104*). These promising findings warranted further exploration into the performance and application of PSMA-TO-1.

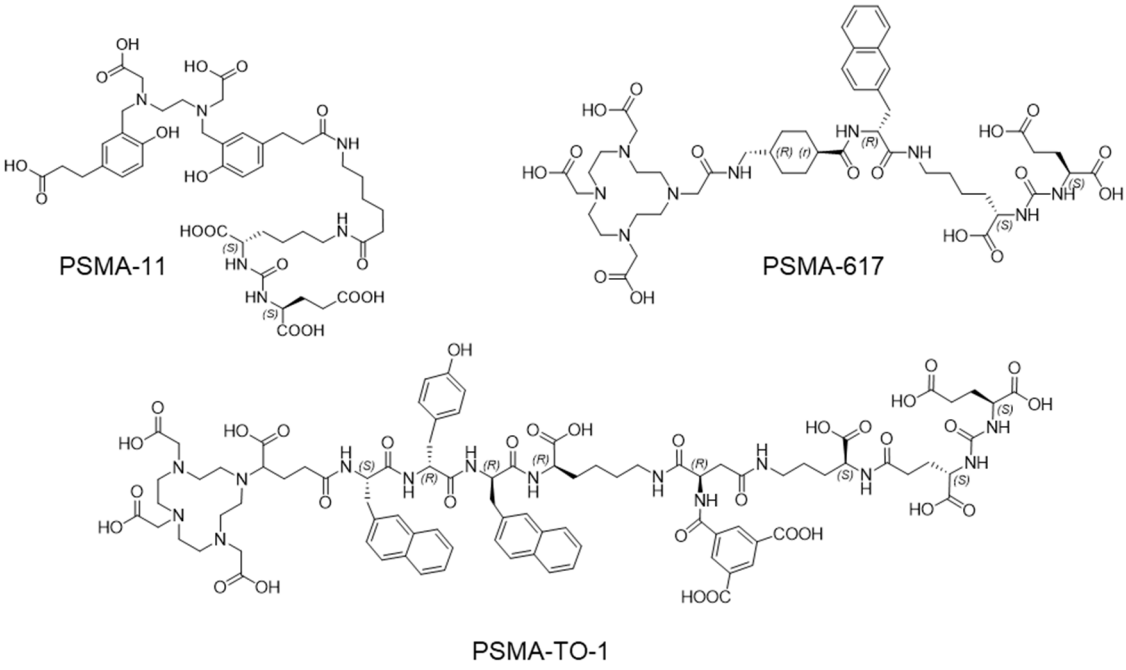


Figure 4.1 PSMA-targeting peptides. Chemical structures for PSMA-11, PSMA-617, and PSMA-TO-1 used in this study. PSMA-TO-1 contains an extended linker with additional napthyl groups.

Here we directly compared PSMA-TO-1 with the two most widely studied PSMA ligands for imaging and therapy: PSMA-11 and PSMA-617, respectively. We first determined the biodistribution of the diagnostic compounds $^{68}$Ga-PSMA-TO-1/-617/-11 in preclinical models. We then assessed the biodistribution of the therapeutic compounds $^{177}$Lu-PSMA-TO-1 and $^{177}$Lu-PSMA-617 in a subcutaneous tumor model. Finally, we conducted a murine survival study in a model of disseminated prostate cancer to compare therapeutic efficacy of $^{225}$Ac-PSMA-TO-1 and $^{225}$Ac-PSMA-617 against widespread disease.

## 4.2 Materials and Methods

### 4.2.1 Cell Culture and Animal Studies

In all studies, the C4-2 cell line was used in 6-8 weeks old NSG mice. Details regarding cell culture and animal studies are as previously described in Section 2.2.1 and Section 2.2.2.

### 4.2.2 Radiopharmaceutical Synthesis

PSMA-11 and PSMA-617 precursors were obtained from ABX advanced biochemical compounds (Radeberg, Germany). PSMA-TO-1 precursor was obtained from Dr. H.-J. Wester (Technische Universität München, Germany). Radiolabeling with $^{68}$Ga is as described in Section 2.2.4. Radiolabeling procedures for $^{177}$Lu and $^{225}$Ac are available in Section 3.2.2.

### 4.2.3 $^{68}$Ga-PSMA-TO-1/-617/-11 PET/CT Imaging in Mice

NSG mice bearing subcutaneous C4-2 tumors underwent PET/CT imaging with each of the following compounds on consecutive days: $^{68}$Ga-PSMA-11, $^{68}$Ga-PSMA-617, and $^{68}$Ga-PSMA-TO-1 in the same 3 mice. Average tumor volumes over the 3 days were 660 ± 35 mm$^3$, 190 ± 32mm$^3$, and 243 ±1.5 mm$^3$ for mouse 1, 2, and 3, respectively. PET image acquisition parameters are available in Section 2.2.4. The resulting PET/CT images were analyzed for tumor volume and percent injected activity uptake per gram using VivoQuant Imaging Software (Invicro, Boston, MA). One-way ANOVA with Bonferroni's multiple comparisons test was used to compare the tumor uptake of each ligand.

### 4.2.4 $^{177}$Lu-PSMA-TO-1 ex-vivo Biodistribution Study in Mice

NSG mice were subcutaneously inoculated into the right shoulder region with 5 million C4-2 cells in 100 µl matrigel (n=50 mice). After 3 weeks, when average tumor size was approximately 300 mm$^3$, mice were randomized based on tumor volume and treated with 30 MBq of $^{177}$Lu-PSMA-TO-1 (n=25 mice) as previously performed for PSMA-617 in Section 3.2.4. Treatment activity (30 MBq) was selected based on previous studies (*63*). Following treatment, mice were sacrificed at 5 time points (n=5 mice/time point): 1, 4, 24, 48, and 168 hours (7 days). The following organs were collected and weighed prior to gamma-counting for activity quantification with $^{177}$Lu detection energy window of 189 – 231 keV (Cobra II Auto-Gamma; Packard Instrument Co.): blood, tumor, submandibular

salivary glands, heart, lungs, liver, bilateral kidneys, spleen, stomach (with contents), intestines (with contents), prostate, testes, muscle, femur (with and without bone marrow), bone marrow, and the brain. Kidney organ doses were estimated from the measured uptake values using OLINDA/EXM version 2.2.0 (*105*). The kidney activity data were fit and integrated to yield residence times and kidney self-doses using the 25 gram mouse model. The multiple t-test method was used for biodistribution statistical comparisons and the Holm-Sidak method was applied to determine statistical significance (set to ≤ 0.05).

### 4.2.5 $^{225}$Ac-PSMA-TO-1/-617 Survival Study in Mice

Mice underwent intracardiac inoculation with 500,000 C4-2-luc cells (in 50 µl PBS) to achieve widespread microscopic visceral and bone metastases, as previously described and detailed in Chapter 2 (n=25 mice) (*98*). After 5 weeks, mice were randomized into 3 groups: treatment with $^{225}$Ac-PSMA-617 (n=10), treatment with $^{225}$Ac-PSMA-TO-1 (n=10), or untreated controls (n=5). Before treatment, whole body tumor burden was assessed by BLI (IVIS Lumina III *in vivo* imaging system, Perkin Elmer). Treatment groups comprised equal proportions of mice with higher and lower tumor burden to create groups with comparable average tumor burden. Two days prior to treatment, the mean bioluminescence radiance for non-treated, $^{225}$Ac-PSMA-617, and $^{225}$Ac-PSMA-TO-1 treated mice was $2.23x10^9 \pm 1.46x10^9$ p/sec/cm2/sr (n=5), $2.07x10^9 \pm 2.09x10^9$ (n=10), and $2.37x10^9 \pm 1.56x10^9$ (n=10), respectively (not significantly different; p>0.42 for all group comparisons). The mean radiance across groups was 2.23e09 p/sec/cm2/sr ± 1.48e08.

The treatment activity was selected as 40 kBq $^{225}$Ac for both the PSMA-TO-1 and 617 groups based on our previous studies outlined in Sections 3.2.3 and 3.3.1 (*21*). Mice were sacrificed when they exhibited severe weight loss and showed signs of deteriorating health such as hunching, dehydration, and labored breathing. The overall condition of the animals was assessed using the body conditioning score (*85*). The Log-rank (Mantel-Cox) statistical test was used for survival analysis (GraphPad Prism 8).

## 4.3 Results

### 4.3.1 $^{68}$Ga-PSMA-TO-1/-617/-11 PET/CT Imaging

All $^{68}$Ga-labeled PSMA-TO-1, PSMA-11, and PSMA-617 PET images showed high tumor accumulation 1 hour after tail vein injection (Figure 4.2A). Tracer clearance was predominantly via urinary excretion. We observed greatest tumor uptake (%IA/g) for PSMA-617, followed by PSMA-TO-1 and PSMA-11 in all three mice (Figure 4.2A and 4.2B). Mean tumor uptake for PSMA-TO-1, PSMA-11, and PSMA-617 was 11.27, 8.92 and 15.46 %IA/g, respectively. The difference in mean tumor uptake between ligands was not statistically significant ($p>0.06$ for all group comparisons).

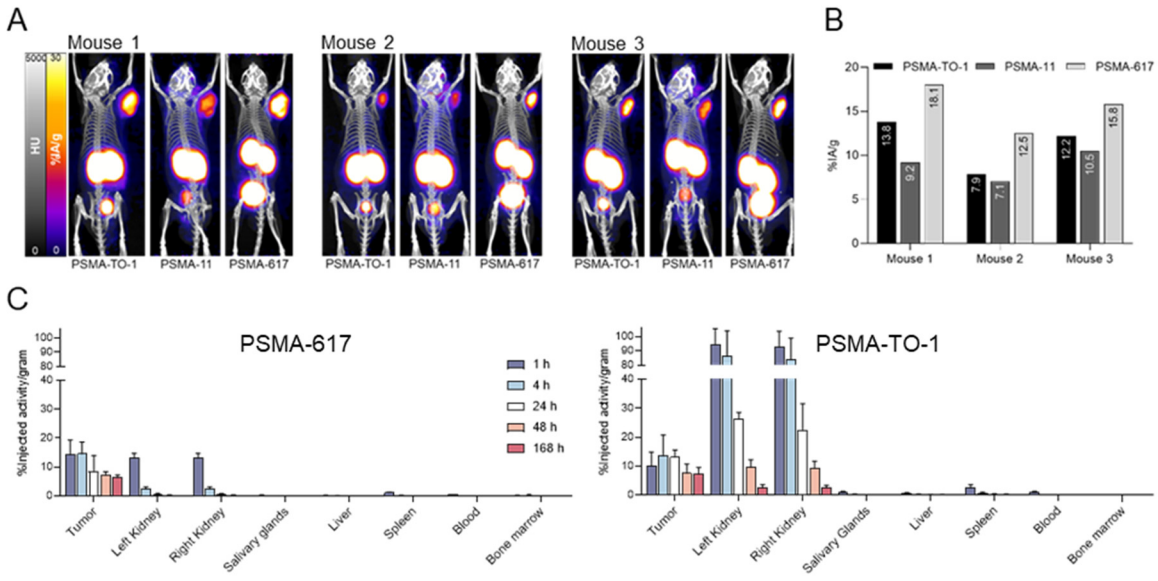


Figure 4.2 $^{68}$Ga-PSMA PET and $^{177}$Lu-PSMA biodistribution in mice. (A) Mice bearing subcutaneous C4-2 tumors were imaged 1 h after administration of $^{68}$Ga-PSMA-TO-1/-11/-617 on consecutive days in the same 3 mice. (B) Corresponding tumor percent injected activity per gram (%IA/g). Mean tumor uptake for PSMA-TO-1, PSMA-11, and PSMA-617 was 11.27, 8.92 and 15.46 %IA/g, respectively (not statistically different; $p>0.06$). (C) Non-decay-corrected tumor and organ %IA/g in mice treated with 30 MBq $^{177}$Lu-PSMA-617 (left) or 30 MBq $^{177}$Lu-PSMA-TO-1 (right) (n=5 mice/time point per ligand; bar graphs show mean ± SD). All other organs not shown measured %IA/g<0.4% at their peak and uptake values for all organs are available in Tables 3.1 and 4.1.

### 4.3.2 $^{177}$Lu-PSMA-TO-1 ex-vivo Biodistribution Study

Similar to $^{177}$Lu-PSMA-617, ex-vivo counts of $^{177}$Lu-PSMA-TO-1 revealed predominant uptake in the subcutaneous tumors and kidneys (Figure 4.2C). Consistent with the $^{68}$Ga-PSMA-TO-1/-617 PET imaging findings, tumor uptake at 1 hour post-administration tended to be higher for $^{177}$Lu-PSMA-617 than $^{177}$Lu-PSMA-TO-1, though it did not reach statistical significance (14.4 vs. 10.2 %IA/g; $p=0.207$). Tabulated uptake values for $^{177}$Lu-PSMA-617 and $^{177}$Lu-PSMA-TO-1 are available in Table 3.1 and Table 4.1, respectively. At all subsequent measurement time points, the absolute tumor uptake

tended to be higher for PSMA-TO-1 than PSMA-617 ($p>0.13$ for all time points). However, kidney uptake was also higher (24 %IA/g 24 hours after administration, compared with 0.54 %IA/g using PSMA-617; $p=0.0001$, $n=5$ mice [10 kidneys] per time point per compound). Kidney TIACs for $^{177}$Lu-PSMA-617 and $^{177}$Lu-PSMA-TO-1 were 2.00E-01 and 5.34E00 MBq-h/MBq, respectively. This translates to a 26 times greater dose in the kidneys for PSMA-TO-1 compared with PSMA-617 (5.41E01 vs. 1.44E03 mSv/MBq; or, 43 Sv vs. 1.6 Sv for an injected activity of 30 MBq).

Table 4.1 $^{177}$Lu-PSMA-TO-1 biodistribution in organs and tumors (n=5 mice per time point)

| Organ | %Injected activity/gram (not decay-corrected) | | | | | | | | | |
|---|---|---|---|---|---|---|---|---|---|---|
| | 1 h | | 4 h | | 24 h | | 48 h | | 168 h | |
| | mean | SD | mean | SD | mean | SD | mean | SD | mean | SD |
| Brain | 0.042 | 0.012 | 0.014 | 0.004 | 0.009 | 0.001 | 0.005 | 0.001 | 0.003 | 0.001 |
| Tumor | 10.23 | 4.631 | 13.47 | 7.315 | 13.08 | 2.479 | 7.501 | 3.162 | 7.423 | 2.092 |
| Salivary glands (submandibular) | 1.089 | 0.262 | 0.230 | 0.087 | 0.130 | 0.012 | 0.098 | 0.007 | 0.051 | 0.009 |
| Heart | 0.777 | 0.332 | 0.145 | 0.044 | 0.072 | 0.006 | 0.059 | 0.008 | 0.030 | 0.006 |
| Lung | 1.752 | 0.363 | 0.313 | 0.086 | 0.089 | 0.008 | 0.068 | 0.013 | 0.018 | 0.010 |
| Liver | 0.680 | 0.145 | 0.254 | 0.031 | 0.234 | 0.019 | 0.190 | 0.024 | 0.093 | 0.06 |
| Left kidney | 94.70 | 10.75 | 86.70 | 17.42 | 26.31 | 2.211 | 9.760 | 2.435 | 2.689 | 0.825 |
| Right kidney | 92.74 | 10.87 | 84.12 | 14.78 | 22.47 | 9.095 | 9.448 | 2.286 | 2.526 | 0.855 |
| Spleen | 2.662 | 0.851 | 0.559 | 0.451 | 0.342 | 0.041 | 0.230 | 0.099 | 0.059 | 0.053 |
| Stomach (with contents) | 0.739 | 0.461 | 0.141 | 0.192 | 0.563 | 0.543 | 0.056 | 0.033 | 0.014 | 0.013 |
| Intestines (with contents) | 0.266 | 0.111 | 0.112 | 0.032 | 0.290 | 0.220 | 0.032 | 0.008 | 0.055 | 0.092 |
| Prostate | 0.954 | 0.112 | 0.252 | 0.247 | 0.042 | 0.012 | 0.019 | 0.003 | 0.011 | 0.005 |
| Muscle | 0.328 | 0.081 | 0.056 | 0.012 | 0.019 | 0.003 | 0.013 | 0.002 | 0.007 | 0.006 |
| Femur with BM | 1.055 | 0.510 | 0.200 | 0.068 | 0.120 | 0.024 | 0.090 | 0.018 | 0.035 | 0.025 |
| Femur no BM | 0.614 | 0.282 | 0.154 | 0.030 | 0.097 | 0.047 | 0.045 | 0.031 | 0.030 | 0.006 |
| Bone marrow | 0.021 | 0.006 | 0.003 | 0.001 | 0.001 | 0.000 | 0.001 | 0.001 | 0.001 | 0.000 |
| Blood | 1.030 | 0.305 | 0.084 | 0.038 | 0.012 | 0.004 | 0.004 | 0.003 | 0.000 | 0.000 |
| Testes | 0.721 | 0.091 | 0.227 | 0.035 | 0.111 | 0.042 | 0.050 | 0.042 | 0.044 | 0.009 |

BM: bone marrow

### 4.3.3 $^{225}$Ac-PSMA-TO-1/-617 Survival Study

$^{225}$Ac-PSMA-617 and $^{225}$Ac-PSMA-TO-1 both significantly prolonged median overall survival relative to untreated mice (7.7 vs. 14.5 and 7.7 vs. 17.8 weeks; p<0.0001). The survival benefit conferred by mice treated with $^{225}$Ac-PSMA-TO-1 was statistically significant compared to treatment with $^{225}$Ac-PSMA-617 (p=0.0002) (Figure 4.3).

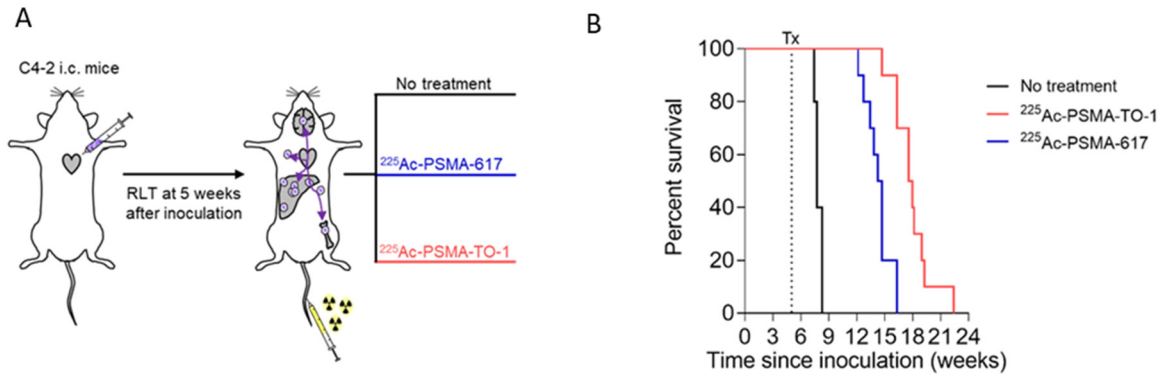


Figure 4.3 $^{225}$Ac-PSMA-617 and $^{225}$Ac-PSMA-TO-1 mouse overall survival. (A) Experimental design. (B) Median survival increased from 7.7 weeks (no treatment) to 14.5 weeks for $^{225}$Ac-PSMA-617 and 17.8 weeks for $^{225}$Ac-PSMA-TO-1 treated mice (n=10 mice/treatment group and 5 mice for controls: p<0.0001 for NT vs. PSMA-617 or PSMA-TO-1, and p=0.0002 for PSMA-617 vs. PSMA-TO1). RLT = radioligand therapy, i.c. = intracardiac.

## 4.4 Discussion

### 4.4.1 Preclinical Experiments

In this work we first examined the preclinical biodistribution of 3 PSMA-targeting compounds in tumor-bearing mice. We observed higher tumor uptake using PSMA-TO-1 compared with PSMA-617 after the first hour following injection. However, 24 hours after administration, murine kidney uptake was 44 times higher using PSMA-TO-1 than PSMA-

617 (24 vs. 0.54 %IA/g, respectively). This translates to a 26-fold greater kidney dose in mice. Nevertheless, the preclinical survival study indicated that mice treated with $^{225}$Ac-PSMA-TO-1 conferred a significant survival benefit compared to those treated with $^{225}$Ac-PSMA-617 (median overall survival 17.8 vs. 14.5 weeks; p=0.0002). However, long-term nephrotoxic effects could not be studied since the time for histologically measurable parenchymal damage can be greater than 6 months in murine models (*106,107*) and euthanasia was required within 7-18 weeks of treatment in all mice.

Future work may include preclinical approaches to quantify acute kidney damage with molecular or pathological biomarkers as predictors for long-term injury. One study by Pellegrini et al. identified γ-H2AX positive nuclei in the renal cortex, a marker for DNA strand breaks, as a possible indicator for long-term radiation-induced kidney damage (*107*). However, meaningful translation of preclinical observations related to renal damage are confounded by the relative increased radio-resistance of murine kidneys compared to humans (*108,109*).

### 4.4.2 Clinical Dosimetry Collaboration

In addition to our preclinical experiments, this overall study included early evaluation of PSMA-TO-1 in patients. We have collaborated with the University of Ulm, Germany to evaluate the dosimetry of $^{177}$Lu-PSMA-TO-1 in mCRPC patients. All patients had end-stage progressive mCRPC disease after all conventional therapies had failed and were referred by their treating uro-oncologist for $^{177}$Lu-PSMA therapy under compassionate use in compliance with the German Medicinal Products Act, AMG §13

(2b). Three patients gave written informed consent following national regulations, the updated Declaration of Helsinki, and Good Clinical Practice. All three patients were injected with 500 MBq of $^{177}$Lu-PSMA-TO-1; a sub-therapeutic activity for dosimetry calculation purposes only. Dosimetry estimates were based on planar and SPECT image acquisitions after activity administration. No subsequent therapy with $^{177}$Lu-PSMA-TO-1 was performed.

Kidney, salivary gland, bone marrow and tumor doses for $^{177}$Lu-PSMA-TO-1 in all three patients are available in Table 4.2. In patient #03, the only patient for whom a dosimetry comparison between PSMA-TO-1 and PSMA-617 could be completed, the therapeutic index (mean tumor dose/critical organ dose) of $^{177}$Lu-PSMA-617/$^{177}$Lu-PSMA-TO-1 for the kidney, bone marrow and salivary gland was 1.6/0.6, 28.8/18.0, and 0.9/0.8, respectively (Figure 4.4). Due to the higher uptake in critical organs, no subsequent radionuclide therapy with $^{177}$Lu-PSMA-TO-1 was done.

Table 4.2. Clinical dosimetry results in three mCRPC patients

| **Organ** | **$^{177}$Lu-PSMA-TO-1 Dose (Gy/GBq)** | | | **$^{177}$Lu-PSMA-617 Dose (Gy/GBq)** |
|---|---|---|---|---|
| | **Patient #01** | **Patient #02** | **Patient #03** | **Patient #03** |
| Kidneys | 2.5 | 2.4 | 3.0 | 0.6 |
| Salivary Gland | 1.0 | 2.5 | 2.3 | 1.1 |
| Bone Marrow | 0.14 | 0.11 | 0.10 | 0.033 |
| Tumor 1 | 0.40 | 4.4 | 2.2 | 1.10 |
| Tumor 2 | 0.44 | 4.5 | 1.4 | 0.80 |

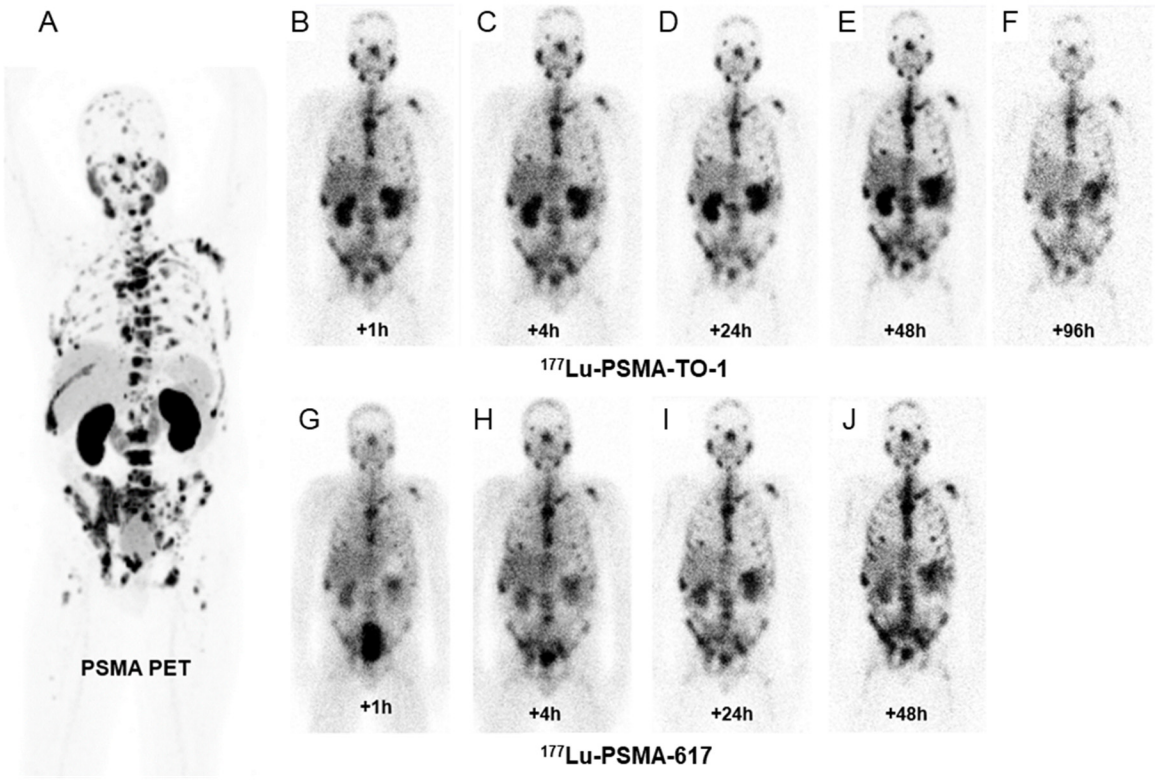


Figure 4.4 $^{177}$Lu-PSMA-TO-1 imaging in Patient #03. (A) PSMA PET 3D maximum intensity projection (MIP) and $^{177}$Lu-PSMA-TO-1 gamma planar imaging anterior views at +1h (B), +4h (C), +24h (D), +48h (E), +96h (F). $^{177}$Lu-PSMA-617 gamma planar imaging anterior views at +1h (G), +4h (H), +24h (I), +48h (J). Gamma images are normalized to liver uptake.

In addition, Patient #01 underwent both $^{68}$Ga-PSMA-TO-1 and $^{68}$Ga-PSMA-11 PET/CT imaging. Blood pool activity and kidney uptake were higher with PSMA-TO-1 than with PSMA-11 (mean standardized uptake value [SUVmean] of 4.0 vs 1.0 and 30 vs. 14, respectively). Tracer uptake in liver metastases was higher with $^{68}$Ga-PSMA-TO-1 compared to $^{68}$Ga-PSMA-11: SUVmean 6.0 vs. 4.0. At 120 minutes, $^{68}$Ga-PSMA-TO-1 uptake in metastases increased (SUVmean 8.0, +33%), whereas blood pool uptake remained constant (Figure 4.5 and Table 4.3).

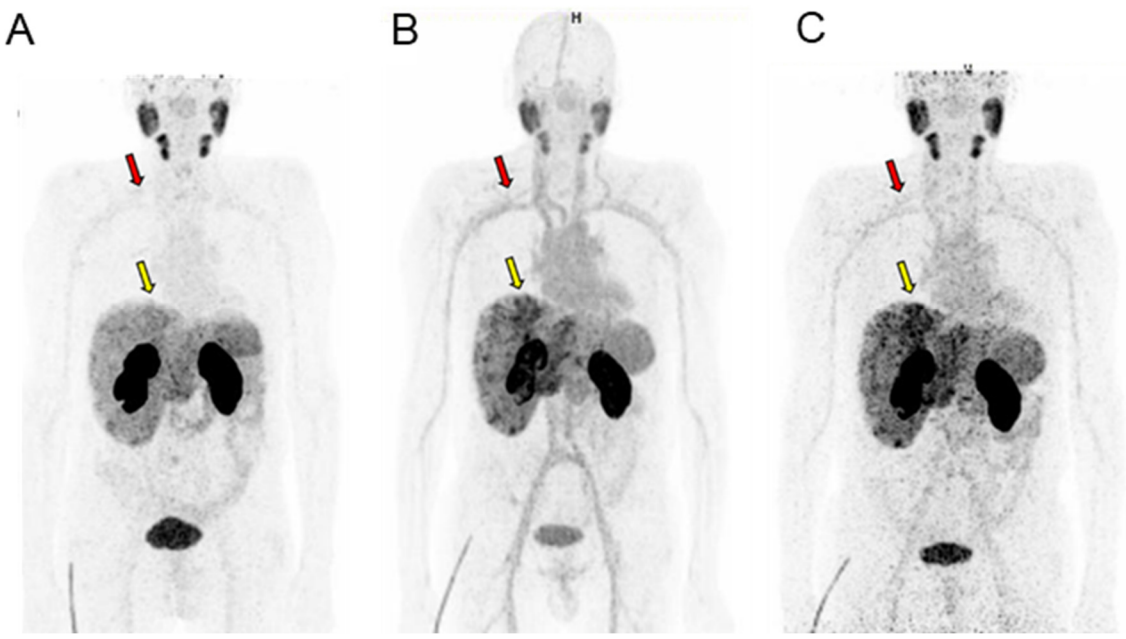


Figure 4.5 PSMA PET images in patient #01 (A) $^{68}$Ga-PSMA-11 PET MIP at +60 minutes. B) $^{68}$Ga-PSMA-TO-1 PET MIP at +60 minutes. C) $^{68}$Ga-PSMA-TO-1 PET MIP at +120 minutes. Blood pool activity was higher with $^{68}$Ga-PSMA-TO-1 in comparison to $^{68}$Ga-PSMA-11 (red arrows). Tumor uptake in liver metastases was slightly higher with $^{68}$Ga-PSMA-TO-1 in comparison to $^{68}$Ga-PSMA-11 and increased at +120 minutes (yellow arrows, SUVmean 6.0 to 8.0, +33%). SUVmean values are available in Table 4.3.

Table 4.3. $^{68}$Ga-PSMA-TO-1 and $^{68}$Ga-PSMA-11 PET/CT SUVs in patient #01

| Organ | SUVmean $^{68}$Ga-PSMA-TO-1 60 minutes | SUVmean $^{68}$Ga-PSMA-11 60 minutes | SUVmean $^{68}$Ga-PSMA-TO-1 120 minutes |
|---|---|---|---|
| Blood pool | 4 | 1 | 4 |
| Spleen | 6 | 6 | 6 |
| Kidneys | 30 | 14 | 24 |
| Salivary glands | 6 | 9 | 10 |
| Liver metastasis | 6 | 4 | 8 |

Clinically, the kidney dose was 6-8 times higher using $^{177}$Lu-PSMA-TO-1 compared with $^{177}$Lu-PSMA-617 (2.4-3.0 vs. 0.39 Gy/GBq, based on $^{177}$Lu-PSMA-617 dose

estimates from Violet et al.) (*36*). The kidneys are a primary dose-limiting organ in PSMA-targeted RNT, with commonly used maximum tolerated dose thresholds ranging from 18 to 28 Gy (derived from EBRT studies) (*110,111*). However the low dose rate radiation delivered by RNT differs from the high dose rate of EBRT, and biologically effective doses up to 40 Gy with low dose rate RNT may be well-tolerated (*111*). This may in part be explained by the relatively short survival of patients who may not live to experience renal toxicity. Similarly, our preclinical biodistribution study revealed increased kidney uptake and dose for PSMA-TO-1 compared with PSMA-617.

Since PSMA-TO-1 is a longer-circulating peptide, higher bone marrow doses were expected. Indeed, dosimetry data of Patient #03 revealed a 3-fold higher bone marrow dose with PSMA-TO-1 compared to PSMA-617 (Table 4.2). Comparing the bone marrow dose in these three patients with a larger PSMA-617 cohort (*34*), the bone marrow dose is 8-10 fold higher for PSMA-TO-1 than with PSMA-617. While this higher dose could pose more risk for hematotoxicity, greater bone marrow exposure may be efficacious in treating patients with bone marrow involvement. Overall, the higher uptake in normal organs in both preclinical and clinical settings necessitates that this tracer undergo further preclinical testing and optimization.

## 4.5 Conclusion

Overall, higher tumor uptake was observed with PSMA-TO-1 compared with PSMA-617 in the later phase of biodistribution. Preclinical studies demonstrated a significant survival benefit with $^{225}$Ac-PSMA-TO-1 over $^{225}$Ac-PSMA-617. However, in a

related clinical study, $^{177}$Lu-PSMA-TO-1 also led to higher radiation doses to kidneys, salivary glands, and bone marrow. Before further clinical use, preclinical optimization of PSMA-TO-1 is required.

# Chapter 5: Radiation dosimetry of a new pan-cancer imaging agent

A version of this chapter has been published: Meyer C, Dahlbom M, Lindner T, Vauclin S, Mona C, Slavik R, Czernin J, Haberkorn U, Calais J. Radiation dosimetry and biodistribution of $^{68}$Ga-FAPI-46 PET imaging in cancer patients. J Nucl Med. 2020; 26:2946-2955.

## 5.1 Introduction

While most efforts towards radionuclide therapy for prostate cancer have been focused on PSMA, targeting the stroma in the tumor microenvironment has become an attractive goal for both diagnostic imaging and therapy (*112-114*). Cancer-associated fibroblasts (CAFs) are the predominant component of the stroma surrounding epithelial cancer cells, and they can comprise up to 90% of the total tumor mass (*115-118*). These stromal cells selectively produce fibroblast activation protein (FAP), a protease which is scarcely expressed within the stroma of healthy tissues (*112,115,116*). FAP-positive CAFs are reported to promote and enhance pro-tumorigenic characteristics such as angiogenesis, neoplastic progression, metastatic invasion and migration (*115,119-125*). FAP expression is high in CAFs, but low in normal adult tissues, except for sites of active tissue damage, remodeling and inflammation (*115*).

The specificity of FAP for the CAFs in the tumor microenvironment provided the motivation to develop FAP-specific small molecule inhibitors. Several FAP-inhibitors (FAPI) that can be labeled with positron emitters have since been developed (*126-128*). Most recently, FAPI-04 labeled with $^{68}$Ga provided PET images with high tumor-to-

background ratios (TBRs) in patients across a wide array of cancers, suggesting high potential for FAP-targeted diagnostics, and possibly RNT (*128-131*). Because the stroma can represent up to 90% of the total tumor mass, stroma-targeted PET imaging may be a sensitive diagnostic companion for tumor detection in some cancers, particularly in cancers with poor FDG visualization (*127,129,132,133*). In the context of stroma-targeted radionuclide therapy, breaking the tumor stroma barrier may also increase tumor cells accessibility for pharmacologic, immunologic or cell-based therapies (10-12). Additionally, delivery of ionizing radiation to the cancer cells may also be possible by crossfire effect.

In an effort to increase FAPI tumor uptake and retention for therapeutic applications, related FAPI-04 derivatives were previously developed and assessed preclinically as well as in cancer patients (*128*). From these studies, FAPI-46 emerged as the most promising tracer for therapeutic clinical application due to its high tumor uptake and retention, and lower uptake in normal organs compared with FAPI-04. As a required step for further translation and approval by regulatory agencies, the primary objective of this study was to provide the radiation dosimetry analysis in cancer patients who underwent $^{68}$Ga-FAPI-46 PET imaging. The secondary aim was to describe the organ biodistribution, SUV metrics, and temporal changes in TBR values (Tumor SUVmax / Organ SUVmean).

## 5.2 Materials and Methods

### 5.2.1 Study Design and Patients

This was a retrospective study of radiation dosimetry and biodistribution of a novel PET imaging probe done in collaboration with the Heidelberg University Hospital in Germany. All patient imaging was performed at Heidelberg University and the imaging data was shared with our group at UCLA for dosimetry and biodistribution analysis. Six patients (4 males, 2 females; age 56 – 81 years) with different cancer types were included. All six patients were referred for an unmet diagnostic challenge that could not be solved sufficiently with standard diagnostic imaging. A summary of patient characteristics is presented in Table 5.1. All patients gave written informed consent to receive FAPI PET/CT. Following the regulations of the German Pharmaceuticals Act §13(2b), indication and labeling of the FAPI-tracers were conducted under the direct responsibility of the applying physician. The data were analyzed retrospectively with approval of the local ethics committee (No. S016/2018).

Table 5.1 $^{68}$Ga-FAPI-46 Patient characteristics

| Patient no. | Sex | Age | Diagnosis | Injected activity (MBq) |
|---|---|---|---|---|
| 1 | F | 63 | Cholangiocellular carcinoma | 246 |
| 2 | M | 81 | Pancreatic cancer with peritonitis carcinomatosa | 240 |
| 3 | F | 78 | Breast cancer | 234 |
| 4 | M | 56 | Oropharynx carcinoma | 239 |
| 5 | M | 78 | Head and neck cancer | 214 |
| 6 | M | 62 | Gastric cancer | 243 |

### 5.2.2 PET/CT Image Acquisition

Based on previous dosimetry estimates of related FAP inhibitors with an effective whole body dose of 1.6 mSv/100 MBq, the maximum injected activity was 250 MBq (*132*). The radiotracer synthesis was conducted as previously published (*126-128*). Each patient underwent PET/CT imaging scans at three time points after radiotracer injection: 10 minutes, 1 hour, and 3 hours. No bladder voiding model was used and thereby the calculated bladder dose will be the maximum dose assuming no voiding. All imaging was performed on a Siemens Biograph mCT Flow scanner. Following non-contrast-enhanced low-dose CT (130keV, 30mAs, CareDose; reconstructed with a soft tissue kernel to a slice thickness of 5mm, increment of 3-4 mm), PET images were acquired in 3-D mode (matrix 200 × 200) using FlowMotion$^{TM}$ (Siemens) with 0.7 cm/min continuous bed motion. The emission data were corrected for randoms, scatter and decay. Reconstruction was performed with an ordered subset expectation maximization (OSEM) algorithm with 2 iterations / 21 subsets and Gauss-filtered to a transaxial resolution of 5 mm at full-width at half-maximum; Attenuation correction was performed using the non-enhanced low dose CT data.

### 5.2.3 Radiation Dosimetry

Mean absorbed radiation doses were estimated using the source and target organ framework outlined by the MIRD Committee (*134,135*). Organ delineation and activity accumulation at each imaging time point was calculated using PLANET Dose internal dosimetry software (DOSIsoft SA, Cachan, France). Time-activity curve fitting and

subsequent dose calculation was performed using OLINDA/EXM v.1.1. The source organs consisted of the kidney parenchyma, urinary bladder, liver, heart contents, spleen, bone marrow, uterus, as well as body remainder. Source organs were chosen based on highest tracer uptake and previously published work (*132*).

Source organ volumes of interest (VOIs) were contoured manually at the first time point and propagated to later time point scans based on automatic deformable registration between each scan. Propagated organ volumes were then manually adjusted when necessary. Organ volume differences that arose due to elastic propagation between time points were accounted for by calculating the mean volume for organ mass input for dose calculation in OLINDA/EXM. Kidney volumes included left and right renal parenchyma, excluding the urinary activity in renal calyces, as shown in Figure 5.1. The urinary activity (Figure 5.1B) was delineated using SUV thresholding and subsequently subtracted from the entire kidney volume to yield only kidney parenchyma. Activity in the bone marrow was determined by contouring two lumbar vertebrae and scaling based on the proportion of total body bone marrow mass, with each vertebra assumed to contain 2.5% (*136*).

In all cases, tumor lesion activity was excluded from normal organ source volumes by Boolean subtraction operations and incorporated in the body remainder term. Tumors were contoured using patient-specific SUV thresholding with manual adjustment (SUV threshold ranged from 2.5-3.5). The body remainder volume was determined by subtracting all source organs from a whole-body contour.

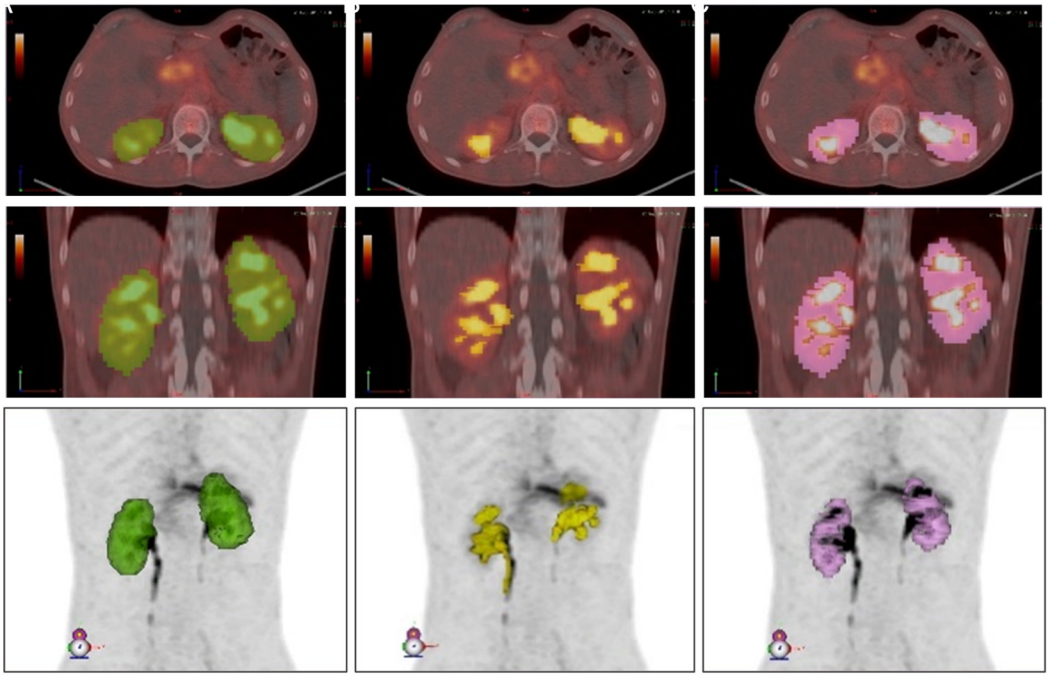

Figure 5.1 Delineated volumes used for determination of renal cortex volume. (A) The entire kidney volume from which the urine including in renal calyces is subtracted (B) to yield to the renal cortex volume (C). Images are shown for Patient 6 and are representative for the method applied for all patients. All volumes are shown in axial (top row), coronal (middle row), and maximum intensity projection (MIP) views (bottom row).

Following tumor and organ contouring, the non-decay-corrected percent injected activity accumulated in the organs at each time point per patient was then used as input for OLINDA/EXM v.1.1 software. Patient-specific masses were used for the liver, kidneys, spleen, uterus, and total body. The organ and total body/remainder activity kinetic data were then fitted with a monoexponential decay function using OLINDA/EXM v.1.1. Representative percent injected activity curves for various source organs for one patient are shown in Figure 5.2. The functions are integrated to obtain time-integrated activity coefficients and S-values are applied according to MIRD methodology from standard adult phantoms to yield absorbed and effective radiation doses. Radiation weighting

factors from ICRP 60 were applied for calculation of effective doses (*137*). The calculated doses based on individual patient inputs were then reported as means ± SD to more accurately represent the general population risk associated with this imaging scan.

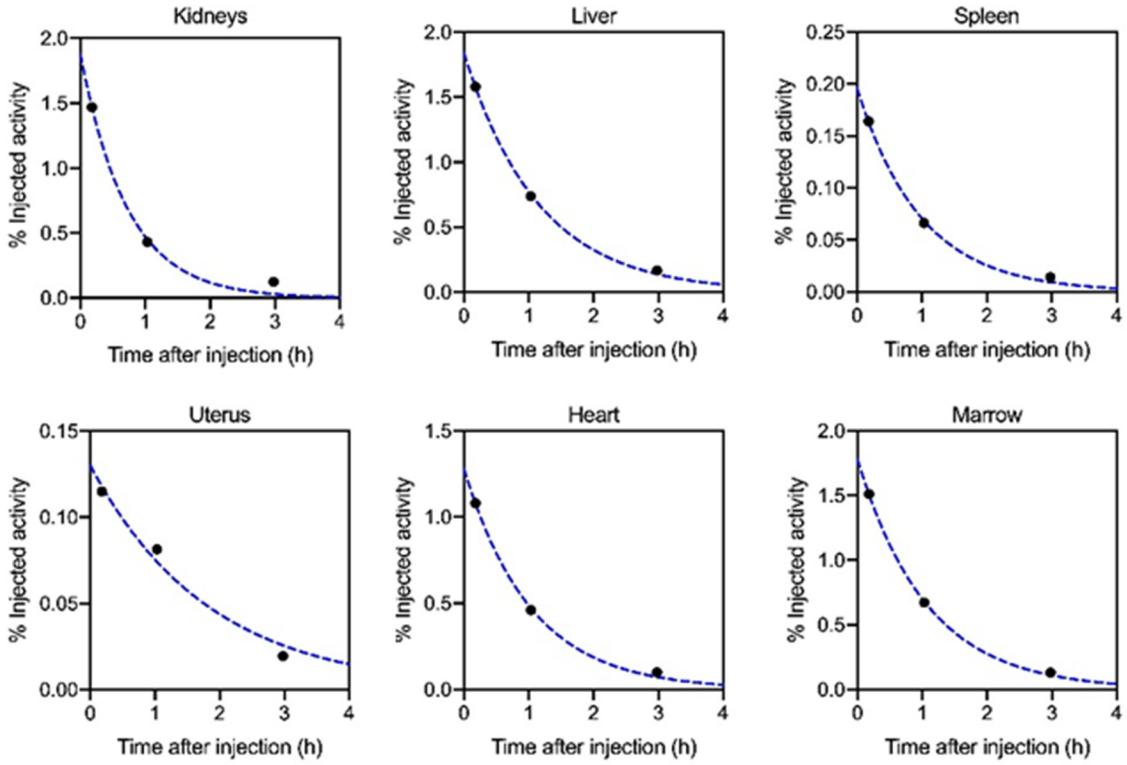


Figure 5.2 Percent injected activity curves for Patient 3 are shown for various source organs. The dotted line is the monoexponential function fit to the data.

### 5.2.4 Biodistribution

In addition to the contoured tumor and source organ volumes drawn for dosimetry, spherical volumes in the gluteal muscle (range 7-20 mL) and blood pool in the ascending aorta (range 4-5 mL) were created and automatically propagated to later time points for biodistribution analysis. Mean and maximum SUV were generated for all previously

contoured organs and spherical muscle and blood VOIs to compute TBRs (Tumor SUVmax / Organ SUVmean).

## 5.3 Results

### 5.3.1 PET/CT Imaging

The injected activity of $^{68}$Ga-FAPI-46 ranged from 214-246 MBq (5.8 – 6.6 mCi) (Table 5.1). Images were acquired at 12 ± 2.5 minutes, 1.2 ± 0.3 hours, and 3.3 ± 0.3 hours after intravenous administration of $^{68}$Ga-FAPI-46. The tracer injection was well-tolerated without any side effects in all six patients. No adverse events were observed during the three hours following injection. Maximum intensity projections (MIPs) and organ volumes used for activity quantification are shown for Patient 3 (female) and Patient 5 (male) in Figures 5.3 and 5.4, respectively.

### 5.3.2 Radiation Dosimetry

The monoexponential curve fitting parameters and time-integrated activity coefficients (TIACs), also known as residence times, for each source organ are summarized in Table 5.2. The pooled patient dosimetry reports from OLINDA/EXM v.1.1 are shown in Table 5.3.

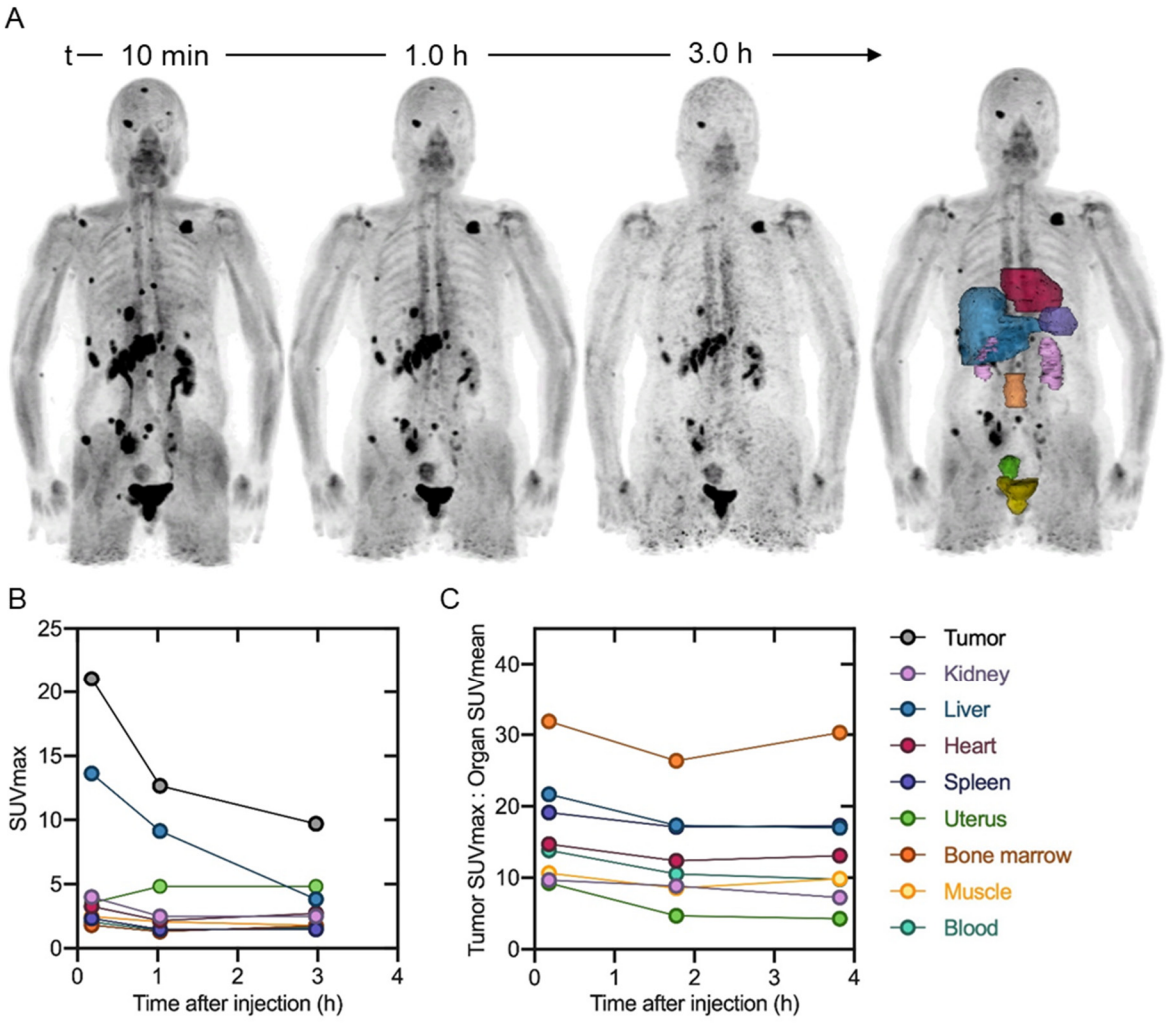


Figure 5.3 Patient 3 (Female) biodistribution. (A) $^{68}$Ga-FAPI-46 MIPs and delineated organs for dose calculations, (B) SUVmax and (C) TBR at three timepoints following tracer injection. SUVmax and TBR for the bladder are excluded from the plot.

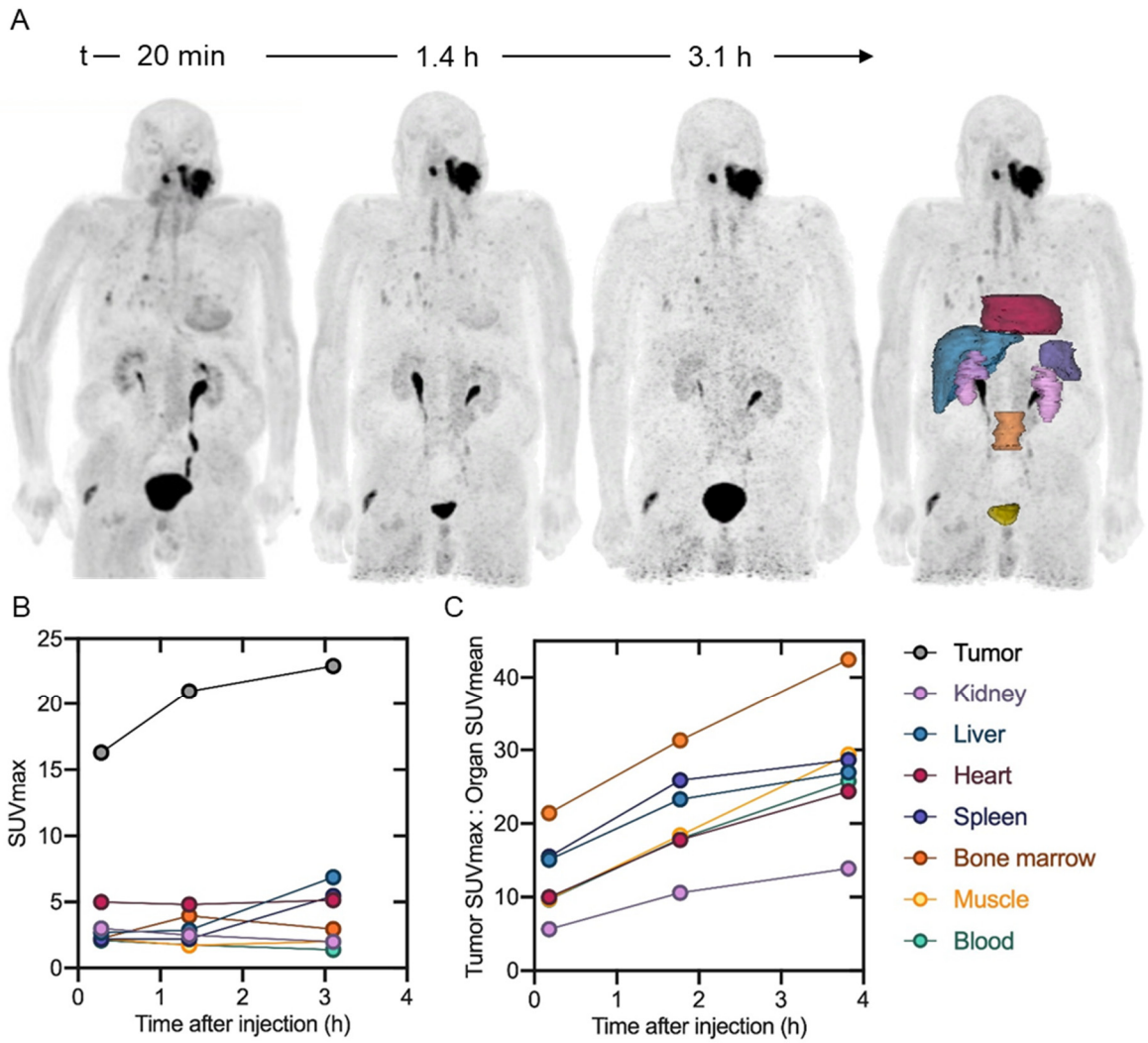


Figure 5.4 Patient 5 (Male) biodistribution. (A) $^{68}$Ga-FAPI-46 MIP and delineated organs for dose calculations, (B) SUVmax and (C) TBR at three timepoints following tracer injection. SUVmax and TBR for the bladder are excluded from the plot.

Table 5.2 Monoexponential function fitting parameters and TIACs (residence times) for $^{68}$Ga-FAPI-46 in various organs. Results are shown as mean (standard deviation) for n=6 patients. Per-patient coefficients and TIACs are available in Supplemental Table 2.

| Organ | $\%IA = A * \exp(-\lambda t)$ | | |
|---|---|---|---|
| | A (%IA) | λ ($h^{-1}$) | TIAC (h) |
| Liver | 3.49 (2.26) | 0.88 (0.12) | 0.0378 (0.0198) |
| Kidney | 2.07 (0.65) | 1.08 (0.26) | 0.0195 (0.0062) |
| Bladder | 6.82 (2.32) | 1.47 (0.91) | 0.0595 (0.0319) |
| Heart | 1.69 (0.30) | 0.94 (0.06) | 0.0182 (0.0035) |
| Spleen | 0.71 (0.62) | 0.96 (0.12) | 0.0074 (0.0066) |
| Marrow | 2.61 (0.63) | 2.05 (2.97) | 0.0250 (0.0114) |
| Uterus (n=2) | 0.13 (0.004) | 0.50 (0.07) | 0.0027 (0.0005) |

Table 5.3 $^{68}$Ga-FAPI-46 dosimetry summary of mean absorbed and effective doses using OLINDA/EXM v.1.1. The effective dose in ovaries and testes are equivalent due to use of hermaphroditic adult phantom weighting. Gallbladder wall and heart wall effective doses are not available based on the ICRP radiation weighting factors.

| | **Dose per injected activity (mGy/MBq) (n=6)** | | **Effective dose per injected activity (mSv/MBq) (n=6)** | |
|---|---|---|---|---|
| | **Mean** | **SD** | **Mean** | **SD** |
| Adrenals | 5.60E-03 | 8.12E-04 | 2.80E-05 | 4.04E-06 |
| Brain | 4.59E-03 | 6.12E-04 | 2.29E-05 | 3.06E-06 |
| Breasts | 4.55E-03 | 6.47E-04 | 2.28E-04 | 3.23E-05 |
| Gallbladder Wall | 5.62E-03 | 8.53E-04 | - | - |
| LLI Wall | 5.72E-03 | 6.96E-04 | 6.86E-04 | 8.33E-05 |
| Small Intestine | 5.48E-03 | 6.37E-04 | 2.74E-05 | 3.20E-06 |
| Stomach Wall | 5.32E-03 | 7.25E-04 | 6.38E-04 | 8.69E-05 |
| ULI Wall | 5.47E-03 | 6.97E-04 | 2.74E-05 | 3.50E-06 |
| Heart Wall | 1.11E-02 | 1.26E-03 | - | - |
| Kidneys | 1.60E-02 | 4.60E-03 | 7.98E-05 | 2.29E-05 |
| Liver | 1.01E-02 | 7.96E-03 | 5.05E-04 | 4.00E-04 |
| Lungs | 5.02E-03 | 7.09E-04 | 6.02E-04 | 8.48E-05 |
| Muscle | 4.96E-03 | 6.54E-04 | 2.48E-05 | 3.27E-06 |
| Ovaries | 5.76E-03 | 6.91E-04 | 1.15E-03 | 1.38E-04 |
| Pancreas | 5.69E-03 | 8.49E-04 | 2.84E-05 | 4.24E-06 |
| Red Marrow | 7.08E-03 | 1.00E-03 | 8.49E-04 | 1.20E-04 |
| Osteogenic Cells | 9.38E-03 | 1.30E-03 | 9.38E-05 | 1.30E-05 |
| Skin | 4.41E-03 | 6.33E-04 | 4.41E-05 | 6.33E-06 |
| Spleen | 6.96E-03 | 2.76E-03 | 3.48E-05 | 1.39E-05 |
| Testes | 4.88E-03 | 6.69E-04 | 1.15E-03 | 1.38E-04 |
| Thymus | 5.10E-03 | 6.40E-04 | 2.55E-05 | 3.21E-06 |
| Thyroid | 4.84E-03 | 5.72E-04 | 2.42E-04 | 2.85E-05 |
| Urinary Bladder Wall | 4.83E-02 | 8.55E-03 | 2.41E-03 | 4.27E-04 |
| Uterus | 9.54E-03 | 5.36E-03 | 4.76E-05 | 2.67E-05 |
| Total Body | 5.82E-03 | 1.18E-03 | 7.80E-03 | 1.31E-03 |
| Total Body Dose for 200 MBq | 1.16 | 0.24 mGy | 1.56 mSv | 0.26 mSv |

The organ with the highest absorbed dose was the urinary bladder wall with 4.83E-02 mGy/MBq, followed by the kidneys (1.60E-02 mGy/MBq), the heart wall (1.11E-02 mGy/MBq), liver (1.01E-02 mGy/MBq), and the uterus (9.54E-03 mGy/MBq). The remaining organ absorbed doses were all below 6.96E-03 mGy/MBq. Organs with the highest effective doses were the bladder wall (2.41E-03 mSv/MBq), followed by ovaries (1.15E-03 mSv/MBq) and red marrow (8.49E-04mSv/MBq). The average total body absorbed dose was 5.82E-03 mGy/MBq and the effective dose was 7.80E-03 mSv/MBq - similar, though lower than the reported values for related FAP-inhibitors (*132*). Thus for administration of 200 MBq (5.4 mCi) $^{68}$Ga-FAPI-46 the total body effective dose was 1.56 mSv ± 0.26 mSv. Together with approximately 3.7 mSv from one low-dose CT attenuation scan (*138*), this results in an estimated total effective dose of 5.3 mSv. Reported standard deviations arise from calculating the mean OLINDA/EXM dosimetry profile from six patients, and does not account for any possible errors involved in organ delineation.

### 5.3.3 Biodistribution

Biodistribution data assessed by SUV kinetics for Patient 3 (female) and Patient 5 (male) are shown in Figures 5.3 and 5.4, respectively. Pooled SUVmax and TBRs for all six patients are summarized in Figure 5.5, and SUVmean are also included in Table 5.4. The highest average normal organ SUVmax at all time points was observed in the liver, decreasing from an average SUVmax of 7.4 at 10 minutes to 5.0 by 3.3 hours (decline of 32%). Tracer uptake in the tumor was rapid with greater retention than normal organs: average SUVmax of 15.5 at 10 minutes, and 13.4 at 3.3 hours (decrease of 14%).

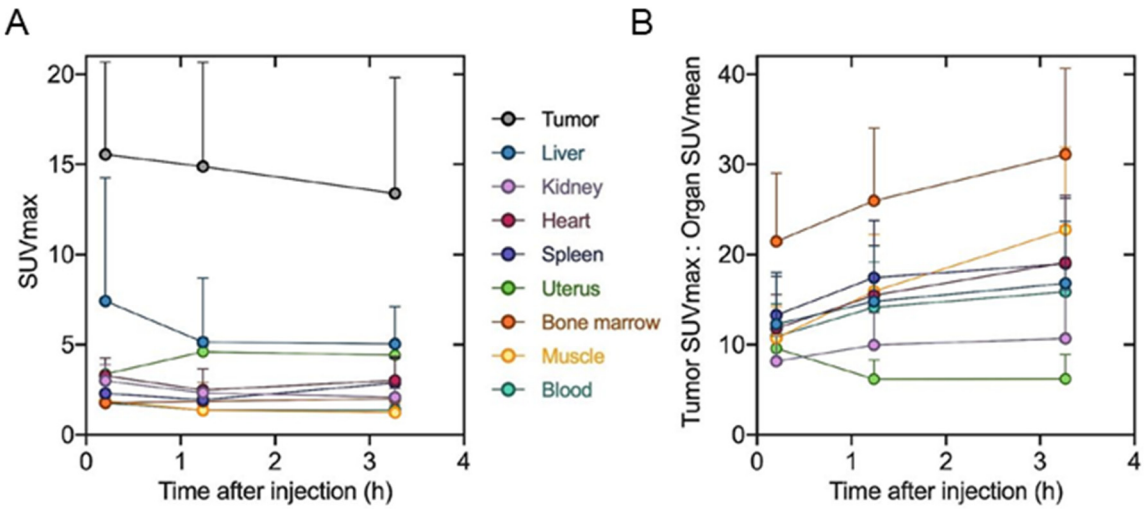


Figure 5.5 Pooled tumor and organ SUVmax (A) and TBR (B) at 3 time points after tracer injection (excluding bladder). Results are shown as mean and SD for 6 patients. Data values are available in Table 5.4.

Tumor and organ mean SUVs decreased in all patients from the first to last time points, while TBRs increased with time (with the exception of the uterus TBR). The highest TBR at all timepoints was observed in the marrow, with a ratio of 31 at 3.3 hours. The tumor-to-muscle ratio of 10.7 at 10 minutes increased more than 2-fold at 3.3 hours to 22.8. At 3.3 hours, the next highest TBRs were observed in the heart (19.1), spleen (18.9) and liver (16.8).

In summary, the tracer rapidly accumulated in the primary tumors and metastases with high maximum SUVs and low tracer uptake in normal tissue. The radioactivity was cleared steadily from the blood pool and was excreted via the kidneys, producing high contrast images.

Table 5.4 Pooled tumor-to-organ SUV ratios, SUVmax, and SUVmean values at three time points following $^{68}$Ga-FAPI-46 administration. Results are shown as mean (standard deviation) for n=6 patients.

| | | 10 minutes | 1.2 hours | 3.3 hours |
|---|---|---|---|---|
| SUVmax tumor: SUVmean organ | T : Liver | 12.28 (5.75) | 14.79 (6.22) | 16.80 (6.90) |
| | T : Kidney | 8.17 (2.76) | 9.96 (3.64) | 10.68 (5.34) |
| | T : Blood | 10.89 (3.61) | 14.15 (5.02) | 15.87 (7.30) |
| | T : Muscle | 10.71 (3.56) | 15.91 (6.33) | 22.77 (9.15) |
| | T: Heart | 11.78 (3.76) | 15.48 (5.49) | 19.11 (7.44) |
| | T : Spleen | 13.27 (4.31) | 17.44 (6.36) | 18.99 (7.27) |
| | T : Marrow | 21.46 (7.56) | 25.96 (8.09) | 31.13 (9.52) |
| | T: Uterus (n=2) | 9.60 (0.46) | 6.19 (2.12) | 6.20 (2.70) |
| SUVmax | Tumor | 15.54 (5.13) | 14.89 (5.77) | 13.39 (6.44) |
| | Liver | 7.42 (6.84) | 5.15 (3.56) | 5.04 (2.07) |
| | Kidney | 3.00 (0.89) | 2.33 (0.26) | 2.08 (0.49) |
| | Blood | 1.77 (0.35) | 1.38 (0.26) | 1.37 (0.31) |
| | Muscle | 1.87 (0.49) | 1.37 (0.45) | 1.24 (0.56) |
| | Heart | 3.28 (1.00) | 2.48 (1.17) | 3.02 (1.31) |
| | Spleen | 2.30 (0.23) | 1.94 (0.42) | 2.88 (1.38) |
| | Marrow | 1.77 (0.34) | 1.85 (1.05) | 2.00 (0.59) |
| | Uterus (n=2) | 3.37 (0.23) | 4.61 (0.32) | 4.42 (0.58) |
| SUVmean | Tumor | 3.87 (1.30) | 3.37 (1.11) | 2.81 (1.44) |
| | Liver | 1.51 (0.96) | 1.10 (0.58) | 0.81 (0.34) |
| | Kidney | 1.92 (0.34) | 1.47 (0.17) | 1.25 (0.22) |
| | Blood | 1.43 (0.25) | 1.03 (0.15) | 0.83 (0.15) |
| | Muscle | 1.48 (0.41) | 0.96 (0.32) | 0.61 (0.24) |
| | Heart | 1.32 (0.21) | 0.95 (0.15) | 0.68 (0.15) |
| | Spleen | 1.17 (0.20) | 0.85 (0.17) | 0.69 (0.16) |
| | Marrow | 0.73 (0.12) | 0.56 (0.11) | 0.41 (0.10) |
| | Uterus (n=2) | 2.08 (0.27) | 2.53 (0.24) | 1.97 (0.42) |

## 5.4 Discussion

This chapter describes the biodistribution of $^{68}$Ga-FAPI-46 and its estimated radiation dose deposition in organs of six cancer patients who underwent $^{68}$Ga-FAPI-46 PET/CT imaging at three time points. These are required for clinical translation and approval by regulatory agencies. These results have been used to provide the radiation safety data necessary to initiate clinical trials at UCLA investigating FAPI PET/CT in a variety of malignancies, including prostate cancer. These trials are currently ongoing.

The average effective whole-body dose for administration of 200 MBq $^{68}$Ga was 1.56 ± 0.26 mSv (7.80E-03 ± 1.31E-03 mSv/MBq). This estimate is slightly lower than the prior reported effective total body effective doses of other $^{68}$Ga-FAPI PET tracers: 1.80E-02 and 1.64E-02 mSv/MBq with $^{68}$Ga-FAPI-02 and $^{68}$Ga-FAPI-04, respectively (*132*). As a comparison, the reported effective dose for $^{68}$Ga-PSMA-11 ranges from 1.08E-02 – 2.46E-02 mSv/MBq (*139,140*), while the effective total body dose of both $^{68}$Ga-DOTATOC and $^{68}$Ga-DOTATATE is 2.10E-02 ± 3.00E-03 mSv/MBq (*141*).

Despite collection of patient-specific time-activity curves, the dose calculation was based on the stylized phantoms provided in OLINDA/EXM v.1.1. These estimates provide generalizable population mean absorbed dose values to organs by means of standard phantoms with selected customized organ masses. The reported standard deviations for the dosimetry estimates (Table 5.3) arise from taking the average of six sets of OLINDA/EXM v.1.1 patient reports. There are however sources of uncertainty not included in the analysis that are inherent in the dose calculation process that propagate to the final dose result. One of the most significant contributing sources of uncertainty is

the organ volume delineation itself (*58,142*). Inter-patient variability is also seen within Table 5.2 which shows relatively high standard deviations for time-activity curve-fitting parameters, most prominently observed in the liver.

While tumor dosimetry was not addressed directly in this study, the trend in biodistribution observed up to 3.3 hours after tracer administration demonstrates rapid tumor uptake and satisfactory retention. FAPI-46 biodistribution and dosimetry, including tumor dosimetry, using longer-lived isotopes for therapeutic applications remains to be studied. Such studies are essential to evaluate longer term tracer kinetics and thereby determine rational therapeutic isotope conjugates with well-matched physical half-life. Given the high achieved TBRs even at 10 minutes, early timepoint imaging with $^{68}$Ga-FAPI becomes possible; however, it should be considered that the contrast ratio improves with time.

This analysis was limited to six cancer patients (4 males; 2 females), and no healthy subjects. The basal FAP expression profile of a greater variety of cancers as well as in healthy subjects remains to be quantitatively assessed. It is however known that FAP is expressed at sites of arthritis, wound healing and active tissue remodeling, bone marrow mesenchymal cells, as well as in cirrhotic liver (*116,129,143,144*). The extent of this expression and its impact on imaging and potential therapies requires further clinical study. Implementation of FAP-targeted therapies thereby necessitates a better understanding of the comprehensive role of FAP, not only in the tumor microenvironment and carcinogenesis of different cancer types, but also its role in widespread bodily fibrotic mechanisms. Evaluation of $^{68}$Ga-FAPI-46 diagnostic accuracy was outside the study scope.

## 5.5 Conclusion

$^{68}$Ga-FAPI-46 PET/CT imaging is shown to have a favorable dosimetry profile. For administration of 200 MBq (5.4 mCi) of $^{68}$Ga-FAPI-46, the effective whole body dose of a PET scan is 1.56 mSv ± 0.26 mSv. When including a low dose CT (3.7 mSv), the dose of a $^{68}$Ga-FAPI-46 PET/CT scan is approximately 5.3 mSv in total. The biodistribution study showed high TBRs increasing over time, suggesting high diagnostic performance and favorable tracer kinetics for potential therapeutic applications. Long-term tracer biodistribution and dosimetry for longer-lived therapeutic isotope applications remains to be studied. Further work is needed to better identify indications for FAPI PET/CT, including its relevance in prostate cancer, as well as its diagnostic accuracy.

# Chapter 6: Assessing feasibility of a $^{99m}$Tc-labelled PSMA tracer

A version of this chapter has been published: Urbán S, Meyer C, Dahlbom M, Farkas I, Sipka G, Besenyi Z, Czernin J, Calais J, Pávics L. Radiation dosimetry of $^{99m}$Tc-PSMA-I&S: a single-center prospective study. J Nucl Med. 2021; 62:1075-1081.

## 6.1 Introduction

In the past decade, hundreds of thousands of PSMA-targeted PET scans using fluorine-18 or gallium-68 have been performed worldwide, reflecting the rapid and profound clinical adoption by the uro-oncologist community. However, technetium-99m is the most widely-used and accessible radionuclide for diagnostic imaging. Both SPECT/CT imaging systems and SPECT tracers are more affordable than PET/CT systems (*145*). Therefore, $^{99m}$Tc–labelled PSMA compounds could be a valuable cost-effective alternative in regions where access to PET imaging is limited. $^{99m}$Tc-PSMA imaging can also enable radioguided surgery (RGS) with intra-operative gamma detection for tumor localization. PSMA-targeted RGS can help guide urologic surgeons to detect prostate cancer lymph node metastases during surgery. Pelvic lymph nodes are often the first location of systemic spread and serve as a satellite for further dissemination (*146,147*). Once prostate cancer spreads, the likelihood of cancer cure dramatically decreases, with a 5-year survival rate of only 30% in patients with distant metastases (*148*). Therefore, surgical removal of affected lymph nodes may impact and improve patient outcomes (*149*).

To date, several different $^{99m}$Tc-99m-PSMA compounds have been developed. $^{99m}$Tc-Mas3-y-nal-k(Sub-KuE) ($^{99m}$Tc-PSMA-I&S – “imaging & surgery”) is a non-patented compound derived from the PSMA-I&T (“imaging & therapy”) precursor that can be obtained with a reliable kit-labeling procedure (*150*). Previous work has shown the utility of $^{99m}$PSMA-I&S for RGS (*151,152*). The primary objective of this study was to provide the radiation dosimetry analysis of $^{99m}$Tc-PSMA-I&S in healthy volunteers using a hybrid imaging method (sequential gamma planar imaging and one single SPECT/CT).

## 6.2 Materials and Methods

### 6.2.1 Study Design and Patients

This was a collaborative study with the University of Szeged, Hungary. All imaging studies were acquired at the University of Szeged and analyzed at UCLA. The study protocol was approved by the local institutional ethics committee for human biomedical trials at the University of Szeged (license #229/2017-SZTE). Four healthy men, free from any malignant disease, were enrolled in the dosimetry study. Patient characteristics are shown in Table 6.1.

Table 6.1 $^{99m}$Tc-PSMA-I&S patient characteristics

| Subject No. | Age (years) | Weight (kg) | Indication | Injected Activity (MBq) |
|---|---|---|---|---|
| 1 | 57 | 95 | Healthy Volunteer | 674 |
| 2 | 68 | 92 | Healthy Volunteer | 804 |
| 3 | 64 | 83 | Healthy Volunteer | 828 |
| 4 | 70 | 84 | Healthy Volunteer | 562 |

### 6.2 2 Image Acquisition

A hybrid imaging method was used to determine the dosimetry of $^{99m}$Tc-PSMA-I&S: multiple time-point whole-body planar imaging and one single quantitative SPECT/CT scan. The median injected activity of $^{99m}$Tc-PSMA-I&S was 739 MBq (range 562-828). Synthesis of $^{99m}$Tc-PSMA-I&S was performed as previously reported (*150*). In all healthy subjects, anterior and posterior scintigraphy was performed at 1, 2, 3, 6 and 24 hours after radiopharmaceutical administration using a Mediso AnyScan Trio triple head gamma camera equipped with low energy high-resolution collimators. The scanning speed was 18 cm/min, matrix size of 256×1024 pixels was used and a symmetric 20% window was set at 140 keV. In all volunteers, whole-body (mid-thighs to vertex) SPECT/CT images were acquired 6 hours after tracer administration. Quantitative SPECT images were acquired using a 128×128 matrix with a 20% energy window centered at 140 keV with adjacent scatter correction windows. A total of 96 projection views were acquired over 360 degrees using 10 seconds per view. SPECT data were iteratively reconstructed using 48 iterations and 4 subsets. CT-based attenuation

correction and point spread function corrections were used. CT images were acquired using low dose CT (120 KeV, 100 mAs, 1.5 pitch factor and 2.5 mm slice thickness). To improve the visibility of the gastrointestinal tract, Macrogol 1500 (50g/l) was administered orally one hour before SPECT/CT imaging.

### 6.2.3 Determination of Absorbed Doses

The source organs consisted of the salivary glands, kidneys, liver, small intestine, large intestine, spleen, urinary bladder, and the body remainder. Source organs contours were delineated manually on the CT images and propagated to the registered quantitative SPECT scans to determine the activity inside the source organs at 6 h after injection. Organ contours were also generated for the first time point scan of planar images, as shown in Figure 6.1 (including appropriate background regions for planar corrections). All ROIs were manually propagated to the subsequent images and were validated by two experienced nuclear medicine physicians.

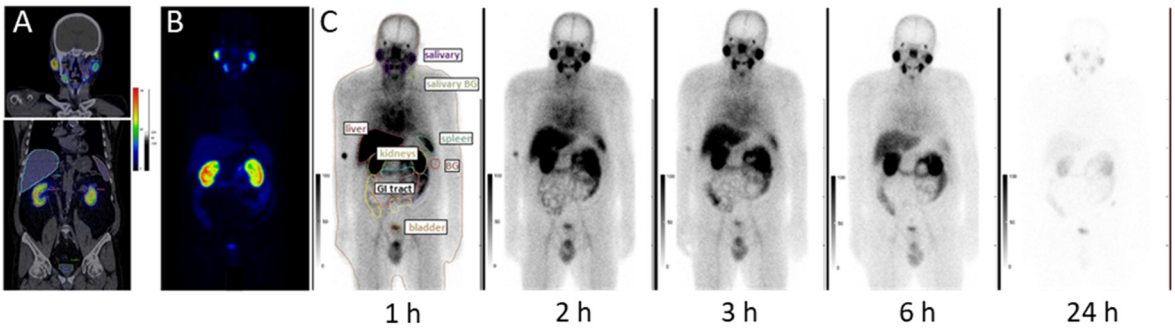


Figure 6.1 Source organ segmentations in a healthy volunteer. (Patient 3) (A) Organ contours on a fused $^{99m}$Tc-PSMA-I&S SPECT/CT scan, (B) on the SPECT 3D MIP, and on planar scintigraphy images (C). Whole body anterior and posterior $^{99m}$Tc-PSMA-I&S scintigraphy was performed at 1, 2, 3, 6 and 24 hours post-injection.

The mean counts were obtained for each organ and background ROI. Background-corrected organ counts were then calculated for both anterior and posterior whole body planar images. The geometric mean count was determined for every organ from the background-corrected anterior and posterior counts. The uptake fraction of injected activity was determined at each time point using the geometric mean counts from the planar images and the activity from the SPECT images.

Time-activity curve-fitting and dose calculations were performed using OLINDA/EXM v.2.0 software. For each volunteer, the non-decay-corrected percent injected activity in the source organs at each time point was used to generate time-activity curves. Patient-specific volumes were used for the liver, kidneys, small intestines, spleen, salivary glands and body remainder mass determination. Bi-exponential curve-fitting in OLINDA/EXM v.2.0 was used to fit the time-activity curves. The individual volunteer dose reports were compiled as means ± SD. Effective dose calculations were done using tissue weighting factors according to recommendations of the International Commission on Radiological Protection (*153*).

For method comparison and validation, investigators at the University of Szeged also calculated the radiation doses using a manual calculation method. The time-activity curves were fit with either mono- or bi-exponential functions using the Levenberg-Marquardt-based algorithm. Absorbed doses for the target organs were estimated based on the RAdiation Dose Assessment Resource (RADAR) scheme (*105*). Integration of the time-activity curve was calculated for every source organ. Wilcoxon signed-rank test was used to compare the doses obtained with the 2 methods.

## 6.3 Results

### 6.3.1 Radiation Dosimetry in Healthy Volunteers

The median injected activity of $^{99m}$Tc-PSMA-I&S was 739 MBq (range 562-828). No adverse events related to the injection of $^{99m}$Tc-PSMA-I&S were reported. Uptake was observed mainly in the salivary glands, liver, kidneys, spleen, small intestine, large intestine and urinary bladder. Figure 6.2 depicts an example of time-activity curves of normal organs in a healthy volunteer (Subject #3). Absorbed and effective doses using the manual RADAR and OLINDA/EXM method are presented in Table 6.2.

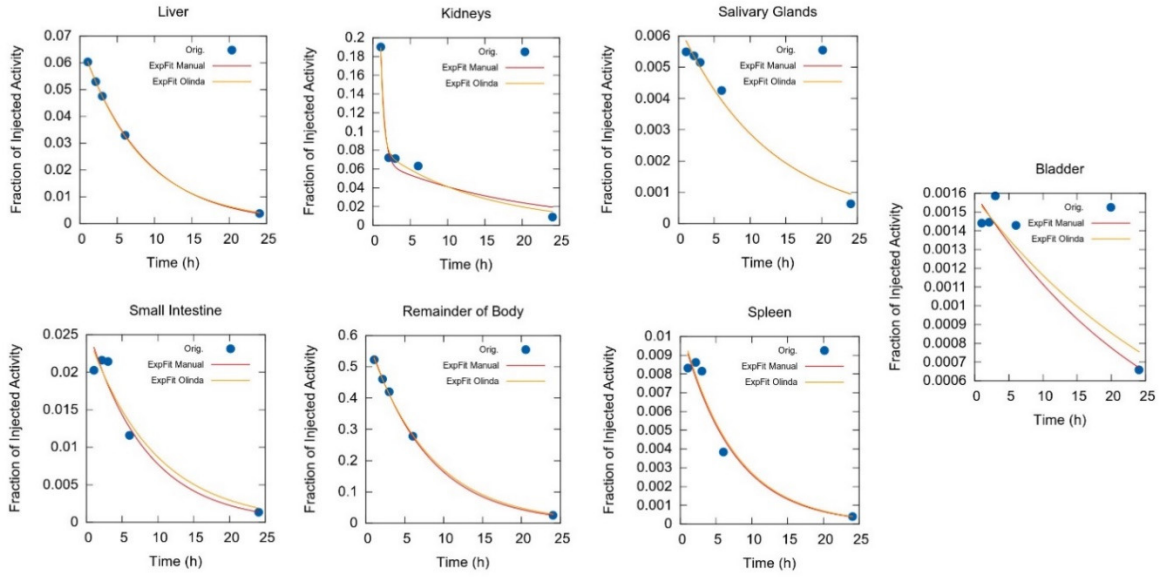


Figure 6.2 Representative time-activity-curves of normal organs in a healthy volunteer (Subject #3).

Table 6.2. Organ absorbed and effective doses of $^{99m}$Tc-PSMA-I&S comparing manual RADAR and OLINDA/EXM 2.0 methods

| Target Organ | Manual RADAR | | | OLINDA/EXM | | |
|---|---|---|---|---|---|---|
| | Organ doses (mGy/MBq) | | Effective Doses (mSv/MBq) | Organ doses (mGy/MBq) | | Effective Doses (mSv/MBq) |
| | Mean | SD | Mean | Mean | SD | Mean |
| Adrenals | 2.17E-02 | 4.54E-03 | 2.00E-04 | 2.17E-02 | 5.62E-03 | 2.00E-04 |
| Brain | 2.13E-03 | 1.59E-04 | 2.13E-05 | 2.15E-03 | 2.20E-04 | 2.15E-05 |
| Esophagus | 4.08E-03 | 2.60E-04 | 1.63E-04 | 3.98E-03 | 3.12E-04 | 1.59E-04 |
| Eyes | 2.02E-03 | 1.69E-04 | 0.00E-00 | 2.04E-03 | 2.23E-04 | 0.00E+00 |
| Gallbladder Wall | 8.98E-03 | 6.34E-04 | 8.30E-05 | 8.22E-03 | 5.89E-04 | 7.59E-05 |
| LLI/Left Colon | 1.02E-02 | 1.74E-03 | 4.94E-04 | 8.90E-03 | 7.57E-04 | 4.31E-04 |
| Small Intestine | 1.15E-02 | 3.93E-03 | 1.07E-04 | 1.19E-02 | 3.82E-03 | 1.10E-04 |
| Stomach Wall | 5.11E-03 | 2.84E-04 | 6.13E-04 | 5.00E-03 | 4.03E-04 | 6.00E-04 |
| ULI/Right Colon | 1.12E-02 | 2.66E-03 | 5.43E-04 | 8.49E-03 | 1.03E-03 | 4.12E-04 |
| Rectum | 4.56E-03 | 7.54E-04 | 1.05E-04 | 4.45E-03 | 4.74E-04 | 1.02E-04 |
| Heart Wall | 4.12E-03 | 2.65E-04 | 3.80E-05 | 4.00E-03 | 3.01E-04 | 3.69E-05 |
| Kidneys | 7.20E-02 | 2.34E-02 | 6.64E-04 | 7.33E-02 | 2.66E-02 | 6.77E-04 |
| Liver | 1.35E-02 | 1.92E-03 | 5.43E-04 | 1.23E-02 | 1.76E-03 | 4.93E-04 |
| Lungs | 3.46E-03 | 2.36E-04 | 4.15E-04 | 3.37E-03 | 2.82E-04 | 4.05E-04 |
| Pancreas | 7.59E-03 | 4.58E-04 | 7.01E-05 | 7.23E-03 | 2.77E-04 | 6.67E-05 |
| Prostate | 4.60E-03 | 6.36E-04 | 2.12E-05 | 4.50E-03 | 3.74E-04 | 2.08E-05 |
| Salivary Glands | 2.32E-02 | 3.05E-03 | 2.32E-04 | 2.21E-02 | 3.02E-03 | 2.21E-04 |
| Red Marrow | 3.43E-03 | 1.79E-04 | 4.12E-04 | 3.41E-03 | 2.56E-04 | 4.10E-04 |
| Osteogenic Cells | 6.39E-03 | 3.80E-04 | 6.39E-05 | 6.45E-03 | 5.03E-04 | 6.45E-05 |

Using the OLINDA/EXM method, the mean absorbed dose (mGy/MBq) was the highest in the kidneys (0.0733 mGy/MBq) followed by the salivary glands (0.0221

mGy/MBq), the adrenals (0.0217 mGy/MBq), the liver (0.0123 mGy/MBq), the spleen (0.0119 mGy/MBq) and the small intestine (0.0119 mGy/MBq. Total body effective doses of the four volunteers were: 0.0053 (#001), 0.0048 (#002), 0.0051 (#003) and 0.0055 (#004) mSv/MBq. The average total body effective dose was 0.0052 mSv/MBq. Considering the injected activities (range: 562-828 MBq), the effective doses of the four volunteers were between 3.11-4.23 mSv. There was no statistically significant difference between the paired mean effective doses (mSv/MBq) obtained by the two methods (paired Wilcoxon signed-rank test, $p>0.05$, LLI/ULI and left/right colon were excluded).

### 6.4 Discussion

This chapter reports the radiation dose of $^{99m}$Tc-PSMA-I&S in 4 healthy volunteers using a hybrid imaging method (multiple sequential time-point planar imaging and one single SPECT/CT). The average effective whole-body dose for administration of 700 MBq $^{99m}$Tc-PSMA I&S was 3.63 ± 0.64 mSv. The mean effective dose of $^{99m}$Tc-PSMA-I&S (0.0052 mSv/MBq) is similar to conventional $^{99m}$Tc-MDP used in SPECT/CT bone scintigraphy scans (0.004 mSv/MBq) (*154*).

Several other $^{99m}$Tc-PSMA compounds have been developed; including among others $^{99m}$Tc-EDDA/HYNIC-iPSMA (*155*), $^{99m}$Tc-tricarbonyl-iPSMA (*156*), $^{99m}$Tc-MIP-1404 and $^{99m}$Tc-MIP-1405 (*157*). In comparison with currently available $^{99m}$Tc-labeled PSMA inhibitors, the effective dose of $^{99m}$Tc-PSMA-I&S (0.0052 mSv/MBq) is similar to $^{99m}$Tc-EDDA/HYNIC-iPSMA (0.0046 mSv/MBq) and lower than $^{99m}$Tc-MIP-1404 (0.0088 mSv/MBq) and $^{99m}$Tc-MIP-1405 (0.0079 mSv/MBq) agents. The radiation absorbed

doses of 740 MBq $^{99m}$Tc-PSMA-I&S in the liver (9.10 mSv) was lower than those of $^{99m}$Tc-EDDA/HYNIC-iPSMA (liver = 10.73 mSv), however small intestine (8.83 mSv), spleen (8.83 mSv), kidneys (54.24 mSv) and salivary glands (16.35 mSv) receive higher doses than with $^{99m}$Tc -EDDA/HYNIC-iPSMA (small intestine = 2.42 mSv, spleen = 7.06 mSv, kidneys = 28.80 mSv, salivary glands = 9.69 mSv) (*9*). In comparison to PSMA PET tracers, the effective dose of $^{99m}$Tc-PSMA I&S is lower than $^{68}$Ga-labelled ($^{68}$Ga-PSMA-11 (0.0236 mSv/MBq, (*139*)) and $^{18}$F-labelled (0.0220 mSv/MBq, (*158*)) PSMA-targeted tracers.

Two dose calculation methods were compared in this work; however, the manual RADAR and OLINDA methods are largely very similar. The largest difference was in the exponential curve-fitting method: OLINDA was used for bi-exponential curve fitting in every case, whereas the manual method used mono- or bi-exponential fitting, based on visual assessment. As shown in Figure 6.2, there were cases when the mono-exponential fit was adequate (liver, spleen, remainder of body) by visual inspection. Therefore, there were only minor differences in the calculated number of disintegrations of source organs between both methods. Another difference was the segmentation definitions of the gastrointestinal tract: RADAR contained dose factors for the upper and lower large intestines, whereas OLINDA/EXM calculates doses to the left and right colon.

### 6.4.1 Biodistribution in prostate cancer patients

In addition to our dosimetry study, our collaborators at the University of Szeged conducted a related biodistribution study for $^{99m}$Tc-PSMA-I&S in patients with prostate

cancer. Ten patients with newly diagnosed prostate cancer were enrolled in the biodistribution study. All patients provided oral and written consent to enroll in the study. High uptake of $^{99m}$Tc-PSMA-I&S was observed 6 hours after injection both in primary tumors (10/10 patients, mean SUVmax 13), and in metastatic lesions (3/10 patients, mean SUVmax 6). The mean tumor:muscle, tumor:bladder, and tumor:intestines ratios in the primary tumors was 30, 1.6, and 5.6, respectively. For metastases, the metastatic tumor:muscle, tumor:bladder, and tumor:intestines ratios were 15, 0.6, and 3.2, respectively. Detailed biodistribution results are available in our collaborative publication (*159*). Examples of tumor uptake of $^{99m}$Tc-PSMA-I&S are shown in Figure 6.3. In this study, intestinal tracer accumulation was found to be highly variable, as similarly observed for bladder activity.

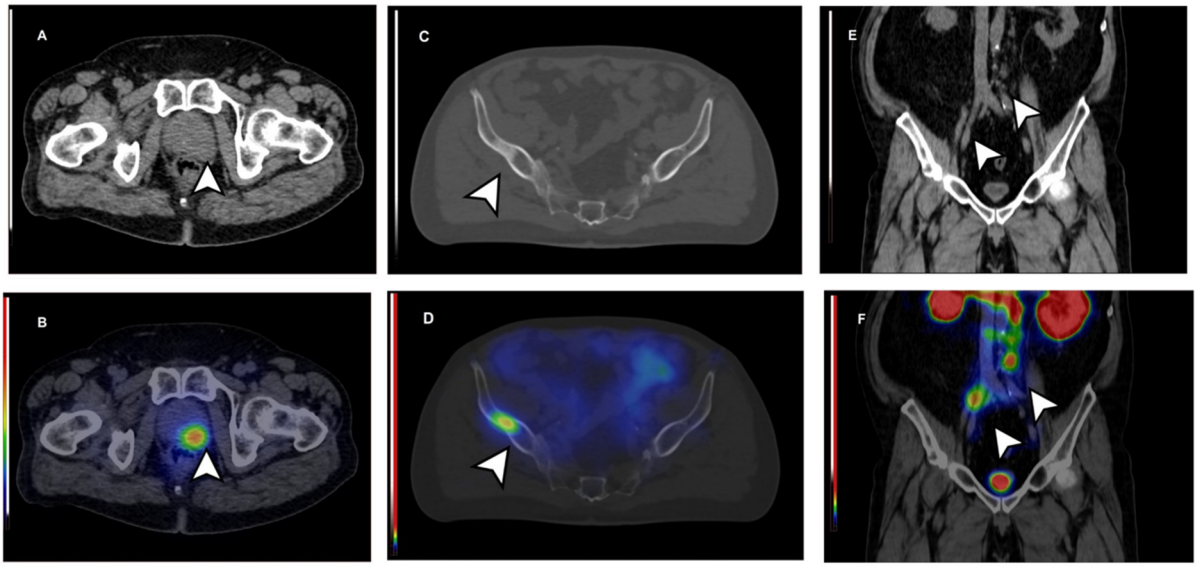


Figure 6.3 $^{99m}$Tc-PSMA-I&S SPECT/CT in cancer patients. (A-B) Patient with primary prostate cancer tumor lesion with high TBR (TBR: 42, SUVmax: 22); (C-D) Patient with a bone metastasis with high TBR (TBR: 26, SUVmax: 12); (E-F) Patient with a lymph node metastases with similarly high TBR (TBR: 24, SUVmax: 8.

### 6.4.2 $^{99m}$Tc-PSMA-I&S for Radioguided Surgery

Another potential application of $^{99m}$Tc-PSMA-I&S is with radioguided surgery (RGS). PSMA-targeted RGS can help guide urologists to detect prostate cancer lymph node metastases during surgery. PSMA-expressing lymph nodes with tracer uptake can be detected intraoperatively using a gamma probe. PSMA-targeted RGS was initially introduced with Indium-111-labeled PSMA ligands ($^{111}$In-PSMA-I&T) (*160*). However, $^{99m}$Tc-PSMA-I&S has emerged as the preferred radiopharmaceutical due to its lower cost, more widespread availability and superior imaging properties of $^{99m}$Tc compared with $^{111}$In (*150*).

Despite the use of PSMA-targeted PET as a tool for preoperative guidance, intraoperative detection and resection of small lesions remains challenging, especially because of the small dimension of the lymph node metastases, the technical difficulty of pelvic lymph node dissection, and atypical anatomic localization of the affected nodes. Prior studies reported that in up to two-thirds of patients who experienced disease recurrence after surgery, at least one lesion had already been detected on the preoperative PSMA-targeted PET imaging, suggesting that lymph node dissection was often not complete (*161*). PSMA-targeted RGS might increase the surgeon's confidence in intraoperative detection and complete dissection of metastatic lymph node lesions detected in the preoperative PSMA-targeted SPECT and PET imaging.

There are several European retrospective studies conducted in large cohorts that have now reported high rates of intraoperative tumor detection validated by histopathology, as well as improved treatment outcome (*151,152*). To summarize these

studies, higher rates of complete biochemical response were achieved in patients treated with PSMA-targeted RGS versus standard lymph node dissections: 66% vs. 27-59%, respectively (*152,162-164*). No adverse events related to the injection nor to the intraoperative use of the gamma probe were reported (*146,147,149*). Overall, complications related to PSMA-targeted RGS were comparable to those of the conventional surgery (*151,165*).

Currently, the timing of tracer administration for RGS has been determined empirically and may be improved. Even though $^{99m}$Tc-PSMA-I&S showed favorable TBR in both primary and metastatic lesions, differentiation between pathological and physiological uptake can be difficult due to regional organ background uptake, namely intestinal tracer accumulation. Based on the reported TBRs, tumor differentiation from the intestines may be reasonably achieved as soon as 6 hours after administration. However, waiting an even longer period, such as 24 hours may be preferable to take advantage of the relatively lower background activity by urinary and intestinal elimination in contrast with more stable tumor retention. Longer-term biodistribution was not covered in the scope of this study.

### 6.4.3 PSMA Radioguided Surgery at UCLA

Based on the promising results of PSMA-targeted RGS in Europe, and the radiation safety profile determined in this study, we designed an exploratory study conducted under the Radioactive Drug Research Committee Program to assess the feasibility of using $^{99m}$Tc-PSMA-I&S for application in RGS. The first objective of the study

was to establish the short and long-term tracer biodistribution in prostate cancer patients. This information is key to help move away from empirically-derived surgery times and determine the optimal time after tracer administration at which to perform the surgery so as to maximize the tumor-to-background ratio. The secondary objective was to validate the SPECT imaging findings with histopathological analysis of resected tissue from patients who undergo pelvic lymph node dissection.

We designed the study such that the first 5 patients will receive a first administration of $^{99m}$Tc-PSMA-I&S followed by five SPECT/CT scans to calculate the time-activity uptake curves for tumors and surrounding organs. The target imaging time points are as follows: 10 minutes, 4 hours, 19 hours, 27 hours and 43 hours. On the SPECT/CT images, in addition to the target lesions, normal tissues within the surrounding pelvic area are segmented, including the bladder, muscle, blood pool, intestines, and bone. For each region of interest, SUVmean, SUVmax, and the percent of injected activity are quantified. These curves are used to define the best time point at which the ratio between tumor uptake and the neighboring background signal is the highest (greatest TBR). Then, those patients will undergo a second administration of the radiotracer with a single SPECT/CT prior to surgery at the determined optimal time interval. The population-based average time interval between administration and surgery for these 5 patients will be used systematically to schedule the single radiotracer injection in all subsequent patients (n=25).

During each of the patients' surgeries, target lymph node metastases (as defined by preoperative imaging techniques) are detected intraoperatively using a handheld miniature gamma probe (IntraMedical Imaging, Hawthorne, California, USA). Resected

tissues are then processed by the UCLA Surgical Pathology core laboratory. Once the lymph nodes are grossed, we measure the absolute radioactivity in each lymph node using a gamma counter (Capintec CAPRAC-t, Mirion Technologies, Florham Park, NJ). Compared to a handheld miniature gamma probe, a standalone gamma counter system enables for quantitative measurement of the radionuclide activity with increased sensitivity. The aim of this analysis was to obtain an accurate measurement of the accumulated radioactivity in the resected specimens suspicious for malignancy (radioactive-positive by gamma probe). The gamma detector response in counts/minute is converted to activities based on standard calibrations for $^{99m}$Tc. The samples are then transferred back to the pathology core laboratory for histologic analysis. Besides conventional hematoxylin-eosin staining, analysis includes PSMA immunohistochemistry using an anti-PSMA antibody. Immunohistochemistry scoring is performed by the pathologist using a semiquantitative scoring system. All patients are asked to consent for analyzing their tumor tissue for PSMA expression.

The ultimate goal of these various measurements is to evaluate the association between $^{99m}$Tc-PSMA-I&S uptake as seen by SPECT imaging, ex-vivo gamma counter measurements, and the degree of PSMA expression. The hypothesis is that greater tracer uptake by imaging will correlate with greater count rates by ex-vivo measurements and more intense PSMA expression levels.

To date, 3 patients have enrolled and completed PSMA-targeted radioguided surgery for pelvic lymph node dissection at UCLA. Figure 6.4 shows the SPECT imaging time course for a single patient with lymph node metastases at the left common and external iliac arteries. At the earliest time point of imaging (10 minutes), it is difficult to

distinguish any malignancies, especially in these lymph nodes next to arteries, due to high uptake in blood as the tracer is still in circulation. However, by 3 hours, the external iliac lymph node is easily visualized, with improving contrast over time. TBR time-activity curves are shown in Figure 6.4B. Based on these curves, the recommended surgery time for this patient was between 15-22 hours after tracer administration. This patient then underwent another $^{99m}$Tc-PSMA-I&S administration one month later followed by surgery 20 hours later. Multiple lymph node packets were successfully intraoperatively detected in-vivo, resected, measured for radioactivity, and processed for histological analysis. While PSMA immunohistochemistry is still pending, H&E staining confirmed that the resected target lymph nodes were cancerous (Figure 6.4C).

This study is ongoing. When enrollment of five patients is completed, we will compare the biodistribution curves and compute average TBRs to determine an average favorable time between injection and surgery that yields favorable contrast between target lesions and surrounding tissues. We are also working in collaboration with surgeons on a comparison of different commercially-available gamma probes for intraoperative use.

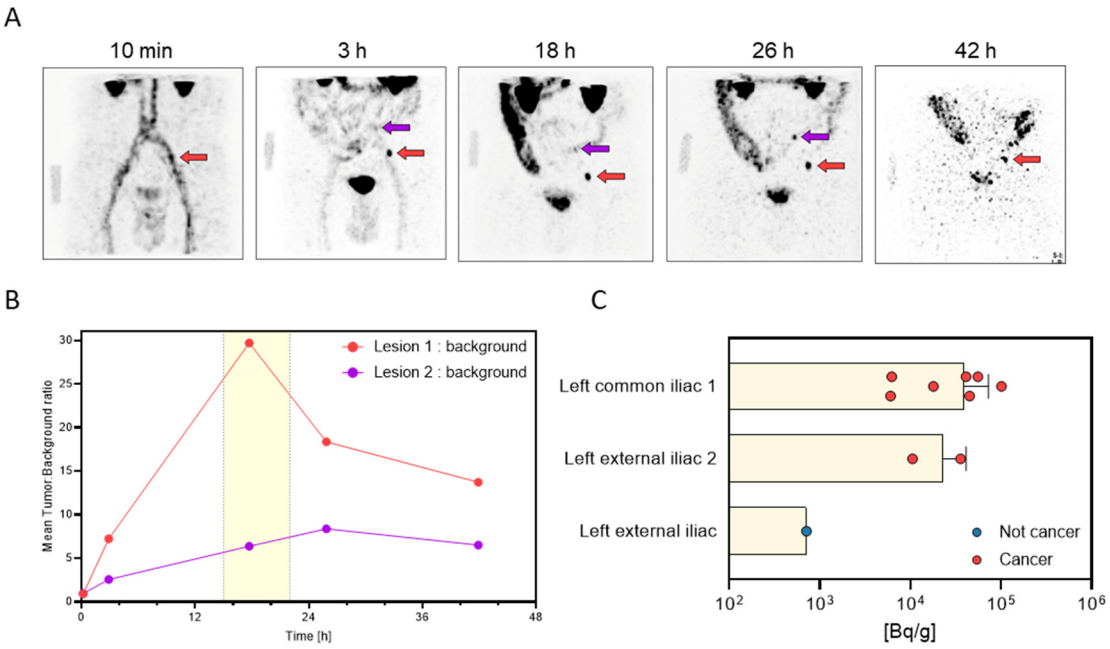


Figure 6.4 $^{99m}$Tc-PSMA-I&S serial imaging and lesion analysis. (A) Pelvic SPECT MIPs at 5 time points following administration of $^{99m}$Tc-PSMA-I&S in a single patient. Arrows point to target lymph node metastases in a left common iliac lymph node and left external iliac lymph node. (B) Tumor-to-background ratio curves over time for both target lesions. Background consists of the mean uptake in blood, muscle, and nearby digestive activity. (C) Radioactivity measurements in Becquerel/gram, corrected to the time of surgery. Bar graphs show mean activity for each lymph node packet submitted for histologic analysis. Red points indicate individual lymph nodes that were positive for cancer.

## 6.5 Conclusion

This dosimetry study of $^{99m}$Tc-PSMA-I&S showed that injected activities of 562-828 MBq translate to estimated effective doses of 3.1 - 4.2 mSv (OLINDA/EXM method), which is similar to the effective doses from other $^{99m}$Tc-PSMA inhibitors. Larger trials, including the ongoing trial at UCLA towards its application in radioguided surgery, are needed to further define its capabilities and utility in the management of prostate cancer.

# Chapter 7: Patient-specific radiation dosimetry of $^{177}$Lu-PSMA-617

A version of this chapter has been presented at the 2021 SNMMI Annual Meeting and is the basis for a manuscript in preparation: Meyer C, Mirando D, Adams T, Ranganathan D, Esfandiari R, Delpassand E, Czernin J, Calais J, Dahlbom M. Dosimetry of mCRPC patients treated with 177Lu-PSMA-617: a post-hoc analysis of a prospective phase 2 study. [Manuscript in preparation]

## 7.1 Introduction

For EBRT, individualized treatments are standard practice. However, the current treatment paradigm in radionuclide therapy is to treat with fixed activities for the same number of cycles at fixed intervals, with some empirical adjustments. RNT with a fixed treatment activity neglects the fact that the disease state, tumor load and biology can vary widely among patients. Given that the mechanism of action of RNT is by targeted radiation, the dose will be a function of individual target expression and pharmacokinetics, and as such warrants dose planning and verification. To move away from this “one size fits all” approach to more individualized treatment, dosimetry can be used to devise safe therapeutic activities to deliver maximal tumor doses while delivering as low as achievable doses to non-target volumes.

To date, there are few publications reporting the patient-specific dosimetry of patients treated with $^{177}$Lu-PSMA-617. Delker et al. were the first to report dosimetry in a cohort of 5 patients using a combination planar and SPECT imaging approach (*34*). The only other published report of individualized therapy dosimetry for $^{177}$Lu-PSMA-617 was

performed by Violet et al. in a cohort of 30 patients based on 3 quantitative SPECT/CT scans acquired after the initial therapy cycle (*36*). Between these studies, estimates of kidney and salivary gland doses differed by 33% and 59%, respectively. However, direct comparison between reports is confounded by varied patient populations and study size.

In addition, more investigation is needed on the performance of different imaging modalities (and combination thereof) for dosimetry estimates. The aim of this study was to estimate the absorbed doses in mCRPC patients treated with $^{177}$Lu-PSMA-617 using a hybrid imaging approach: one single SPECT/CT and multiple planar imaging scans. Specifically, our objective was to quantify the radiation absorbed doses to the kidneys and tumors of $^{177}$Lu-PSMA-617-treated patients. The kidneys are often the dose-limiting organ in radiopharmaceutical therapies, due to their involvement in biologic elimination. The rationale for this study is that the overall treatment efficacy is largely governed by the radiation dose deposited in the tumor targets, and toxicity is determined by the sparing of other tissues.

## 7.2 Materials and Methods

### 7.2.1 Study Design and Patient Population

This work is a retrospective analysis of the absorbed dose in tumors and kidneys in patients treated with $^{177}$Lu-PSMA-617 as part of the prospective multicenter phase II trial RESIST-PC (NCT03042312). Participating sites in the trial were UCLA (Los Angeles, CA) and Excel Diagnostics (Houston, TX). Included patients had progressive mCRPC after androgen deprivation therapy (ADT) with a positive PSMA screening PET scan to

confirm target expression. The aim of the trial was to evaluate the efficacy and toxicity of two different administered activities of $^{177}$Lu-PSMA-617: 6.0 and 7.4 GBq. Patients received up to 4 cycles of treatment every 8 weeks; however, serial imaging for dosimetry was only performed for the first cycle.

In total, 72 patients were enrolled in the trial (51 from UCLA and 21 from Excel Diagnostics). Patients were excluded from the dosimetry analysis only if they had insufficient post-therapy imaging data. This analysis includes 49 patients who received treatment with $^{177}$Lu-PSMA-617 and had complete imaging data available. Patient cohort characteristics are shown in Table 7.1. Previous studies have reported on the safety findings on this trial, concluding that the treatment is overall well-tolerated with a low toxicity profile (*166*).

Table 7.1 $^{177}$Lu-PSMA-617 dosimetry patient characteristics

| | **Treatment cohort (n=49)** | |
|---|---|---|
| | **6.0 GBq (n=16)** | **7.4 GBq (n=33)** |
| Median age (range) [y] | 74 (57 - 95) | 70 (55 - 84) |
| Median injected activity (range) [GBq] | 6.1 (5.1 - 7.8) | 7.4 (5.6 - 8.1) |
| % Prior chemotherapy | 75 | 75 |

### 7.2.2 Image Acquisition

Following administration of $^{177}$Lu-PSMA-617, each patient underwent whole body scintigraphy at +4 h, 24 h, 48 h, and 72 h. A late imaging time point after 4-9 days was optional. A schematic view of the imaging workflow is shown in Figure 7.1. Images were

acquired with a Siemens Symbia Intevo at UCLA and a Siemens Symbia T2 at Excel Diagnostics. Planar images were acquired with a symmetric 20% energy window centered on 208 keV and medium energy collimation. The whole body scan rate was 20 cm/min with fixed head position (matrix 1024×256). Each patient also underwent SPECT/CT imaging 24 h after treatment covering 2 bed positions of the abdomen and pelvis. The total number of views acquired were 120 (60 per head) with a frame duration of 15 s/view, with auto-contouring activated. Scatter correction was applied using triple energy windows (10% width upper and lower scatter windows around 208 keV). SPECT acquisitions were followed by a low-dose CT acquisition for attenuation correction (parameters: 130 kVp, 30 mAs, 5.0 mm slice thickness, pixel size 0.99 mm). Data were reconstructed using Flash 3D reconstruction algorithm (6i6s with matrix 128×128). No post-reconstruction filtering was applied.

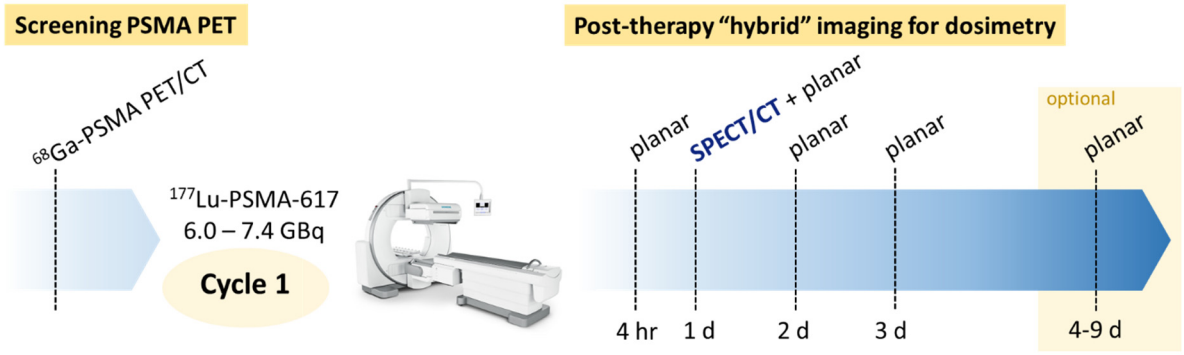


Figure 7.1 Dosimetry imaging workflow. Patients are first screened for PSMA PET expression before treatment with $^{177}$Lu-PSMA-617 followed by serial planar and SPECT/CT imaging procedures.

The quantification of SPECT images is crucial for dosimetric applications because the number of counts in a region is the basis for the calculation of absorbed energy. This

requires accurate calibration of SPECT cameras, which is particularly important with our multicenter collaboration. The $^{177}$Lu SPECT images were quantified using phantom-derived calibration factors, as suggested by the EANM dosimetry guidelines (*111*). Calibration measurements were performed using a phantom with known $^{177}$Lu activity concentration imaged with the same SPECT acquisition parameters used for the patients, as outlined above. The camera sensitivities for the Symbia Intevo and Symbia T2 were 20.12 and 19.58 cps/MBq, respectively.

### 7.2.3 Dosimetry

Image and dosimetry analysis were performed using MIM SurePlan (MIM Software, Cleveland, OH). The first step in the workflow for hybrid planar/SPECT dosimetry is to segment the regions of interest on the +24 h SPECT/CT. First, bilateral kidneys were automatically contoured using a CT-based neural network framework (Contour Protégé AI) (*167*). Then, the neural network generated kidney contours were manually adjusted to include only kidney cortex tissue, excluding urinary activity in renal calyces (as done similarly in previous studies – see Figure 5.1).

For tumor dosimetry, tumors were contoured on the +24 h SPECT sequence semi-automatically with the support of an automatic edge detection algorithm (PET Edge Plus). Lesions were selected if they were clearly visually identifiable on all time points of planar imaging with 1 mL as a minimum volume threshold. Lesions were excluded if there was indistinguishable overlapping activity signal from other tissues on the planar scans. The

anatomical location depth of each lesion was noted to consider the optimal view on the planar images for visualization and activity quantification.

Then, planar and SPECT scans were automatically co-registered to each other using rigid registration with the option for the user to manually modify the alignment. Given that patients return over multiple days for repeated imaging procedures, there can be considerable differences in patient positioning, particularly for the head and neck. We therefore performed two distinct registrations, one each for prioritizing alignment in the kidneys and another prioritizing co-registration of the tumor targets amid the sequential images. A similar approach was carried out in another dosimetry study to optimize region-specific co-registration (*168*).

Following registration, the 3D VOIs from the SPECT/CT are propagated onto the planar series as 2D ROIs. Background regions for each ROI are generated to compute the net counts in each region. It is more important at this step to ensure that the contoured areas represent the true mean uptake of the tissue of interest rather than anatomically accurate structures. For example, in cases where gastro-intestinal activity may overlap with kidney uptake, the overlap should be excluded from the kidney contour. In the case of intense overlapping activity that can't be distinguished between structures, the affected scan time point can be excluded entirely from the analysis. However, we enforced a minimum of three measurements for time-activity curves. Kidney time-activity curves were derived only from counts in the posterior views where the kidneys are clearly visualized. Depending on the anatomical location of the lesions as previously noted, tumor time-activity curves were generated on a lesion basis from counts in the anterior or posterior views, or from the geometric mean.

After selection of the appropriate measurement time points and views, the time-activity curves are fit with the best-fitting automatically-determined exponential function. MIM SurePlan uses the Levenberg-Marquadt algorithm and Akaike information criterion to first fit then select the best-fitting model for the data, respectively. The time-activity curves represent the mean relative kinetics of $^{177}$Lu-PSMA-617 in each target over time. Given that we also have a quantitative SPECT acquisition at +24 h, the counts in the corresponding region on SPECT are used to scale each curve to reflect the absolute activity kinetics.

Then, the scaled best-fit curve function is integrated over time to yield the time-integrated activity, or, the cumulated activity until the radiopharmaceutical is completely decayed and excreted from the body. In this case, we are calculating organ or region-level doses rather than voxelized doses. So, it is assumed that the time-integrated activity is homogeneously distributed in each ROI. Finally, the time-integrated activity distribution is convolved with a spatial $^{177}$Lu dose kernel to yield estimates of organ-level kidney doses and tumor doses. The dose kernel used in the workflow is derived from Monte Carlo radiation transport simulations of $^{177}$Lu decay; however, it does not perform a patient-specific simulation for each case.

## 7.3 Results

### 7.3.1 Patient Population

In total, 72 patients were enrolled in this trial. However, 8 patients did not undergo treatment with $^{177}$Lu-PSMA-617 and were necessarily excluded from the analysis. In

addition, 10 patients were excluded for insufficient post-therapy imaging data. This preliminary report includes 49 patients in the renal dose analysis, and 32 patients are included for tumor dose analysis. Patient characteristics are available in Table 7.1. All included patients have serial whole body planar images at 4, 24, 48, and 72 hours after injection. Nine patients participated in a late planar imaging scan 4-9 days after treatment administration.

### 7.3.2 Kidney Dosimetry

The median injected activity for the 49 patients was 7.2 GBq (range: 5.1 – 8.1 GBq). A representative patient example for kidney region segmentation and corresponding time-activity curves is shown in Figure 7.2. In all cases, the time-activity curves were derived from counts on the posterior planar view only. This was done to minimize regions of overlapping activity seen on the anterior view, such as gastrointestinal uptake.

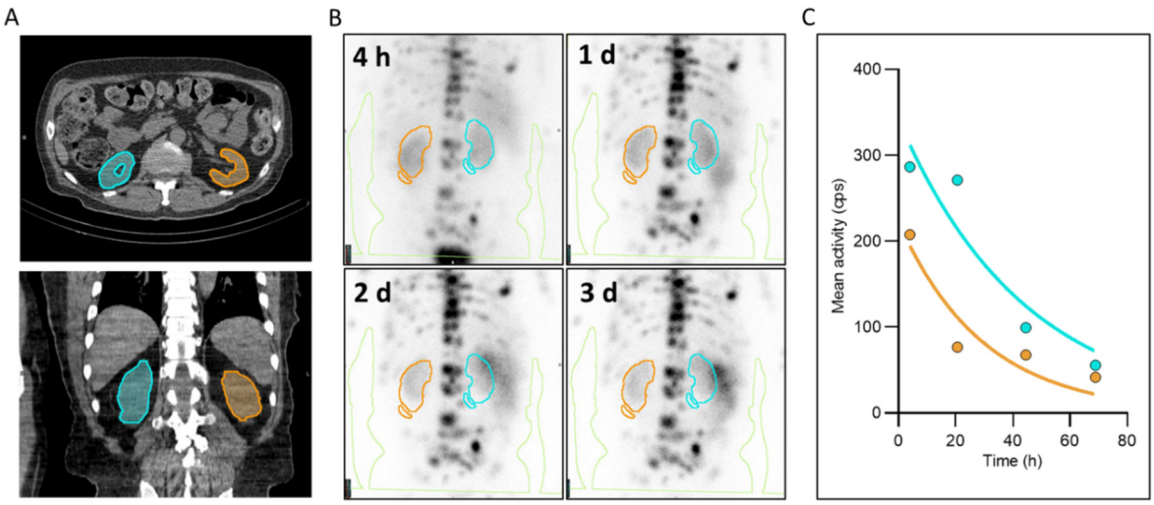


Figure 7.2 Kidney contouring and time-activity curves. (A) Segmentation of bilateral kidney ROIs on the CT from the +24h SPECT/CT acquisition. (B) Propagation of kidney contours onto the planar imaging series with corresponding background regions. Posterior planar views are shown. (C) Time-activity curves for kidneys derived from counts in the posterior planar views.

After time-activity curve generation and curve-fitting, the cumulated activity is convolved with a $^{177}$Lu spatial dose kernel to yield mean kidney level doses. In 49 patients, the average kidney absorbed dose was 2.46 ± 1.00 Gy (range: 0.77 – 4.63 Gy), or, 0.35 ± 0.14 Gy/GBq (range: 0.10 – 0.62 Gy/GBq) when normalized by the injected activity (Figure 7.3). Assuming the median injected activity of 7.2 GBq, the per-cycle kidney dose would be 2.6 Gy. The frequency distribution of kidney doses revealed a 6-fold difference in dose delivered to the critical organ across this cohort. While the kidney dose tends to increase with increasing applied injected activity (Figure 7.3D), there was no significant correlation (Spearman correlation coefficient $\rho$=0.21, p=0.15).

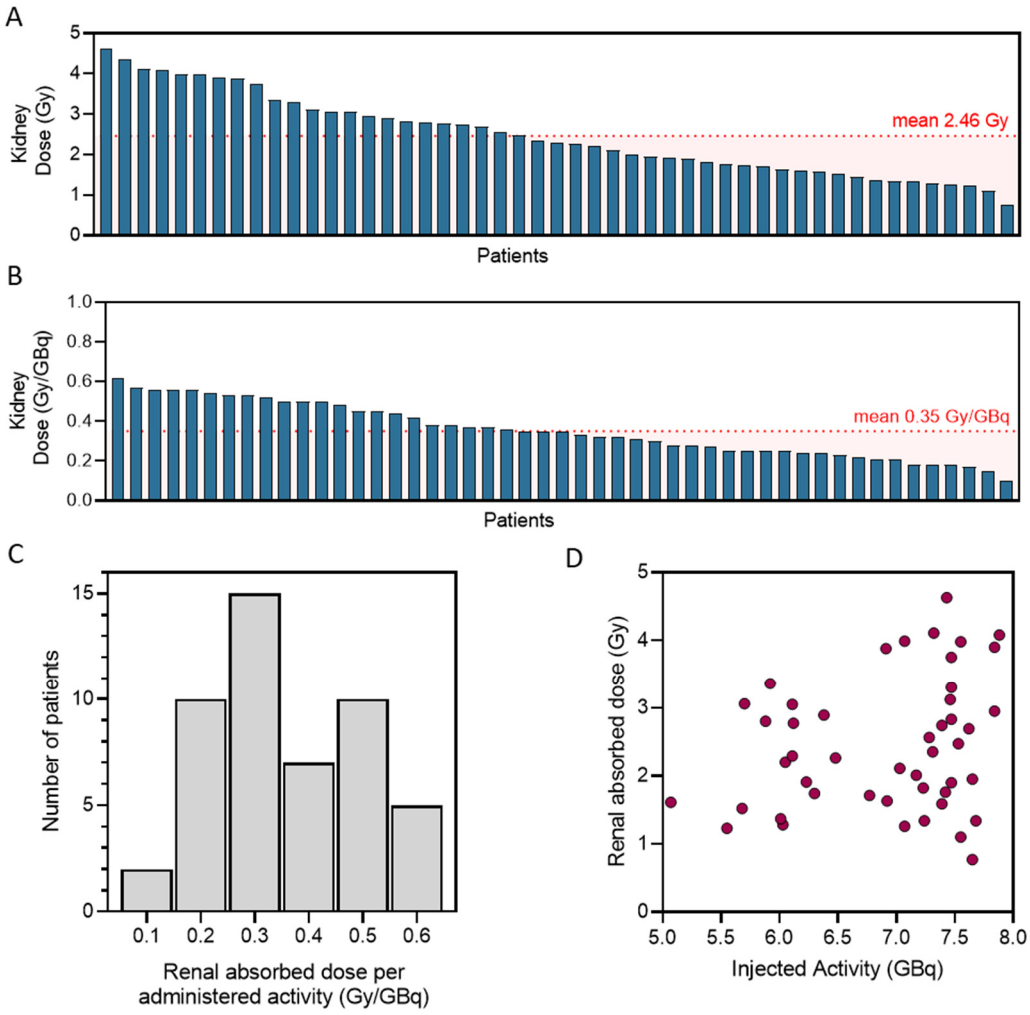


Figure 7.3. Kidney dosimetry. (A) Individual kidney doses (mean of bilateral kidney doses). (B) Individual kidney doses normalized by the respective injected activity. (C) Histogram showing frequency distribution of kidney absorbed doses. (D) Kidney doses versus injected activity (Spearman correlation coefficient ρ=0.21).

### 7.3.3 Tumor Dosimetry

The median injected activity for the 32 patients was 7.3 GBq (range: 5.5 – 8.1 GBq). In total, 289 lesions were included in the analysis (median 10 per patient, range: 1 - 18). The majority of lesions were skeletal (n=244) with some soft tissue involvement, such as in the liver (n=45). The mean tumor absorbed dose across all 289 lesions was 21.9 Gy,

or 3.22 ± 4.32 Gy/GBq for the first cycle. Individual lesion doses per patient are shown in Figure 7.4. Assuming the median injected activity of 7.3 GBq, the per-cycle dose would be 23.2 Gy per metastatic lesion. The mean dose in bone lesions and soft-tissue lesions was 3.1 ± 4.2 Gy/GBq (n=244) and 3.8 ± 4.9 Gy/GBq (n=45), respectively. The difference in absorbed dose between skeletal and soft tissue lesions was not statistically significant (p=0.26 by two-tailed unpaired t-test). Tumor doses varied significantly both within and between patients, suggesting heterogeneity on both inter-tumor and inter-patient scales. The range of individual lesion doses varied from 0.1 - 35.0 Gy/GBq.

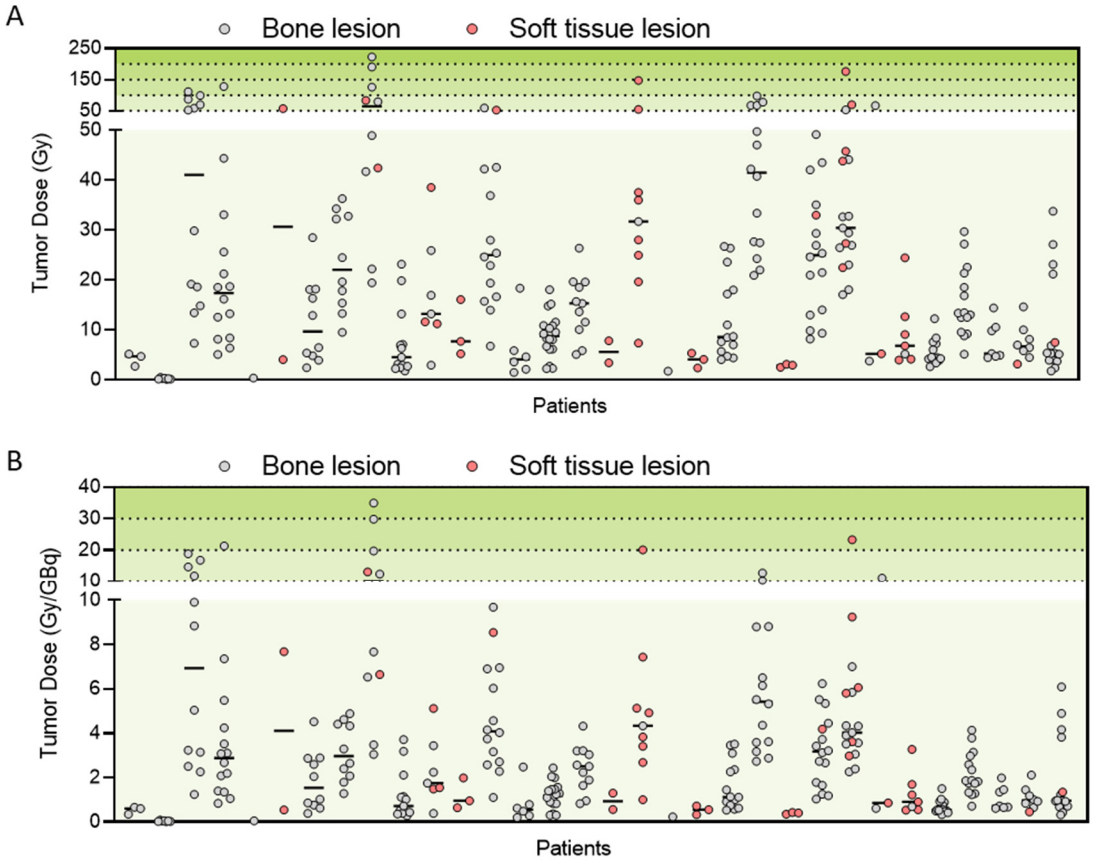


Figure 7.4 Individual tumor doses. (A) Absorbed dose to individual metastatic lesions (B) Absorbed doses normalized by the respective injected activity.

At the per-patient level, average whole body tumor doses varied from 0.1 – 13.7 Gy/GBq (Figure 7.5). From the dose frequency distribution, we can see that the majority of patients (18/32) receive less than 2 Gy/GBq on average to the tumor targets. While a weakly positive association was observed between the applied injected activity and the resultant kidney doses, there was no evidence that the tumor doses between different patients correlated with injected activity (Spearman correlation coefficient $\rho$=-0.01, p=0.94) (Figure 7.5F). We also investigated whether there was any correlation between the absorbed dose in the kidneys and the mean whole body dose to the tumors within the same patients. As shown in Figure 7.5D, we did not observe a significant association between the dose to the kidneys and average tumor dose (Spearman correlation coefficient $\rho$=0.29, p=0.10).

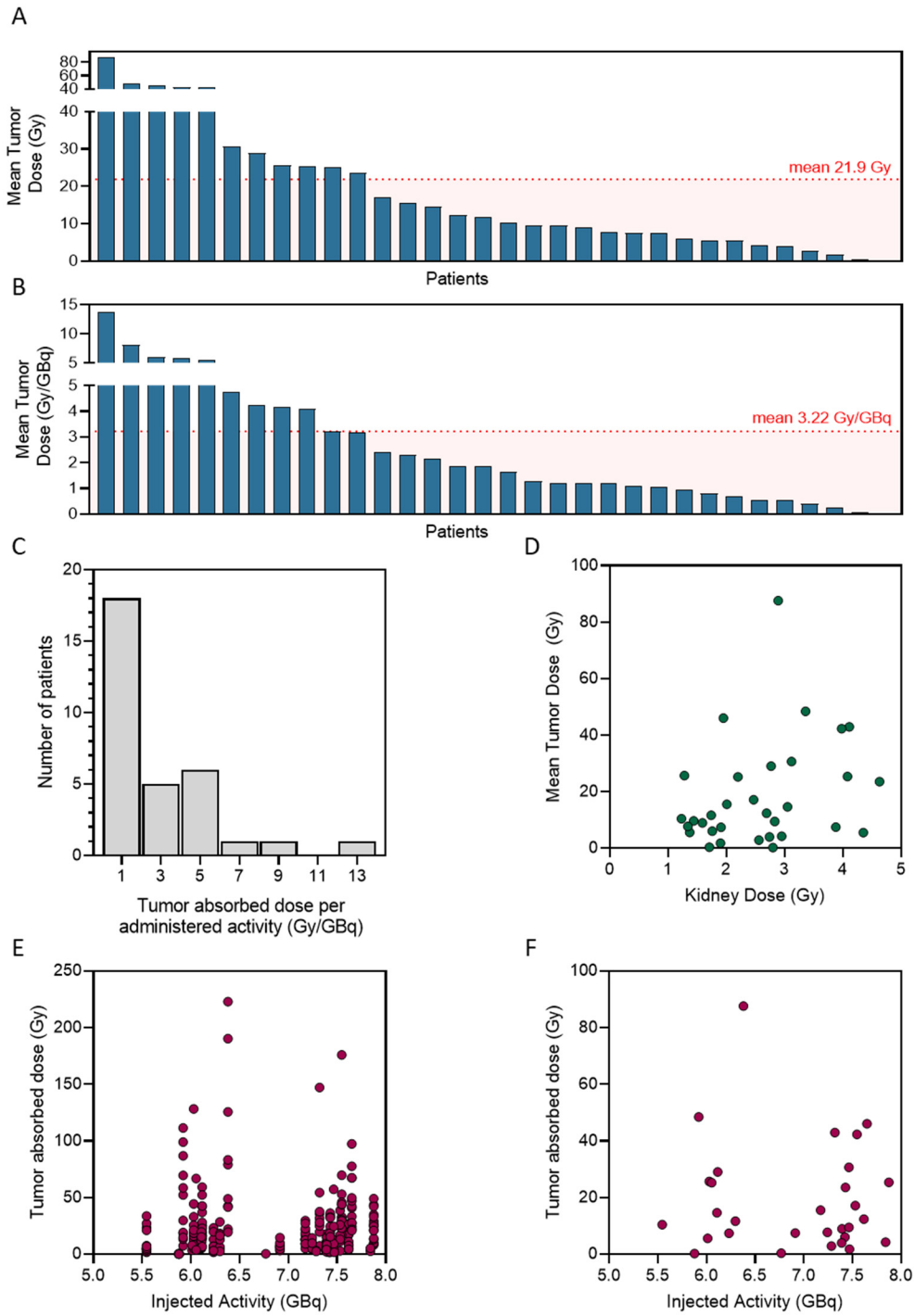


Figure 7.5. Tumor dosimetry. (A) Mean tumor doses per patient. (B) Mean tumor doses per patient normalized by the respective injected activity. (C) Histogram showing frequency distribution of mean tumor absorbed doses. (D) Mean tumor dose versus kidney doses (Spearman correlation coefficient ρ=0.29). (E) Individual tumor doses versus injected activity. (F) Mean tumor doses versus injected activity (Spearman correlation coefficient ρ=-0.01).

## 7.4 Discussion

This chapter describes a study to retrospectively calculate the absorbed dose to kidneys and metastatic tumors in patients treated with $^{177}$Lu-PSMA-617. We report an average kidney dose of 0.35 ± 0.14 Gy/GBq, which is comparable to a previously published study examining patient-specific kidney doses in Lu-PSMA therapy (*36*). The dosimetry study by Violet et al. reported a mean kidney dose of 0.39 ± 0.15 Gy/GBq. Of note, their dosimetry estimate is based on 3 time points of SPECT/CT imaging to quantify radiopharmaceutical distribution on a voxel level. Typically, SPECT imaging at all time points is considered the best modality for quantitative accuracy; however, for logistical purposes SPECT imaging at all time points may not always be feasible (*169*). Despite using different imaging modalities, our kidney dose estimates are still in good agreement. Comparing both studies, the standard deviation in kidney dose is about 40% in both, suggesting significant effects of patient-specific uptake and excretion kinetics in kidneys.

Regarding the per-cycle kidney dose, assuming a median injected activity of 7.2 GBq, the resultant kidney dose is 2.6 Gy, which is typically considered to be a well-tolerated kidney dose (*34*). The kidney dose limit is oft-quoted as 18-23 Gy, where 18 Gy is considered most safe, and 23 Gy is a commonly used tolerance dose accepting a 5% risk of complication in 5 years (*110,170*). Given that none of the patients were near approaching this dose limit in their first cycle, we then posed the question of how many patients, in theory, could have tolerated increased treatment activities on subsequent cycles? Figure 7.6 shows the hypothetical cumulative kidney dose the patients would have received if administered 4 cycles of the same activity. We also assumed that the

kidney dose does not significantly change between treatment cycles with equivalent activities. We found that the cumulative dose in 18/49 patients was at least 67% lower than the 23 Gy dose limit thus suggesting a potential for multiple fold baseline dose escalation to be safely tolerated.

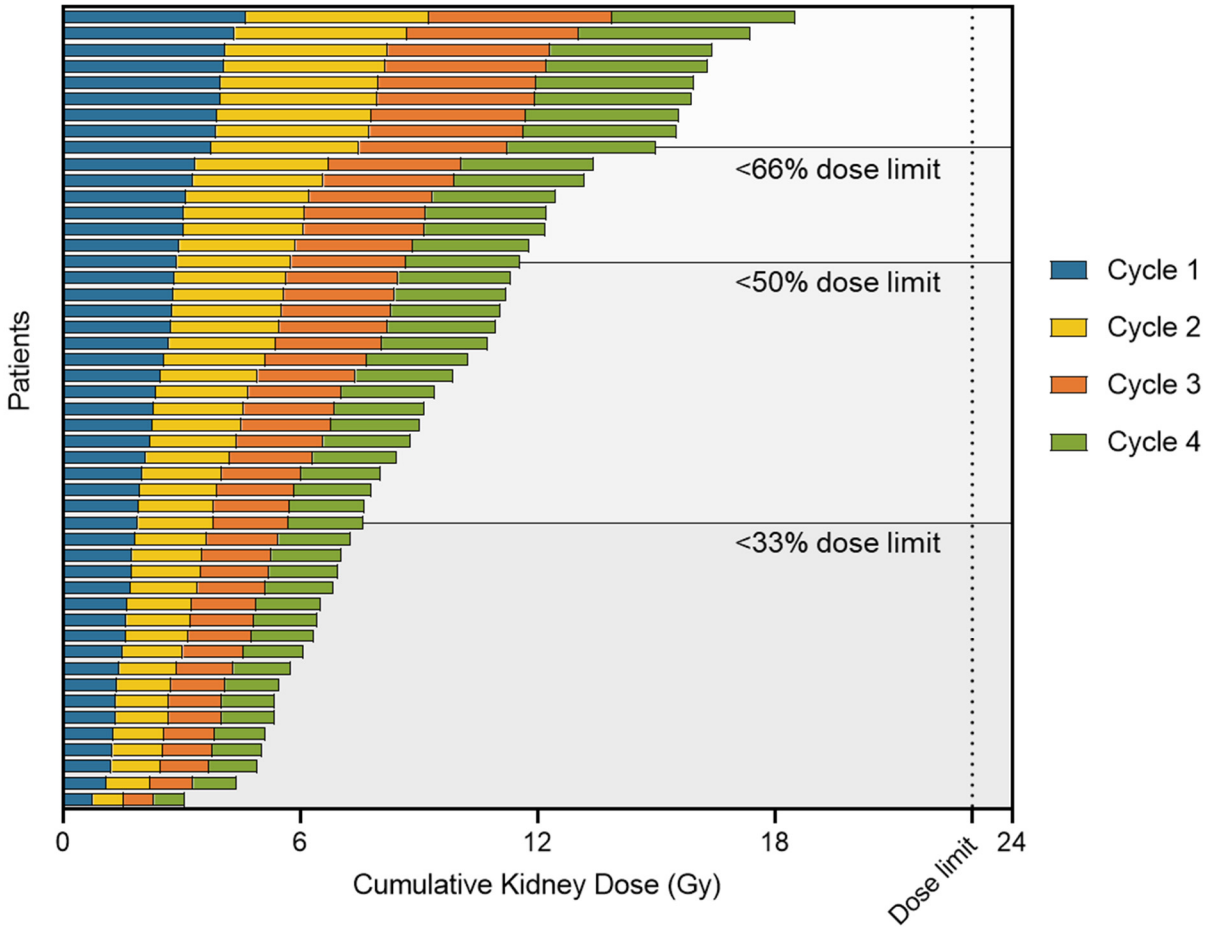


Figure 7.6. Theoretical cumulative kidney doses. Cumulative kidney doses are shown for 4 cycles assuming equal kidney dose and administered activity for all subsequent cycles.

Current literature on how normal organ doses differ between cycles is still sparse; however, one study found that there was no significant difference in kidney dose from $^{177}$Lu-PSMA-617 between the first two cycles (*34*). Even under the conservative

assumption that kidney doses may increase on subsequent treatment cycles (*171*), kidney doses are still significantly lower than accepted dose limits, suggesting a safe window in which activities could be augmented. While Figure 7.6 highlights a theoretical situation in which patients may be able to tolerate increased applied injected activities per cycle, it equally suggests a possibility to increase the number of cycles. Violet et al. also concluded that either higher treatment activities or additional cycles are both possible without compromising patient safety. Further work in a larger cohort is needed to better understand normal organ pharmacokinetics over multiple cycles and whether tumor-sink effects exist as the tumor burden changes over time.

One particular challenge of this study is that there are sources of uncertainty in internal emitter dosimetry that are inherent in the dose calculation process that propagate to the final dose result. One of the most significant contributing sources of uncertainty is the organ or tumor volume delineation itself (*58,142*). While both the kidney and tumor ROI creation is aided by computer segmentation tools, there are still significant manual adjustments made and thereby these regions are subject to inter-observer error. In addition, we could be biased towards selecting higher dose tumors due to the requirement that lesions must show quantifiable uptake on imaging at all time points.

An important limitation of this work is that the hybrid planar/SPECT imaging protocol used for this cohort is susceptible to overestimation of activity in comparison with SPECT-only imaging (though not as severely as with planar-only imaging) (*172-174*). This is particularly likely in abdominal regions with overlapping structures. For example, in many patients the gastrointestinal tract shows high uptake at later time points that needs to be purposefully excluded from kidney ROIs. This activity overlap is significantly

reduced by using the posterior planar views only for kidney dosimetry; however, in some patients it is not entirely avoidable and must be manually excluded. Overestimation of kidney absorbed dose should be minimized so as to not needlessly recommend in future a lower injected activity that in turn lowers the dose to tumor targets. It is however a strength in the dataset that the imaging protocol included a late imaging time point for which 9 patients returned 4-9 days after RNT initiation.

One attractive goal in dosimetry is to move away from organ and tumor-level doses towards voxel-level estimates of tissue absorbed dose (*175*). In reality, tumor tracer uptake is heterogeneous, in part due to varying vascularization and degree of PSMA expression (*176*). Consideration of heterogeneous uptake requires knowledge of 3D activity distributions, which can be obtained by SPECT imaging, but requires more complex computational models. Voxel-level dosimetry considers each voxel as an individual radiation source and all surrounding voxels as targets (*177*). The advantage of voxel-level dosimetry is the ability to process these inhomogeneous activity distributions. Monte Carlo simulations are the gold standard in radiation transport calculations and can also handle inhomogeneous activity distributions. There are multiple MC-based voxel dosimetry platforms available (*178,179*). However, one disadvantage of MC-based simulations is that they are difficult to implement clinically due to long computation times for millions of simulated particles (*180,181*). For future work, SPECT-only follow-up imaging for dosimetry is preferred to enable voxelized dosimetry and better understand radiation dose profiles deposited in tumors and surrounding healthy tissues.

## 7.5 Conclusion

This chapter is a preliminary analysis of the RESIST-PC phase 2 trial cohort of mCRPC patients treated with $^{177}$Lu-PSMA-617 to estimate kidney and tumor lesion absorbed doses. We used a hybrid imaging approach using one single quantitative SPECT/CT (+24h) and serial planar imaging (4h, 24h, 48h, 72h, ±4-9 days). The mean kidney dose for the first cycle was 0.35 ± 0.14 Gy/GBq and the mean tumor lesion dose was 3.22 ± 4.32 Gy/GBq. Assuming the median injected activity of 7.2 GBq, the per-cycle kidney dose would be 2.6 Gy and 23.2 Gy per metastatic lesion, with significant inter- and intra-patient variability in tumor doses.

# Chapter 8: Future outlook

## 8.1 Clinical alpha particle dosimetry

A version of this section has been accepted to be presented at the 2022 SNMMI Annual Meeting and is the basis for a brief communication in preparation: Meyer C, Allmann A, Allmann J, Eiber M, Czernin J, Dahlbom M, Calais J. Extrapolating organ and tumor doses for $^{225}$Ac-PSMA-I&T radionuclide therapy in patients with mCRPC. [Communication in preparation].

As interest in clinical implementation of TAT using actinium-225 as a therapeutic radionuclide is growing, this requires consideration of the radiation dose profile not only for patient safety, but also meaningful study design and regulatory approvals. Unlike for $^{177}$Lu, which decays with an imageable gamma emission, SPECT or imaging-based dosimetry for $^{225}$Ac radiopharmaceuticals is near impossible to calculate directly due to low injected activities and low gamma count statistics. One possible solution is to extrapolate $^{225}$Ac-PSMA dosimetry estimates from pre-existing estimates using a different isotope (i.e. from $^{177}$Lu-PSMA dosimetry). Previous clinical studies have described extrapolation methodologies using serial imaging from $^{68}$Ga and $^{177}$Lu extrapolated to the half-life of alpha-emitters such as $^{213}$Bi and $^{225}$Ac (*96,182*). One such pre-existing $^{177}$Lu-PSMA dosimetry dataset is for $^{177}$Lu-PSMA-I&T as described by Okamoto et al. As a first step, we have indirectly estimated organ and tumor doses for $^{225}$Ac-PSMA-I&T by extrapolating the kinetic activity data from this $^{177}$Lu-PSMA-I&T patient cohort.

Tumor and organ time-activity curves based on whole-body planar scintigraphy from 14 patients with mCRPC obtained after their first cycle of $^{177}$Lu-PSMA-I&T were extrapolated from the 6.7 day half-life of $^{177}$Lu to the 9.9 day half-life of $^{225}$Ac (*96,183*). Source organs included kidneys, liver, salivary glands (using counts from delineated bilateral parotid glands), body remainder, and tumor targets. All subsequent curve-fitting, integration, and dose calculation was performed using OLINDA/EXM v. 2.0 with the adult male phantom model for organs and the sphere model for tumor self-irradiated doses. Time activity curves with 3 time points were fit with mono-exponential functions, and bi-exponential functions were used to fit curves with at least 4 time points. Actinium doses were calculated assuming an injected activity of 8 MBq.

All daughter radionuclides of $^{225}$Ac were assumed to decay instantaneously with no translocation, and a relative biologic effectiveness (RBE) of 5 was assumed for alpha particles (*18,96*). According to current MIRD guidelines, an RBE of 5 for the alpha particles emitted by $^{225}$Ac is most appropriate for comparison to the beta radiation from $^{177}$Lu (*18*). This factor scales the effective dose to better compare the biologic effects of the different therapeutic isotopes. Furthermore, the extrapolation method requires the assumption that the isotope replacement has no effect on the biological retention of the tracer, and that the multiple daughters of $^{225}$Ac are instantly decaying at the site of the first disintegration (*96,182*). This assumption therefore neglects the possibility of recoiling daughters of $^{225}$Ac to cause off-target effects when not retained at the tumor site (*184*). It has however been shown that the rapid internalization of PSMA-617 and the generation of $^{225}$Ac daughters within the cells lead to high daughter retention, particularly for the shorter-lived daughters (*185*).

Individual lesion dose extrapolations for the 14 patients are shown in Figure 8.1. A total of 37 tumors were analyzed, yielding a mean overall dose of 27.6 ± 23.4 Gy, or 4.3 ± 2.6 Gy/GBq, with significant variation both within and between patients. This represents a net 27% increase in tumor dose for $^{225}$Ac over $^{177}$Lu estimates.

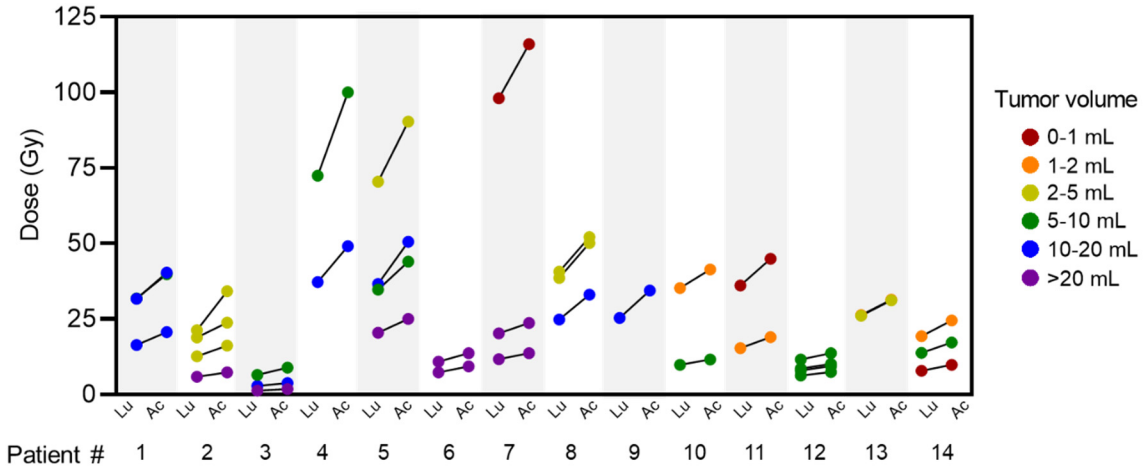


Figure 8.1 Tumor dose extrapolation from $^{177}$Lu-PSMA-I&T to $^{225}$Ac-PSMA-I&T in 14 patients. Actinium doses are calculated assuming an injected activity of 8 MBq.

The mean whole-body effective dose for $^{225}$Ac-PSMA-I&T was 37.1 mSv/MBq. Therefore, for an assumed administration of 8 MBq (0.22 mCi) $^{225}$Ac-PSMA-I&T, the whole-body effective dose is 0.30 Sv ± 0.18 Sv for a single cycle. Absorbed doses for each organ are presented in Table 8.1.

Table 8.1 Average equivalent organ absorbed doses for $^{225}$Ac-PSMA-I&T

| Target Organ | Equivalent Dose [mSv/MBq] | | Equivalent Dose for 8 MBq injection [Sv] | |
|---|---|---|---|---|
| | Ave | SD | Ave | SD |
| Adrenals | 3.06E+01 | 2.59E+01 | 2.45E-01 | 2.07E-01 |
| Brain | 3.01E+01 | 2.60E+01 | 2.41E-01 | 2.08E-01 |
| Esophagus | 3.01E+01 | 2.60E+01 | 2.41E-01 | 2.08E-01 |
| Eyes | 3.01E+01 | 2.60E+01 | 2.41E-01 | 2.08E-01 |
| Gallbladder Wall | 3.03E+01 | 2.60E+01 | 2.42E-01 | 2.08E-01 |
| Left colon | 3.02E+01 | 2.60E+01 | 2.41E-01 | 2.08E-01 |
| Small Intestine | 3.02E+01 | 2.60E+01 | 2.41E-01 | 2.08E-01 |
| Stomach Wall | 3.02E+01 | 2.60E+01 | 2.41E-01 | 2.08E-01 |
| Right colon | 3.02E+01 | 2.60E+01 | 2.41E-01 | 2.08E-01 |
| Rectum | 3.02E+01 | 2.60E+01 | 2.41E-01 | 2.08E-01 |
| Heart Wall | 3.02E+01 | 2.60E+01 | 2.41E-01 | 2.08E-01 |
| Kidneys | 6.14E+02 | 2.49E+02 | 4.91E+00 | 2.00E+00 |
| Liver | 6.80E+01 | 4.25E+01 | 5.44E-01 | 3.40E-01 |
| Lungs | 3.01E+01 | 2.60E+01 | 2.41E-01 | 2.08E-01 |
| Pancreas | 3.02E+01 | 2.60E+01 | 2.42E-01 | 2.08E-01 |
| Prostate | 3.02E+01 | 2.60E+01 | 2.41E-01 | 2.08E-01 |
| Salivary Glands | 2.31E+02 | 9.95E+01 | 1.85E+00 | 7.96E-01 |
| Red Marrow | 4.40E+01 | 3.80E+01 | 3.52E-01 | 3.04E-01 |
| Osteogenic Cells | 3.00E+02 | 2.60E+02 | 2.40E+00 | 2.08E+00 |
| Spleen | 3.02E+01 | 2.60E+01 | 2.42E-01 | 2.08E-01 |
| Testes | 3.01E+01 | 2.60E+01 | 2.41E-01 | 2.08E-01 |
| Thymus | 3.01E+01 | 2.60E+01 | 2.41E-01 | 2.08E-01 |
| Thyroid | 3.01E+01 | 2.60E+01 | 2.41E-01 | 2.08E-01 |
| Urinary Bladder Wall | 3.01E+01 | 2.60E+01 | 2.41E-01 | 2.08E-01 |
| Total Body | 3.47E+01 | 2.61E+01 | 2.77E-01 | 2.09E-01 |
| Whole-body effective dose | 3.71E+01 | 2.27E+01 | 2.97E-01 | 1.81E-01 |

The highest equivalent dose, assuming an RBE of 5, is observed in the kidneys (4.91 Sv), followed by osteogenic cells (2.4 Sv), salivary glands (1.85 Sv), and liver (0.54 Sv). For a potential total of 4 cycles of $^{225}$Ac-PSMA-I&T, the estimated cumulative kidney dose is 19.6 Sv, followed by 9.6 Sv in osteogenic cells, 7.4 Sv in salivary glands, and 2.2 Sv in the liver. Individual patient dosimetry extrapolations for kidneys and salivary glands are shown in Figure 8.2

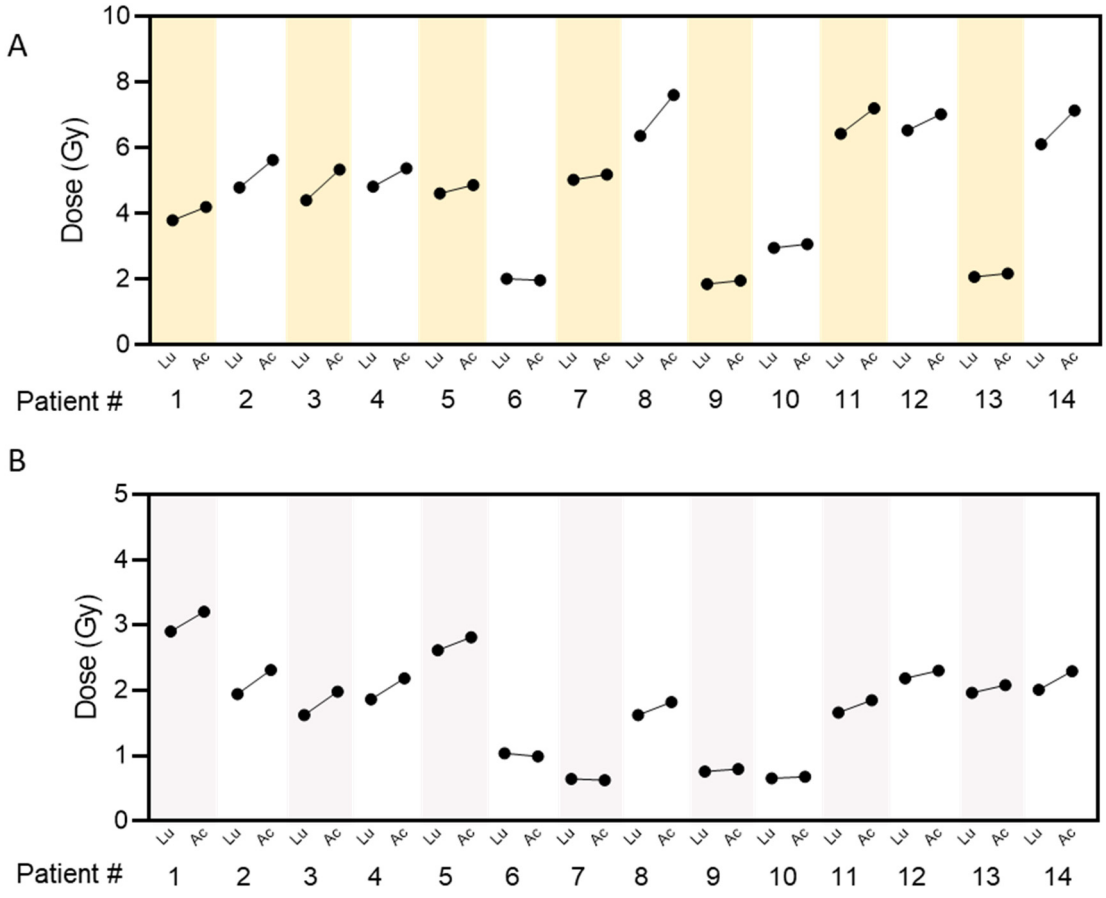


Figure 8.2 $^{225}$Ac-PSMA-I&T dose extrapolation for kidneys and salivary glands, assuming an injected activity of 8 MBq. Values shown for kidneys (A) and salivary glands (B).

Growing interest in the widespread application of $^{225}$Ac-based radiopharmaceuticals necessitates a better understanding of the dosimetry profile. This section described our early experience extrapolating $^{225}$Ac-PSMA-I&T doses based on existing $^{177}$Lu dosimetry data in patients with mCRPC. Given the imaging limitations of $^{225}$Ac that prevent reliable direct measurement of accumulated activities over time, alternative approaches to dosimetry estimates will be an important area of future research and validation.

### 8.2 Single time point dosimetry

One practical challenge that precludes implementation of clinical dosimetry is the logistical need for multiple time point imaging. Current best practices advise a minimum of three imaging time points following administration, with a later time point suggested for more accurate curve-fitting of the tracer washout phase (*175,186*). This can be difficult for both the clinical department to schedule imaging time, as well as from a patient perspective who may not be able to travel and return for multiple follow-up imaging scans. Therefore, dosimetry based on a single quantitative image would be logistically desirable. This concept has been theoretically examined for $^{177}$Lu-PSMA-617 as well as $^{177}$Lu-DOTATATE treatments in neuroendocrine tumor patients (*168,187*). However, it remains an unmet clinical need to assess whether dosimetry based on a single time point of imaging can adequately recapitulate dose estimations as compared with conventional multi-time point dosimetry for PSMA-targeted RNT (*187,188*).

One possible approach is to use a multiple time point imaging dataset, such as the one used for our dosimetry study in Chapter 7, and reproduce the calculated dose using only the SPECT acquisition 24 hours after treatment. The complete serial planar and SPECT images can first be used to determine a population-based average clearance time from each organ of interest and the tumors. The fixed clearance kinetics will then be applied to the $^{177}$Lu counts in the single SPECT and used to generate pseudo activity data points over time for input into OLINDA/EXM. A schematic of this suggested workflow is presented in Figure 8.3. The predicted dose using a single quantitative SPECT and population clearance kinetics can then be directly compared against the dose using patient-specific kinetics from real multi-time point imaging. The degree of dose estimation agreement between methods can then be assessed to quantify the relative differences between the two quantitative measurements. This potential future work may help to answer whether a single quantitative 3D image might be sufficient for dose calculation in these patients, and ultimately streamline clinical implementation of dosimetry.

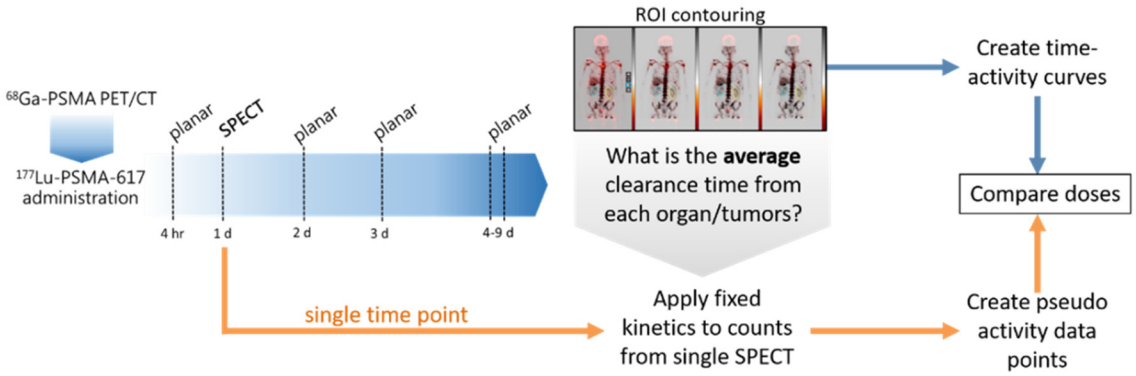


Figure 8.3 Hypothetical dosimetry workflow for single time point dosimetry based on hybrid SPECT/planar imaging. Time-activity curves are generated either from multiple imaging time points (blue) or from a single SPECT image (orange) and compared.

### 8.3 Correlation of absorbed doses and treatment response outcomes

Furthermore, there is increasing interest in investigating whether absorbed doses in RNT actually correlate with efficacy and toxicity. One study of a $^{177}$Lu-PSMA-617 treatment cohort started to investigate this question and found that patients who experienced a PSA decline >50% achieved significantly higher tumor doses (*36*). This study utilized an in-house software program for the conversion of voxel-based activities to doses (*189*). While this is a promising early finding, other available studies are still limited and heterogeneous.

Perhaps the most straightforward way to start answering this question is with already existing data. Prior to treatment with radiopharmaceuticals, each patient undergoes a screening PSMA PET/CT scan, from which we can already seek to identify if there are patterns between pre-therapeutic patient features (SUV metrics, tumor volume) and treatment response (absorbed doses, follow-up PSA). Other potentially relevant features could be baseline PSA levels, clinical stage, and $^{177}$Lu SPECT imaging features. Dosimetry data can be used for multivariate correlation analyses, including for example between tumor volumes and normal organ absorbed doses to help investigate the tumor-sink effect as a rationale for more personalized dosimetry.

Another more computational approach that may play a role in dosimetry and treatment planning of PSMA RNT is machine learning. Supervised machine learning algorithms may have a role in aiding the prediction of $^{177}$Lu-PSMA-617 patient doses. The basic premise of supervised machine learning is to use an algorithm to discover relationships between input variables, like imaging features, and a given output (*190,191*).

The output in this case is a continuous value: the tissue-absorbed doses in organs or tumors. The algorithm learns a mapping function from example inputs and associated outputs from a training dataset and parses through the training dataset, iteratively updating the mapping regression function. The goal is to learn a mapping function sufficiently well that it can predict the outcome (dose) based on the input features (*192*). With this type of work, dose predictions from the test set can be compared to the ground-truth doses calculated separately to evaluate the accuracy of the model. A similar approach may be possible to investigate whether absorbed doses are meaningful in the prediction of patient outcomes such as biochemical response and survival.

Despite growing evidence that absorbed doses in RNT correlate with efficacy and toxicity (*36,58*), dosimetry is still rarely performed. Ultimately, working towards a better understanding of the absorbed doses and their associated effects will help the field of nuclear medicine move towards more precise and patient-specific treatments. This potential future work would help discover dose-response relationships to aid in treatment planning for more individualized management of metastatic prostate cancer. Also, machine learning may play a relevant role in the future towards automated dose prediction, and ultimately the integration of dosimetry calculations in treatment planning.

# Chapter 9: Conclusions

Recalling the specific aims of this dissertation, the overall objective was to investigate differences between $^{177}$Lu and $^{225}$Ac in PSMA RNT, as well as to evaluate the clinical dosimetry of imaging and therapy theranostic agents. The following chapter summaries provide an overview of the research findings of this dissertation addressing these goals.

Chapter 2 describes the development of a translatable mouse model of disseminated prostate cancer achieved by intracardiac inoculation of cell lines. We then compared efficacy of targeted alpha PSMA therapy in this model; leveraging PET imaging, bioluminescence, and immunohistochemistry to evaluate treatment outcomes in this model at various stages of disease. This work revealed superior efficacy at earlier intervention times and suggested potential benefits for treating minimal residual disease before detectable by PET/CT.

In Chapter 3, we sought to directly compare alpha versus beta particle PSMA RNT, as well as a combination thereof, in a mouse model of prostate cancer. Simultaneous dual isotope or, “tandem”, approaches may provide the benefits of using both $^{177}$Lu and $^{225}$Ac to improve treatment tolerability while retaining high tumor dose. In this study, we first determined injected activities of $^{177}$Lu and $^{225}$Ac that yield equivalent tumor doses. Then, mice bearing disseminated prostate cancer lesions were treated at two different stages of disease with $^{177}$Lu- and $^{225}$Ac-PSMA-617 as single agents, or in combination. Treatment with $^{177}$Lu alone was ineffective against micrometastatic disease, while the

most significant tumor growth retardation and survival benefits were observed with the single agent $^{225}$Ac and tandem approaches.

Chapter 4 describes our evaluation of PSMA-TO-1, a novel PSMA ligand with longer circulation time than existing PSMA-targeting compounds. We conducted preclinical comparisons of PET tracer uptake, long-term biodistribution using $^{177}$Lu, and a treatment study using $^{225}$Ac in our metastatic prostate cancer model. Overall, higher tumor uptake was observed with PSMA-TO-1 compared with PSMA-617; however, this was accompanied by higher uptake in normal organs, most notably the kidneys which can be dose-limiting organs in the clinical setting. Our preclinical treatment studies demonstrated a significant survival benefit with $^{225}$Ac-PSMA-TO-1 over $^{225}$Ac-PSMA-617.

Chapter 5 addresses the radiation dosimetry of $^{68}$Ga-FAPI-46, a novel theranostic agent targeting cancer-associated fibroblasts in the tumor microenvironment with potential application in prostate cancer. This chapter describes the calculation of the radiation dose from a diagnostic $^{68}$Ga-FAPI-46 PET scan using clinical imaging data from a variety of cancers. $^{68}$Ga-FAPI-46 was shown to have a favorable dosimetry profile for imaging, with increasing tumor-to-background ratios over time. This work was used to establish radiation safety for multiple ongoing clinical trials investigating the biodistribution of this tracer across different malignancies, including prostate cancer.

In Chapter 6, we calculated the radiation dosimetry profile and biodistribution of a $^{99m}$Tc-labeled PSMA-targeting agent in humans. $^{99m}$Tc-PSMA-I&S biodistribution and dosimetry was assessed in healthy volunteers using a “hybrid” imaging method (sequential gamma planar imaging and one single SPECT/CT). Effective doses were

deemed safe and comparable to other $^{99m}$Tc-labeled PSMA inhibitors. This work was used to initiate a clinical trial at UCLA for radioguided surgery to investigate intra-operative detection of lymph node metastases in prostate cancer patients for the first time in the United States.

Chapter 7 addresses patient-specific dosimetry calculations in the therapeutic setting. To date, there are few published studies of patient-specific tumor doses in PSMA RNT. This chapter is a preliminary analysis of a phase 2 trial cohort of mCRPC patients treated with $^{177}$Lu-PSMA-617 to estimate kidney and tumor lesion absorbed doses using a hybrid imaging approach. This retrospective analysis includes absorbed kidney doses in 49 patients, and 280 segmented metastatic lesions. Kidney doses were regarded to be safe. We observed significant inter- and intra-patient variability in tumor doses, with a mean 10-fold increase in tumor doses compared to kidneys. This is an ongoing study as more patients are included the retrospective analysis.

Finally, Chapter 8 discusses opportunities for further research in PSMA RNT, including dosimetry for alpha particle emitters, single time point dosimetry, and investigation of dose as a predictor of response. This chapter includes our results of an early study to extrapolate doses for an $^{225}$Ac-labeled PSMA inhibitor from existing $^{177}$Lu dosimetry.

Throughout this dissertation, the common thread among these studies is the application of dosimetry to further our understanding of RNT. These works utilize dosimetry along the translational spectrum from preclinical biodistribution studies in mice to clinical analyses of patients treated with RNT. By using these dosimetric approaches,

we have successfully shown the utility of dosimetry to provide a quantitative measure for the comparison, characterization, and evaluation of theranostic agents along the translational research pipeline. Thereby, these studies support an integral role for dosimetry in the pursuit of theranostics and more personalized management of metastatic prostate cancer.

# References


**1.** Gomes Marin JF, Nunes RF, Coutinho AM, et al. Theranostics in Nuclear Medicine: Emerging and Re-emerging Integrated Imaging and Therapies in the Era of Precision Oncology. *RadioGraphics.* 2020;40:1715-1740.

**2.** Solnes LB, Werner RA, Jones KM, et al. Theranostics: Leveraging Molecular Imaging and Therapy to Impact Patient Management and Secure the Future of Nuclear Medicine. *J Nucl Med.* 2020;61:311-318.

**3.** Sgouros G, Bodei L, McDevitt MR, Nedrow JR. Radiopharmaceutical therapy in cancer: clinical advances and challenges. *Nat Rev Drug Discov.* 2020;19:589-608.

**4.** O'Keefe DS, Su SL, Bacich DJ, et al. Mapping, genomic organization and promoter analysis of the human prostate-specific membrane antigen gene. *Biochimica et Biophysica Acta (BBA) - Gene Structure and Expression.* 1998;1443:113-127.

**5.** Mannweiler S, Amersdorfer P, Trajanoski S, Terrett JA, King D, Mehes G. Heterogeneity of prostate-specific membrane antigen (PSMA) expression in prostate carcinoma with distant metastasis. *Pathol Oncol Res.* 2009;15:167-172.

**6.** Jones W, Griffiths K, Barata PC, Paller CJ. PSMA Theranostics: Review of the Current Status of PSMA-Targeted Imaging and Radioligand Therapy. *Cancers.* 2020;12:1367.

**7.** Mhawech-Fauceglia P, Zhang S, Terracciano L, et al. Prostate-specific membrane antigen (PSMA) protein expression in normal and neoplastic tissues and its sensitivity and specificity in prostate adenocarcinoma: an immunohistochemical study using mutiple tumour tissue microarray technique. *Histopathology.* 2007;50:472-483.

**8.** Silver DA, Pellicer I, Fair WR, Heston WD, Cordon-Cardo C. Prostate-specific membrane antigen expression in normal and malignant human tissues. *Clin Cancer Res.* 1997;3:81-85.

**9.** Sweat SD, Pacelli A, Murphy GP, Bostwick DG. Prostate-specific membrane antigen expression is greatest in prostate adenocarcinoma and lymph node metastases. *Urology.* 1998;52:637-640.

**10.** Bostwick DG, Pacelli A, Blute M, Roche P, Murphy GP. Prostate specific membrane antigen expression in prostatic intraepithelial neoplasia and adenocarcinoma: a study of 184 cases. *Cancer.* 1998;82:2256-2261.

**11.** Kawakami M, Nakayama J. Enhanced expression of prostate-specific membrane antigen gene in prostate cancer as revealed by in situ hybridization. *Cancer Res.* 1997;57:2321-2324.

**12.** Rahbar K, Afshar-Oromieh A, Jadvar H, Ahmadzadehfar H. PSMA Theranostics: Current Status and Future Directions. *Molecular imaging.* 2018;17:1536012118776068-1536012118776068.

**13.** Vallabhajosula S, Kuji I, Hamacher KA, et al. Pharmacokinetics and biodistribution of 111In- and 177Lu-labeled J591 antibody specific for prostate-specific membrane antigen: prediction of 90Y-J591 radiation dosimetry based on 111In or 177Lu? *J Nucl Med.* 2005;46:634-641.

**14.** Rosenthal SA, Haseman MK, Polascik TJ. Utility of capromab pendetide (ProstaScint) imaging in the management of prostate cancer. *Tech Urol.* 2001;7:27-37.

**15.** Imai K, Takaoka A. Comparing antibody and small-molecule therapies for cancer. *Nat Rev Cancer.* 2006;6:714-727.

**16.** Afshar-Oromieh A, Hetzheim H, Kratochwil C, et al. The Theranostic PSMA Ligand PSMA-617 in the Diagnosis of Prostate Cancer by PET/CT: Biodistribution in Humans, Radiation Dosimetry, and First Evaluation of Tumor Lesions. *Journal of Nuclear Medicine.* 2015;56:1697.

**17.** Wong FC. MIRD: Radionuclide Data and Decay Schemes. *Journal of Nuclear Medicine.* 2009;50:2091.

**18.** Sgouros G, Roeske JC, McDevitt MR, et al. MIRD Pamphlet No. 22 (abridged): radiobiology and dosimetry of alpha-particle emitters for targeted radionuclide therapy. *J Nucl Med.* 2010;51:311-328.

**19.** Mulford DA, Scheinberg DA, Jurcic JG. The promise of targeted α-particle therapy. *Journal of Nuclear Medicine.* 2005;46:199S-204S.

**20.** National Nuclear Data Center [Internet]. https://www.nndc.bnl.gov/.

**21.** Miederer M, Scheinberg DA, McDevitt MR. Realizing the potential of the Actinium-225 radionuclide generator in targeted alpha particle therapy applications. *Adv Drug Deliv Rev.* 2008;60:1371-1382.

**22.** Scheinberg DA, McDevitt MR. Actinium-225 in targeted alpha-particle therapeutic applications. *Curr Radiopharm.* 2011;4:306-320.

**23.** McDevitt MR, Scheinberg DA. Ac-225 and her daughters: the many faces of Shiva. *Cell Death & Differentiation.* 2002;9:593-594.

**24.** Awang ZH, Essler M, Ahmadzadehfar H. Radioligand therapy of metastatic castration-resistant prostate cancer: current approaches. *Radiation oncology (London, England).* 2018;13:98-98.

**25.** Rahbar K, Bode A, Weckesser M, et al. Radioligand Therapy With 177Lu-PSMA-617 as A Novel Therapeutic Option in Patients With Metastatic Castration Resistant Prostate Cancer. *Clin Nucl Med.* 2016;41:522-528.

**26.** Kratochwil C, Giesel FL, Stefanova M, et al. PSMA-Targeted Radionuclide Therapy of Metastatic Castration-Resistant Prostate Cancer with 177Lu-Labeled PSMA-617. *J Nucl Med.* 2016;57:1170-1176.

**27.** Rahbar K, Ahmadzadehfar H, Kratochwil C, et al. German Multicenter Study Investigating 177Lu-PSMA-617 Radioligand Therapy in Advanced Prostate Cancer Patients. *J Nucl Med.* 2017;58:85-90.

**28.** Ahmadzadehfar H, Eppard E, Kürpig S, et al. Therapeutic response and side effects of repeated radioligand therapy with 177Lu-PSMA-DKFZ-617 of castrate-resistant metastatic prostate cancer. *Oncotarget.* 2016;7:12477-12488.

**29.** Hofman MS, Violet J, Hicks RJ, et al. [(177)Lu]-PSMA-617 radionuclide treatment in patients with metastatic castration-resistant prostate cancer (LuPSMA trial): a single-centre, single-arm, phase 2 study. *Lancet Oncol.* 2018;19:825-833.

**30.** Fendler WP, Reinhardt S, Ilhan H, et al. Preliminary experience with dosimetry, response and patient reported outcome after 177Lu-PSMA-617 therapy for metastatic castration-resistant prostate cancer. *Oncotarget.* 2017;8:3581-3590.

**31.** Fendler WP, Rahbar K, Herrmann K, Kratochwil C, Eiber M. (177)Lu-PSMA Radioligand Therapy for Prostate Cancer. *J Nucl Med.* 2017;58:1196-1200.

**32.** Emmett L, Willowson K, Violet J, Shin J, Blanksby A, Lee J. Lutetium (177) PSMA radionuclide therapy for men with prostate cancer: a review of the current literature and discussion of practical aspects of therapy. *J Med Radiat Sci.* 2017;64:52-60.

**33.** Haberkorn U, Giesel F, Morgenstern A, Kratochwil C. The future of radioligand therapy: α, β, or both? *Journal of Nuclear Medicine.* 2017;58:1017-1018.

**34.** Delker A, Fendler WP, Kratochwil C, et al. Dosimetry for (177)Lu-DKFZ-PSMA-617: a new radiopharmaceutical for the treatment of metastatic prostate cancer. *Eur J Nucl Med Mol Imaging.* 2016;43:42-51.

**35.** Kabasakal L, AbuQbeitah M, Aygün A, et al. Pre-therapeutic dosimetry of normal organs and tissues of (177)Lu-PSMA-617 prostate-specific membrane antigen (PSMA) inhibitor in patients with castration-resistant prostate cancer. *Eur J Nucl Med Mol Imaging.* 2015;42:1976-1983.

**36.** Violet J, Jackson P, Ferdinandus J, et al. Dosimetry of (177)Lu-PSMA-617 in Metastatic Castration-Resistant Prostate Cancer: Correlations Between Pretherapeutic Imaging and Whole-Body Tumor Dosimetry with Treatment Outcomes. *J Nucl Med.* 2019;60:517-523.

**37.** Sathekge M, Bruchertseifer F, Knoesen O, et al. 225Ac-PSMA-617 in chemotherapy-naive patients with advanced prostate cancer: a pilot study. *European Journal of Nuclear Medicine and Molecular Imaging.* 2019;46:129-138.

**38.** Yadav MP, Ballal S, Sahoo RK, Tripathi M, Seth A, Bal C. Efficacy and safety of (225)Ac-PSMA-617 targeted alpha therapy in metastatic castration-resistant Prostate Cancer patients. *Theranostics.* 2020;10:9364-9377.

**39.** Kratochwil C, Bruchertseifer F, Rathke H, et al. Targeted alpha-Therapy of Metastatic Castration-Resistant Prostate Cancer with (225)Ac-PSMA-617: Swimmer-Plot Analysis Suggests Efficacy Regarding Duration of Tumor Control. *J Nucl Med.* 2018;59:795-802.

**40.** Kojima S, Cuttler JM, Shimura N, Koga H, Murata A, Kawashima A. Present and Future Prospects of Radiation Therapy Using α-Emitting Nuclides. *Dose Response.* 2018;16:1559325817747387.

**41.** Morgenstern A, Apostolidis C, Kratochwil C, Sathekge M, Krolicki L, Bruchertseifer F. An Overview of Targeted Alpha Therapy with (225)Actinium and (213)Bismuth. *Curr Radiopharm.* 2018;11:200-208.

**42.** Chakravarty R, Siamof CM, Dash A, Cai W. Targeted α-therapy of prostate cancer using radiolabeled PSMA inhibitors: a game changer in nuclear medicine. *Am J Nucl Med Mol Imaging.* 2018;8:247-267.

**43.** van der Doelen MJ, Mehra N, van Oort IM, et al. Clinical outcomes and molecular profiling of advanced metastatic castration-resistant prostate cancer patients treated with 225Ac-PSMA-617 targeted alpha-radiation therapy. *Urologic Oncology: Seminars and Original Investigations.* 2021;39:729.e727-729.e716.

**44.** Heynickx N, Herrmann K, Vermeulen K, Baatout S, Aerts A. The salivary glands as a dose limiting organ of PSMA- targeted radionuclide therapy: A review of the lessons learnt so far. *Nuclear Medicine and Biology.* 2021;98-99:30-39.

**45.** Rupp NJ, Umbricht CA, Pizzuto DA, et al. First Clinicopathologic Evidence of a Non-PSMA-Related Uptake Mechanism for (68)Ga-PSMA-11 in Salivary Glands. *J Nucl Med.* 2019;60:1270-1276.

**46.** Tönnesmann R, Meyer PT, Eder M, Baranski A-C. [(177)Lu]Lu-PSMA-617 Salivary Gland Uptake Characterized by Quantitative In Vitro Autoradiography. *Pharmaceuticals (Basel, Switzerland).* 2019;12:18.

**47.** Roy J, Warner BM, Basuli F, et al. Comparison of Prostate-Specific Membrane Antigen Expression Levels in Human Salivary Glands to Non-Human Primates and Rodents. *Cancer biotherapy & radiopharmaceuticals.* 2020;35:284-291.

**48.** Taieb D, Foletti JM, Bardies M, Rocchi P, Hicks RJ, Haberkorn U. PSMA-Targeted Radionuclide Therapy and Salivary Gland Toxicity: Why Does It Matter? *J Nucl Med.* 2018;59:747-748.

**49.** Feuerecker B, Tauber R, Knorr K, et al. Activity and Adverse Events of Actinium-225-PSMA-617 in Advanced Metastatic Castration-resistant Prostate Cancer After Failure of Lutetium-177-PSMA. *Eur Urol.* 2021;79:343-350.

**50.** Khreish F, Ebert N, Ries M, et al. (225)Ac-PSMA-617/(177)Lu-PSMA-617 tandem therapy of metastatic castration-resistant prostate cancer: pilot experience. *Eur J Nucl Med Mol Imaging.* 2019.

**51.** Scher HI, Morris MJ, Stadler WM, et al. Trial Design and Objectives for Castration-Resistant Prostate Cancer: Updated Recommendations From the Prostate Cancer Clinical Trials Working Group 3. *J Clin Oncol.* 2016;34:1402-1418.

**52.** Chan TG, O'Neill E, Habjan C, Cornelissen B. Combination Strategies to Improve Targeted Radionuclide Therapy. *Journal of Nuclear Medicine.* 2020;61:1544-1552.

**53.** Scott A, Bodei L. Pharmacogenomics in Radionuclide Therapy: Impact on Response to Theranostics. *Journal of Nuclear Medicine.* 2020:jnumed.120.254995.

**54.** Czernin J, Current K, Mona CE, et al. Immune-Checkpoint Blockade Enhances (225)Ac-PSMA617 Efficacy in a Mouse Model of Prostate Cancer. *J Nucl Med.* 2021;62:228-231.

**55.** Current K, Meyer C, Magyar CE, et al. Investigating PSMA-Targeted Radioligand Therapy Efficacy as a Function of Cellular PSMA Levels and Intratumoral PSMA Heterogeneity. *Clin Cancer Res.* 2020;26:2946-2955.

**56.** Stuparu AD, Capri JR, Meyer C, et al. Mechanisms of Resistance to Prostate-Specific Membrane Antigen-Targeted Radioligand Therapy in a Mouse Model of Prostate Cancer. *J Nucl Med.* 2020.

**57.** Flux GD, Sjogreen Gleisner K, Chiesa C, et al. From fixed activities to personalized treatments in radionuclide therapy: lost in translation? *Eur J Nucl Med Mol Imaging.* 2018;45:152-154.

**58.** Lassmann M, Eberlein U. The Relevance of Dosimetry in Precision Medicine. *J Nucl Med.* 2018;59:1494-1499.

**59.** Chiesa C, Sjogreen Gleisner K, Flux G, et al. The conflict between treatment optimization and registration of radiopharmaceuticals with fixed activity posology in oncological nuclear medicine therapy. *Eur J Nucl Med Mol Imaging.* 2017;44:1783-1786.

**60.** Council Directive 2013/59/Euratom of 5 December 2013 laying down basic safety standards for protection against the dangers arising from exposure to ionising radiation, and repealing Directives 89/618/Euratom, 90/641/Euratom, 96/29/Euratom, 97/43/Euratom and 2003/122/Euratom

OJ L 13, 17.11.2014, p. 2011–2073.

**61.** Beauregard JM, Hofman MS, Kong G, Hicks RJ. The tumour sink effect on the biodistribution of 68Ga-DOTA-octreotate: implications for peptide receptor radionuclide therapy. *Eur J Nucl Med Mol Imaging.* 2012;39:50-56.

**62.** Gaertner FC, Halabi K, Ahmadzadehfar H, et al. Uptake of PSMA-ligands in normal tissues is dependent on tumor load in patients with prostate cancer. *Oncotarget.* 2017;8:55094-55103.

**63.** Fendler WP, Stuparu AD, Evans-Axelsson S, et al. Establishing (177)Lu-PSMA-617 Radioligand Therapy in a Syngeneic Model of Murine Prostate Cancer. *J Nucl Med.* 2017;58:1786-1792.

**64.** Zhang Y, Toneri M, Ma H, et al. Real-Time GFP Intravital Imaging of the Differences in Cellular and Angiogenic Behavior of Subcutaneous and Orthotopic Nude-Mouse Models of Human PC-3 Prostate Cancer. *Journal of Cellular Biochemistry.* 2016;117:2546-2551.

**65.** Wu X, Gong S, Roy-Burman P, Lee P, Culig Z. Current mouse and cell models in prostate cancer research. *Endocr Relat Cancer.* 2013;20:R155-170.

**66.** Stephenson RA, Dinney CP, Gohji K, Ordonez NG, Killion JJ, Fidler IJ. Metastatic model for human prostate cancer using orthotopic implantation in nude mice. *J Natl Cancer Inst.* 1992;84:951-957.

**67.** Rembrink K, Romijn JC, van der Kwast TH, Rubben H, Schroder FH. Orthotopic implantation of human prostate cancer cell lines: a clinically relevant animal model for metastatic prostate cancer. *Prostate.* 1997;31:168-174.

**68.** Bibby MC. Orthotopic models of cancer for preclinical drug evaluation: advantages and disadvantages. *Eur J Cancer.* 2004;40:852-857.

**69.** Wu TT, Sikes RA, Cui Q, et al. Establishing human prostate cancer cell xenografts in bone: induction of osteoblastic reaction by prostate-specific antigen-producing tumors in athymic and SCID/bg mice using LNCaP and lineage-derived metastatic sublines. *Int J Cancer.* 1998;77:887-894.

**70.** Pienta KJ, Abate-Shen C, Agus DB, et al. The current state of preclinical prostate cancer animal models. *Prostate.* 2008;68:629-639.

**71.** Kiess AP, Minn I, Vaidyanathan G, et al. (2S)-2-(3-(1-Carboxy-5-(4-211At-Astatobenzamido)Pentyl)Ureido)-Pentanedioic Acid for PSMA-Targeted α-Particle Radiopharmaceutical Therapy. *J Nucl Med.* 2016;57:1569-1575.

**72.** Corroyer-Dulmont A, Valable S, Falzone N, et al. VCAM-1 targeted alpha-particle therapy for early brain metastases. *Neuro-Oncology.* 2020;22:357-368.

**73.** Persson M, Juhl K, Rasmussen P, et al. uPAR targeted radionuclide therapy with (177)Lu-DOTA-AE105 inhibits dissemination of metastatic prostate cancer. *Mol Pharm.* 2014;11:2796-2806.

**74.** Wu X, Gong S, Roy-Burman P, Lee P, Culig Z. Current mouse and cell models in prostate cancer research. *Endocrine-related cancer.* 2013;20:R155-R170.

**75.** Simmons JK, Hildreth BE, 3rd, Supsavhad W, et al. Animal Models of Bone Metastasis. *Vet Pathol.* 2015;52:827-841.

**76.** Kaighn ME, Narayan KS, Ohnuki Y, Lechner JF, Jones LW. Establishment and characterization of a human prostatic carcinoma cell line (PC-3). *Invest Urol.* 1979;17:16-23.

**77.** Wu HC, Hsieh JT, Gleave ME, Brown NM, Pathak S, Chung LW. Derivation of androgen-independent human LNCaP prostatic cancer cell sublines: role of bone stromal cells. *Int J Cancer.* 1994;57:406-412.

**78.** van Bokhoven A, Varella-Garcia M, Korch C, et al. Molecular characterization of human prostate carcinoma cell lines. *Prostate.* 2003;57:205-225.

**79.** Lückerath K, Wei L, Fendler WP, et al. Preclinical evaluation of PSMA expression in response to androgen receptor blockade for theranostics in prostate cancer. *EJNMMI Res.* 2018;8:96.

**80.** Lin DL, Tarnowski CP, Zhang J, et al. Bone metastatic LNCaP-derivative C4-2B prostate cancer cell line mineralizes in vitro. *Prostate.* 2001;47:212-221.

**81.** Spans L, Helsen C, Clinckemalie L, et al. Comparative genomic and transcriptomic analyses of LNCaP and C4-2B prostate cancer cell lines. *PLoS One.* 2014;9:e90002.

**82.** Yamamichi F, Matsuoka T, Shigemura K, Kawabata M, Shirakawa T, Fujisawa M. Potential establishment of lung metastatic xenograft model of androgen receptor-positive and androgen-independent prostate cancer (C4-2B). *Urology.* 2012;80:951.e951-957.

**83.** Sramkoski RM, Pretlow TG, 2nd, Giaconia JM, et al. A new human prostate carcinoma cell line, 22Rv1. *In Vitro Cell Dev Biol Anim.* 1999;35:403-409.

**84.** Attardi BJ, Burgenson J, Hild SA, Reel JR. Steroid hormonal regulation of growth, prostate specific antigen secretion, and transcription mediated by the mutated androgen receptor in CWR22Rv1 human prostate carcinoma cells. *Mol Cell Endocrinol.* 2004;222:121-132.

**85.** Ullman-Culleré MH, Foltz CJ. Body condition scoring: a rapid and accurate method for assessing health status in mice. *Lab Anim Sci.* 1999;49:319-323.

**86.** Campbell JP, Merkel AR, Masood-Campbell SK, Elefteriou F, Sterling JA. Models of bone metastasis. *J Vis Exp.* 2012:e4260.

**87.** McDevitt MR, Thorek DLJ, Hashimoto T, et al. Feed-forward alpha particle radiotherapy ablates androgen receptor-addicted prostate cancer. *Nature Communications.* 2018;9:1629.

**88.** Barber TW, Singh A, Kulkarni HR, Niepsch K, Billah B, Baum RP. Clinical Outcomes of (177)Lu-PSMA Radioligand Therapy in Earlier and Later Phases of Metastatic Castration-Resistant Prostate Cancer Grouped by Previous Taxane Chemotherapy. *J Nucl Med.* 2019;60:955-962.

**89.** Heck MM, Tauber R, Schwaiger S, et al. Treatment Outcome, Toxicity, and Predictive Factors for Radioligand Therapy with (177)Lu-PSMA-I&T in Metastatic Castration-resistant Prostate Cancer. *Eur Urol.* 2019;75:920-926.

**90.** Budnik J, Suri J, Bates JE, Bylund KC, Milano MT. Prognostic Significance of Sites of Visceral Metastatic Disease in Prostate Cancer: A Population-based Study of 12,180 Patients. *Clin Genitourin Cancer.* 2019;17:260-267.

**91.** Kratochwil C, Haberkorn U, Giesel FL. (225)Ac-PSMA-617 for Therapy of Prostate Cancer. *Semin Nucl Med.* 2020;50:133-140.

**92.** Rosar F, Krause J, Bartholomä M, et al. Efficacy and Safety of [(225)Ac]Ac-PSMA-617 Augmented [(177)Lu]Lu-PSMA-617 Radioligand Therapy in Patients with Highly Advanced mCRPC with Poor Prognosis. *Pharmaceutics.* 2021;13.

**93.** Zemczak A, Kołodziej M, Gut P, et al. Effect of peptide receptor radionuclide therapy (PRRT) with tandem isotopes - [90Y]Y/[177Lu]Lu-DOTATATE in patients with disseminated neuroendocrine tumours depending on [18F]FDG PET/CT qualification in Polish multicentre experience - do we need [18F]FDG PET/CT for qualification to PRRT? *Endokrynol Pol.* 2020;71:240-248.

**94.** Kunikowska J, Zemczak A, Kołodziej M, et al. Tandem peptide receptor radionuclide therapy using (90)Y/(177)Lu-DOTATATE for neuroendocrine tumors efficacy and side-effects - polish multicenter experience. *Eur J Nucl Med Mol Imaging.* 2020;47:922-933.

**95.** de Jong M, Breeman WA, Valkema R, Bernard BF, Krenning EP. Combination radionuclide therapy using 177Lu- and 90Y-labeled somatostatin analogs. *J Nucl Med.* 2005;46 Suppl 1:13s-17s.

**96.** Kratochwil C, Bruchertseifer F, Rathke H, et al. Targeted alpha-Therapy of Metastatic Castration-Resistant Prostate Cancer with (225)Ac-PSMA-617: Dosimetry Estimate and Empiric Dose Finding. *J Nucl Med.* 2017;58:1624-1631.

**97.** Kratochwil C, Bruchertseifer F, Giesel FL, et al. 225Ac-PSMA-617 for PSMA-Targeted alpha-Radiation Therapy of Metastatic Castration-Resistant Prostate Cancer. *J Nucl Med.* 2016;57:1941-1944.

**98.** Stuparu AD, Meyer CAL, Evans-Axelsson SL, et al. Targeted alpha therapy in a systemic mouse model of prostate cancer - a feasibility study. *Theranostics.* 2020;10:2612-2620.

**99.** Kletting P, Schimmel S, Kestler HA, et al. Molecular radiotherapy: the NUKFIT software for calculating the time-integrated activity coefficient. *Med Phys.* 2013;40:102504.

**100.** Jiang Z, Revskaya E, Fisher DR, Dadachova E. In vivo Evaluation of Free and Chelated Accelerator-produced Actinium- 225 - Radiation Dosimetry and Toxicity Results. *Curr Radiopharm.* 2018;11:215-222.

**101.** Zang J, Fan X, Wang H, et al. First-in-human study of 177Lu-EB-PSMA-617 in patients with metastatic castration-resistant prostate cancer. *European Journal of Nuclear Medicine and Molecular Imaging.* 2019;46:148-158.

**102.** Liu Q, Zang J, Sui H, et al. Peptide Receptor Radionuclide Therapy of Late-Stage Neuroendocrine Tumor Patients with Multiple Cycles of (177)Lu-DOTA-EB-TATE. *J Nucl Med.* 2021;62:386-392.

**103.** Zhang J, Wang H, Jacobson O, et al. Safety, Pharmacokinetics, and Dosimetry of a Long-Acting Radiolabeled Somatostatin Analog (177)Lu-DOTA-EB-TATE in Patients with Advanced Metastatic Neuroendocrine Tumors. *J Nucl Med.* 2018;59:1699-1705.

**104.** Wester H-J, Wester H-JWester H-Js. PSMA ligands for imaging and endoradiotherapy, 2020.

**105.** Stabin MG, Sparks RB, Crowe E. OLINDA/EXM: the second-generation personal computer software for internal dose assessment in nuclear medicine. *J Nucl Med.* 2005;46:1023-1027.

**106.** Cohen EP, Robbins ME. Radiation nephropathy. *Semin Nephrol.* 2003;23:486-499.

**107.** Pellegrini G, Siwowska K, Haller S, et al. A Short-Term Biological Indicator for Long-Term Kidney Damage after Radionuclide Therapy in Mice. *Pharmaceuticals (Basel).* 2017;10.

**108.** Augustine AD, Gondré-Lewis T, McBride W, Miller L, Pellmar TC, Rockwell S. Animal models for radiation injury, protection and therapy. *Radiat Res.* 2005;164:100-109.

**109.** Schüler E, Larsson M, Parris TZ, Johansson ME, Helou K, Forssell-Aronsson E. Potential Biomarkers for Radiation-Induced Renal Toxicity following 177Lu-Octreotate Administration in Mice. *PLoS One.* 2015;10:e0136204.

**110.** Emami B, Lyman J, Brown A, et al. Tolerance of normal tissue to therapeutic irradiation. *Int J Radiat Oncol Biol Phys.* 1991;21:109-122.

**111.** Ljungberg M, Celler A, Konijnenberg MW, et al. MIRD Pamphlet No. 26: Joint EANM/MIRD Guidelines for Quantitative 177Lu SPECT Applied for Dosimetry of Radiopharmaceutical Therapy. *J Nucl Med.* 2016;57:151-162.

**112.** Chen X, Song E. Turning foes to friends: targeting cancer-associated fibroblasts. *Nat Rev Drug Discov.* 2019;18:99-115.

**113.** Katayama Y, Uchino J, Chihara Y, et al. Tumor Neovascularization and Developments in Therapeutics. *Cancers (Basel).* 2019;11.

**114.** Weis SM, Cheresh DA. Tumor angiogenesis: molecular pathways and therapeutic targets. *Nat Med.* 2011;17:1359-1370.

**115.** Pure E, Blomberg R. Pro-tumorigenic roles of fibroblast activation protein in cancer: back to the basics. *Oncogene.* 2018;37:4343-4357.

**116.** Brennen WN, Isaacs JT, Denmeade SR. Rationale behind targeting fibroblast activation protein-expressing carcinoma-associated fibroblasts as a novel chemotherapeutic strategy. *Mol Cancer Ther.* 2012;11:257-266.

**117.** Garin-Chesa P, Old LJ, Rettig WJ. Cell surface glycoprotein of reactive stromal fibroblasts as a potential antibody target in human epithelial cancers. *Proc Natl Acad Sci U S A.* 1990;87:7235-7239.

**118.** Shiga K, Hara M, Nagasaki T, Sato T, Takahashi H, Takeyama H. Cancer-Associated Fibroblasts: Their Characteristics and Their Roles in Tumor Growth. *Cancers (Basel).* 2015;7:2443-2458.

**119.** Lo A, Li CP, Buza EL, et al. Fibroblast activation protein augments progression and metastasis of pancreatic ductal adenocarcinoma. *JCI Insight.* 2017;2.

**120.** Gao LM, Wang F, Zheng Y, Fu ZZ, Zheng L, Chen LL. Roles of Fibroblast Activation Protein and Hepatocyte Growth Factor Expressions in Angiogenesis and Metastasis of Gastric Cancer. *Pathol Oncol Res.* 2019;25:369-376.

**121.** Liu J, Huang C, Peng C, et al. Stromal fibroblast activation protein alpha promotes gastric cancer progression via epithelial-mesenchymal transition through Wnt/ beta-catenin pathway. *BMC Cancer.* 2018;18:1099.

**122.** Jia J, Martin TA, Ye L, et al. Fibroblast activation protein-alpha promotes the growth and migration of lung cancer cells via the PI3K and sonic hedgehog pathways. *Int J Mol Med.* 2018;41:275-283.

**123.** Zi FM, He JS, Li Y, et al. Fibroblast activation protein protects bortezomib-induced apoptosis in multiple myeloma cells through beta-catenin signaling pathway. *Cancer Biol Ther.* 2014;15:1413-1422.

**124.** Zi F, He J, He D, Li Y, Yang L, Cai Z. Fibroblast activation protein alpha in tumor microenvironment: recent progression and implications (review). *Mol Med Rep.* 2015;11:3203-3211.

**125.** Liu F, Qi L, Liu B, et al. Fibroblast activation protein overexpression and clinical implications in solid tumors: a meta-analysis. *PLoS One.* 2015;10:e0116683.

**126.** Lindner T, Loktev A, Altmann A, et al. Development of Quinoline-Based Theranostic Ligands for the Targeting of Fibroblast Activation Protein. *J Nucl Med.* 2018;59:1415-1422.

**127.** Loktev A, Lindner T, Mier W, et al. A Tumor-Imaging Method Targeting Cancer-Associated Fibroblasts. *J Nucl Med.* 2018;59:1423-1429.

**128.** Loktev A, Lindner T, Burger EM, et al. Development of novel FAP-targeted radiotracers with improved tumor retention. *J Nucl Med.* 2019.

**129.** Kratochwil C, Flechsig P, Lindner T, et al. (68)Ga-FAPI PET/CT: Tracer Uptake in 28 Different Kinds of Cancer. *J Nucl Med.* 2019;60:801-805.

**130.** Rohrich M, Loktev A, Wefers AK, et al. IDH-wildtype glioblastomas and grade III/IV IDH-mutant gliomas show elevated tracer uptake in fibroblast activation protein-specific PET/CT. *Eur J Nucl Med Mol Imaging.* 2019.

**131.** Giesel FL, Heussel CP, Lindner T, et al. FAPI-PET/CT improves staging in a lung cancer patient with cerebral metastasis. *Eur J Nucl Med Mol Imaging.* 2019;46:1754-1755.

**132.** Giesel FL, Kratochwil C, Lindner T, et al. (68)Ga-FAPI PET/CT: Biodistribution and Preliminary Dosimetry Estimate of 2 DOTA-Containing FAP-Targeting Agents in Patients with Various Cancers. *J Nucl Med.* 2019;60:386-392.

**133.** Hamson EJ, Keane FM, Tholen S, Schilling O, Gorrell MD. Understanding fibroblast activation protein (FAP): substrates, activities, expression and targeting for cancer therapy. *Proteomics Clin Appl.* 2014;8:454-463.

**134.** Loevinger R, Budinger TF, Watson EE. *MIRD primer for absorbed dose calculations*: Society of Nuclear Medicine; 1988.

**135.** Bolch WE, Eckerman KF, Sgouros G, Thomas SR. MIRD pamphlet No. 21: a generalized schema for radiopharmaceutical dosimetry--standardization of nomenclature. *J Nucl Med.* 2009;50:477-484.

**136.** Hindorf C, Glatting G, Chiesa C, Linden O, Flux G. EANM Dosimetry Committee guidelines for bone marrow and whole-body dosimetry. *Eur J Nucl Med Mol Imaging.* 2010;37:1238-1250.

**137.** 1990 Recommendations of the International Commission on Radiological Protection. *Ann ICRP.* 1991;21:1-201.

**138.** Huang B, Law MW, Khong PL. Whole-body PET/CT scanning: estimation of radiation dose and cancer risk. *Radiology.* 2009;251:166-174.

**139.** Afshar-Oromieh A, Hetzheim H, Kubler W, et al. Radiation dosimetry of (68)Ga-PSMA-11 (HBED-CC) and preliminary evaluation of optimal imaging timing. *Eur J Nucl Med Mol Imaging.* 2016;43:1611-1620.

**140.** Pfob CH, Ziegler S, Graner FP, et al. Biodistribution and radiation dosimetry of (68)Ga-PSMA HBED CC-a PSMA specific probe for PET imaging of prostate cancer. *Eur J Nucl Med Mol Imaging.* 2016;43:1962-1970.

**141.** Sandstrom M, Velikyan I, Garske-Roman U, et al. Comparative biodistribution and radiation dosimetry of 68Ga-DOTATOC and 68Ga-DOTATATE in patients with neuroendocrine tumors. *J Nucl Med.* 2013;54:1755-1759.

**142.** Gear JI, Cox MG, Gustafsson J, et al. EANM practical guidance on uncertainty analysis for molecular radiotherapy absorbed dose calculations. *Eur J Nucl Med Mol Imaging.* 2018;45:2456-2474.

**143.** Keane FM, Yao TW, Seelk S, et al. Quantitation of fibroblast activation protein (FAP)-specific protease activity in mouse, baboon and human fluids and organs. *FEBS Open Bio.* 2013;4:43-54.

**144.** Yazbeck R, Jaenisch SE, Abbott CA. Potential disease biomarkers: dipeptidyl peptidase 4 and fibroblast activation protein. *Protoplasma.* 2018;255:375-386.

**145.** Rahmim A, Zaidi H. PET versus SPECT: strengths, limitations and challenges. *Nucl Med Commun.* 2008;29:193-207.

**146.** Gundem G, Van Loo P, Kremeyer B, et al. The evolutionary history of lethal metastatic prostate cancer. *Nature.* 2015;520:353-357.

**147.** Shou J, Zhang Q, Wang S, Zhang D. The prognosis of different distant metastases pattern in prostate cancer: A population based retrospective study. *Prostate.* 2018;78:491-497.

**148.** Seitz AK, Rauscher I, Haller B, et al. Preliminary results on response assessment using (68)Ga-HBED-CC-PSMA PET/CT in patients with metastatic prostate cancer undergoing docetaxel chemotherapy. *Eur J Nucl Med Mol Imaging.* 2018;45:602-612.

**149.** Choo MS, Kim M, Ku JH, Kwak C, Kim HH, Jeong CW. Extended versus Standard Pelvic Lymph Node Dissection in Radical Prostatectomy on Oncological and Functional Outcomes: A Systematic Review and Meta-Analysis. *Ann Surg Oncol.* 2017;24:2047-2054.

**150.** Robu S, Schottelius M, Eiber M, et al. Preclinical Evaluation and First Patient Application of 99mTc-PSMA-I&S for SPECT Imaging and Radioguided Surgery in Prostate Cancer. *J Nucl Med.* 2017;58:235-242.

**151.** Maurer T, Robu S, Schottelius M, et al. (99m)Technetium-based Prostate-specific Membrane Antigen-radioguided Surgery in Recurrent Prostate Cancer. *Eur Urol.* 2019;75:659-666.

**152.** Horn T, Krönke M, Rauscher I, et al. Single Lesion on Prostate-specific Membrane Antigen-ligand Positron Emission Tomography and Low Prostate-specific Antigen Are Prognostic Factors for a Favorable Biochemical Response to Prostate-specific Membrane Antigen-targeted Radioguided Surgery in Recurrent Prostate Cancer. *Eur Urol.* 2019;76:517-523.

**153.** The 2007 Recommendations of the International Commission on Radiological Protection. ICRP publication 103. *Ann ICRP.* 2007;37:1-332.

**154.** Ferrari M, De Marco P, Origgi D, Pedroli G. SPECT/CT radiation dosimetry. *Clinical and Translational Imaging.* 2014;2:557-569.

**155.** Santos-Cuevas C, Davanzo J, Ferro-Flores G, et al. (99m)Tc-labeled PSMA inhibitor: Biokinetics and radiation dosimetry in healthy subjects and imaging of prostate cancer tumors in patients. *Nucl Med Biol.* 2017;52:1-6.

**156.** Hillier SM, Maresca KP, Lu G, et al. 99mTc-labeled small-molecule inhibitors of prostate-specific membrane antigen for molecular imaging of prostate cancer. *J Nucl Med.* 2013;54:1369-1376.

**157.** Vallabhajosula S, Nikolopoulou A, Babich JW, et al. 99mTc-labeled small-molecule inhibitors of prostate-specific membrane antigen: pharmacokinetics and biodistribution studies in healthy subjects and patients with metastatic prostate cancer. *J Nucl Med.* 2014;55:1791-1798.

**158.** Giesel FL, Hadaschik B, Cardinale J, et al. F-18 labelled PSMA-1007: biodistribution, radiation dosimetry and histopathological validation of tumor lesions in prostate cancer patients. *Eur J Nucl Med Mol Imaging.* 2017;44:678-688.

**159.** Urbán S, Meyer C, Dahlbom M, et al. Radiation Dosimetry of (99m)Tc-PSMA I&S: A Single-Center Prospective Study. *J Nucl Med.* 2021;62:1075-1081.

**160.** Maurer T, Weirich G, Schottelius M, et al. Prostate-specific membrane antigen-radioguided surgery for metastatic lymph nodes in prostate cancer. *Eur Urol.* 2015;68:530-534.

**161.** Farolfi A, Gafita A, Calais J, et al. (68)Ga-PSMA-11 Positron Emission Tomography Detects Residual Prostate Cancer after Prostatectomy in a Multicenter Retrospective Study. *J Urol.* 2019;202:1174-1181.

**162.** Porres D, Pfister D, Thissen A, et al. The role of salvage extended lymph node dissection in patients with rising PSA and PET/CT scan detected nodal recurrence of prostate cancer. *Prostate Cancer Prostatic Dis.* 2017;20:85-92.

**163.** Fossati N, Suardi N, Gandaglia G, et al. Identifying the Optimal Candidate for Salvage Lymph Node Dissection for Nodal Recurrence of Prostate Cancer: Results from a Large, Multi-institutional Analysis. *Eur Urol.* 2019;75:176-183.

**164.** Suardi N, Gandaglia G, Gallina A, et al. Long-term outcomes of salvage lymph node dissection for clinically recurrent prostate cancer: results of a single-institution series with a minimum follow-up of 5 years. *Eur Urol.* 2015;67:299-309.

**165.** Rauscher I, Duwel C, Wirtz M, et al. Value of (111) In-prostate-specific membrane antigen (PSMA)-radioguided surgery for salvage lymphadenectomy in recurrent prostate cancer: correlation with histopathology and clinical follow-up. *BJU Int.* 2017;120:40-47.

**166.** Calais J, Czernin J, Thin P, et al. Safety of PSMA-Targeted Molecular Radioligand Therapy with <sup>177</sup>Lu-PSMA-617: Results from the Prospective Multicenter Phase 2 Trial RESIST-PC (NCT03042312). *Journal of Nuclear Medicine.* 2021;62:1447.

**167.** Wan H. Automated Contouring Using Neural Networks [White Paper]. *MIM Software Inc.* 2021.

**168.** Jackson PA, Hofman MS, Hicks RJ, Scalzo M, Violet J. Radiation Dosimetry in (177)Lu-PSMA-617 Therapy Using a Single Posttreatment SPECT/CT Scan: A Novel Methodology to Generate Time- and Tissue-Specific Dose Factors. *J Nucl Med.* 2020;61:1030-1036.

**169.** Lehnert W, Schmidt K, Kimiaei S, Meyer T, Bronzel M, Kluge A. Impact of Modality (2D Planar, 2D/3D Hybrid, 3D SPECT) on Kidneys Absorbed Dose in <sup>177</sup>Lu-based PRRT. *Journal of Nuclear Medicine.* 2018;59:391.

**170.** Klaus R, Niyazi M, Lange-Sperandio B. Radiation-induced kidney toxicity: molecular and cellular pathogenesis. *Radiation Oncology.* 2021;16:43.

**171.** Herrmann K, Rahbar K, Eiber M, et al. Dosimetry of 177Lu-PSMA-617 for the treatment of metastatic castration-resistant prostate cancer: results from the VISION trial sub-study. *Journal of Clinical Oncology.* 2022;40:97-97.

**172.** Roth D, Gustafsson J, Sundlov A, Sjogreen Gleisner K. A method for tumor dosimetry based on hybrid planar-SPECT/CT images and semiautomatic segmentation. *Med Phys.* 2018;45:5004-5018.

**173.** Sundlöv A, Gustafsson J, Brolin G, et al. Feasibility of simplifying renal dosimetry in (177)Lu peptide receptor radionuclide therapy. *EJNMMI physics.* 2018;5:12-12.

**174.** Willowson KP, Ryu H, Jackson P, Singh A, Eslick E, Bailey DL. A Comparison of 2D and 3D Kidney Absorbed Dose Measures in Patients Receiving (177)Lu-DOTATATE. *Asia Oceania journal of nuclear medicine & biology.* 2018;6:113-119.

**175.** Dewaraja YK, Frey EC, Sgouros G, et al. MIRD pamphlet No. 23: quantitative SPECT for patient-specific 3-dimensional dosimetry in internal radionuclide therapy. *J Nucl Med.* 2012;53:1310-1325.

**176.** Flynn AA, Green AJ, Pedley RB, Boxer GM, Boden R, Begent RH. A mouse model for calculating the absorbed beta-particle dose from (131)I- and (90)Y-labeled immunoconjugates, including a method for dealing with heterogeneity in kidney and tumor. *Radiat Res.* 2001;156:28-35.

**177.** Bolch WE, Bouchet LG, Robertson JS, et al. MIRD pamphlet No. 17: the dosimetry of nonuniform activity distributions--radionuclide S values at the voxel level. Medical Internal Radiation Dose Committee. *J Nucl Med.* 1999;40:11s-36s.

**178.** Kost SD, Dewaraja YK, Abramson RG, Stabin MG. VIDA: a voxel-based dosimetry method for targeted radionuclide therapy using Geant4. *Cancer Biother Radiopharm.* 2015;30:16-26.

**179.** Hauf S, Kuster M, Batič M, et al. Radioactive Decays in Geant4. *IEEE Transactions on Nuclear Science.* 2013;60:2966-2983.

**180.** Huizing DMV, de Wit-van der Veen BJ, Verheij M, Stokkel MPM. Dosimetry methods and clinical applications in peptide receptor radionuclide therapy for neuroendocrine tumours: a literature review. *EJNMMI research.* 2018;8:89-89.

**181.** Hippelainen E, Tenhunen M, Sohlberg A. Fast voxel-level dosimetry for (177)Lu labelled peptide treatments. *Phys Med Biol.* 2015;60:6685-6700.

**182.** Kratochwil C, Schmidt K, Afshar-Oromieh A, et al. Targeted alpha therapy of mCRPC: Dosimetry estimate of (213)Bismuth-PSMA-617. *European journal of nuclear medicine and molecular imaging.* 2018;45:31-37.

**183.** Okamoto S, Thieme A, Allmann J, et al. Radiation Dosimetry for (177)Lu-PSMA I&T in Metastatic Castration-Resistant Prostate Cancer: Absorbed Dose in Normal Organs and Tumor Lesions. *J Nucl Med.* 2017;58:445-450.

**184.** de Kruijff RM, Wolterbeek HT, Denkova AG. A Critical Review of Alpha Radionuclide Therapy-How to Deal with Recoiling Daughters? *Pharmaceuticals (Basel, Switzerland).* 2015;8:321-336.

**185.** McDevitt MR, Ma D, Lai LT, et al. Tumor therapy with targeted atomic nanogenerators. *Science.* 2001;294:1537-1540.

**186.** Siegel JA, Thomas SR, Stubbs JB, et al. MIRD pamphlet no. 16: Techniques for quantitative radiopharmaceutical biodistribution data acquisition and analysis for use in human radiation dose estimates. *J Nucl Med.* 1999;40:37s-61s.

**187.** Willowson KP, Eslick E, Ryu H, Poon A, Bernard EJ, Bailey DL. Feasibility and accuracy of single time point imaging for renal dosimetry following (177)Lu-DOTATATE ('Lutate') therapy. *EJNMMI physics.* 2018;5:33-33.

**188.** Hanscheid H, Lapa C, Buck AK, Lassmann M, Werner RA. Dose Mapping After Endoradiotherapy with (177)Lu-DOTATATE/DOTATOC by a Single Measurement After 4 Days. *J Nucl Med.* 2018;59:75-81.

**189.** Jackson PA, Beauregard JM, Hofman MS, Kron T, Hogg A, Hicks RJ. An automated voxelized dosimetry tool for radionuclide therapy based on serial quantitative SPECT/CT imaging. *Med Phys.* 2013;40:112503.

**190.** Sidey-Gibbons JAM, Sidey-Gibbons CJ. Machine learning in medicine: a practical introduction. *BMC medical research methodology.* 2019;19:64-64.

**191.** Rajkomar A, Dean J, Kohane I. Machine Learning in Medicine. *N Engl J Med.* 2019;380:1347-1358.

**192.** Uribe CF, Mathotaarachchi S, Gaudet V, et al. Machine Learning in Nuclear Medicine: Part 1-Introduction. *J Nucl Med.* 2019;60:451-458.